

DELIVERABLE D2.12

**PUBLIC**

Six conferences  
contributions and  
three journal  
articles



**Co-funded by  
the European Union**

Elodie Pahon (UBFC)

Quality Assurance: Federico Zenith (SINTEF)

**Project acronym:** HAEOLUS

**Project title:** Hydrogen-Aeolic Energy with Optimised eElectrolysers Upstream of Substation

**Project number:** 779469

**Call:** H2020-JTI-FCH-2017-1

**Topic:** FCH-02-4-2017

**Document date:** September 06, 2022

**Due date:** December 31, 2023

**Keywords:** publications ; scientific journals ; dissemination ; innovation

**Abstract:** This deliverable presents a review of six conferences contributions and three journal articles published in high level scientific journals.

## Revision History

Date	Description	Author
2022/09/06	First completed version	Elodie PAHON (UBFC)

*This project has received funding from the Fuel Cells and Hydrogen 2 Joint Undertaking under the European Union's Horizon 2020 research and innovation programme under grant agreement No 779469.*

*Any contents herein reflect solely the authors' view. The FCH 2 JU and the European Commission are not responsible for any use that may be made of the information herein contained.*

## Table of Contents

1	Introduction.....	3
2	Six conferences contributions .....	3
2.1	Oral presentation .....	3
2.2	Poster presentation.....	3
2.3	Oral presentation .....	3
2.4	Oral presentation .....	3
2.5	Oral presentation .....	3
2.6	Oral presentation .....	4
3	Three journal articles.....	4
3.1	Control Engineering Practice .....	4
3.2	Energies .....	4
3.3	International Journal of Hydrogen Energy .....	4

## 1 Introduction

This deliverable presents a review of six conferences contributions and three journal articles published in high-level scientific journals.

The list of publications is given from the oldest to the most recent.

## 2 Six conferences contributions

### 2.1 Oral presentation

A presentation given at the Nordic Hydrogen and Fuel Cells Conference untitled “Large-scale hydrogen production from wind power in Arctic conditions”. This presentation was done in October 8<sup>th</sup>, 2018 in Reykjavik, Iceland.

The complete DOI is <https://doi.org/10.5281/zenodo.1460454>

The presentation is given in Appendix 1.

### 2.2 Oral presentation

A presentation given at the Input Meeting for Svalbard’s Future Energy Supply untitled “Hydrogen Export to Svalbard: Exploiting Stranded Wind in Finnmark”. This presentation was done in November 9<sup>th</sup>, 2018 in Oslo, Norway.

The complete DOI is <https://doi.org/10.5281/zenodo.1482894>

The presentation is given in Appendix 2.

### 2.3 Poster presentation

A poster presentation to 12<sup>th</sup> Conference Exhibition on Energy Transition and Circular Economy which took place in Napoli, Italy from 28<sup>th</sup> to 30<sup>th</sup> March, 2019.

The poster presented is given in Appendix 3.

### 2.4 Oral presentation

A presentation given at the Hydrogen i vinden Conference untitled “Visjoner for hydrogen og vind i Finnmark”. This presentation was done in March 21<sup>st</sup>, 2019 in Norway.

The presentation is given in Appendix 4.

### 2.5 Oral presentation

. A conference article devoted to the International Conference named "2020 Prognostics and Health Management Conference" which took place in Besancon, France. This is 12th PHM Conference virtual conference which be held in November 9 – 13, 2020.

The complete citation is M. Yue, Z. Li, R. Roche, S. Jemei and N. Zerhouni, "A Feature-Based Prognostics Strategy for PEM Fuel Cell Operated under Dynamic Conditions," *2020 Prognostics and Health Management Conference (PHM-Besançon)*, 2020, pp. 122-127, doi: 10.1109/PHM-Besançon49106.2020.00026.



The full paper is given in Appendix 5.

## 2.6 Oral presentation

A presentation given at the International Summit on the Operational Analysis of Wind Farms from 19<sup>th</sup> to 20<sup>th</sup> November 2020. This was a virtual event.

The presentation is given in Appendix 6.

## 3 Three journal articles

Three journal articles were published in high level quality journals in open access.

### 3.1 Control Engineering Practice

M. Yue, Z. Li, R. Roche, S. Jemei, N. Zerhouni, Degradation identification and prognostics of proton exchange membrane fuel cell under dynamic load, Control Engineering Practice, Volume 118, 2022, 104959, ISSN 0967-0661, <https://doi.org/10.1016/j.conengprac.2021.104959>.

The full paper is given in Appendix 7.

### 3.2 Energies

Mariani, V.; Zenith, F.; Glielmo, L. Operating Hydrogen-Based Energy Storage Systems in Wind Farms for Smooth Power Injection: A Penalty Fees Aware Model Predictive Control. Energies 2022, 15, 6307. <https://doi.org/10.3390/en15176307>

The full paper is given in Appendix 8.

### 3.3 International Journal of Hydrogen Energy

M. B. Abdelghany, M. F. Shehzad, V. Mariani, D. Liuzza, L. Glielmo, Two-stage model predictive control for a hydrogen-based storage system paired to a wind farm towards green hydrogen production for fuel cell electric vehicles, International Journal of Hydrogen Energy, 2022, ISSN 0360-3199, <https://doi.org/10.1016/j.ijhydene.2022.07.136>.

The full paper is given in Appendix 9.

Federico Zenith

# Large-scale hydrogen production from wind power in Arctic conditions

## The HAEOLUS project

SINTEF Mathematics & Cybernetics

Nordic Hydrogen & Fuel Cell  
Conference  
October 9, 2018  
Reykjavík, Iceland



# Outline

Motivation

The Project

Future Perspective

# Outline

Motivation

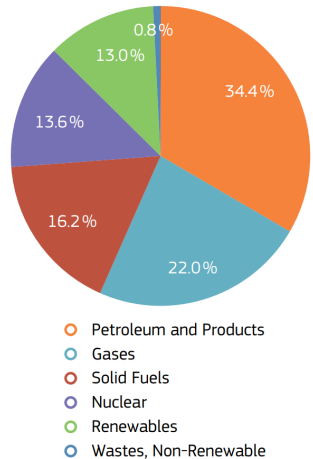
The Project

Future Perspective

# Motivation

- EU 2030 target: 27 % renewable energy consumption
  - In 2015 it was 13 %
  - *Production* is already 26.2 % (2015)
  - No renewables in energy imports
- Most renewables produce electricity
- Several are not controllable
- Some are unpredictable

2015 EU consumption



# Constraints of Wind Power

- Hard to predict production
- Capacity factor about 33 %
- Need reserve capacity
- Often, good wind power is found where:
  - there is little hydro potential
  - few people live
  - the grid is weak
  - accessibility is difficult
- All this even more true for offshore wind!



# The Connection between Hydrogen and Wind

- Beyond 20 % wind share, value plummets
  - *Gonzalez et al., Ren. Ener., 29.4 (2003), 471–489*
- Hydro is rarely possible
- Batteries are too expensive
- Hydrogen has lower efficiency
- IEA's HIA task 24 identified 3 main cases:
  - Energy storage
  - Mini-grid (e.g. islands)
  - Fuel production
- Grid services, reserves, target matching...



The Utsira, Norway,  
50 kW / 215 kg<sub>H<sub>2</sub></sub> system  
(2004)

# Outline

Motivation

The Project

Future Perspective



# The HAEOLUS Project

<http://haeolus.eu> - @HaeolusProject

- A FCH2 JU Innovation Action
- Objectives:
  - Enable more wind power
  - Test multiple use cases
  - Demonstrate a 2.5 MW system
  - Demonstrate remote operation
  - Report & disseminate
- Key figures:
  - Budget: 6.9 M€ (5 M€ from EU)
  - Time frame 2018–2021
  - Capacity 1 t/d
  - Production start: late summer 2019

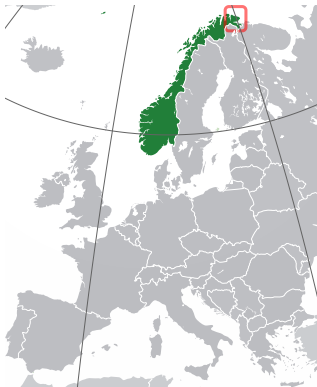


Kick-off in Oslo, January 2018

# The Wind Park

Raggovidda wind park, Berlevåg municipality, Varanger peninsula, Finnmark county

- The Raggovidda wind park:
  - 45 MW built of 200 MW concession
  - Neighbour Hamnafjell: 50 MW / 120 MW
  - Bottleneck to main grid is 95 MW
  - Total Varanger resources about 2000 MW



# The Wind Park

Raggovidda wind park, Berlevåg municipality, Varanger peninsula, Finnmark county

- The Raggovidda wind park:
  - 45 MW built of 200 MW concession
  - Neighbour Hamnafjell: 50 MW / 120 MW
  - Bottleneck to main grid is 95 MW
  - Total Varanger resources about 2000 MW
- Capacity factor 50 %
- Local consumption max. 60 MW
- Local economy based on fishing
- Partner operator of park & grid:



# The Electrolyser System's Site

Raggovidda wind park, Berlevåg municipality, Varanger peninsula, Finnmark county

- Located beside Berlevåg harbour
- Compact 2.5 MW PEM electrolyser
- 100 kW fuel cell for re-electrification
- New 10 km power line from Raggovidda
- Virtually “inside the fence”
- Accessibility by road or sea
- At least 120 t over 2.5 year
- Partner electrolyser manufacturer:

**HYDROGENICS**  
SHIFT POWER | ENERGIZE YOUR WORLD



View of Berlevåg,  
site highlighted

## Grid Services

- Wind energy production target match
  - Currently: prediction outsourced
  - 3<sup>rd</sup> party paid in % of production
  - Easily quantifiable potential
  - Adjust electrolyser to fulfil target
- Primary, secondary & tertiary reserves
  - Electrolysers are easily ramped
  - Can acquire slots in all reserves
- Project partner:



Hour	Price NOK/MW	Volume MW
1	180	33
2	139	34
3	139	34
4	139	34
⋮	⋮	⋮
18	18	34
19	18	25
20	17	48
⋮	⋮	⋮

Price for primary reserves on  
October 3, northern Norway.

## Other Activities

- Remote operation
  - Relevant for many wind parks
  - Run demonstration from Italy

- Partner software developer:



- 
- System prognostics
    - Reduce on-site inspections
    - Optimise maintenance
    - Avoid unscheduled stops

- Partner university:



- Dynamic modelling
  - Process model & optimisation
  - Control synthesis

- Partner university:



University of Sannio

- 
- Control implementation
  - Integration with smart grids
  - H<sub>2</sub> valorisation plan
  - Coordinator:



# Outline

Motivation

The Project

Future Perspective

# Expected Impact

## From Short to Long Term

- Convince Varanger Kraft to expand hydrogen production
- Export model to other sites in Europe (other EU projects?)
- Allow deployment of wind power beyond 20 %
- Push hydrogen utilisation in the area
  - Mobility, industry, etc.
- Contribute to EU renewable targets & energy independence



# Public Deliverables

## Reports (18):

- Raggovidda energy analysis
- Dynamic model & control
- Impact on energy systems, RCS
- Valorisation plan
- Business case analysis
- Road to MAWP 2023 targets
- Techno-economic analysis
- Environmental performance
- Demonstration protocols & data

## Other (15):

- Workshop at ECC2019 Naples
- Real-time demo on website
- Plant visit
- Academic seminars
- Student internship
- Presence at industrial fair

# What to Do with the Hydrogen?

## Valorisation Plan: Identified Opportunities

Action	Realism	Size	Gimmick
Svalbard energy supply	✓	✓	✓
Coastal ships	(✓)	✓	✓
Fishing boats	✓	✓	
Ammonia production	✓	✓	
Aquaculture	(✓)	✓	
Fast passenger boats	(✓)	✓	
Cars	✓		✓
Regional mini-buses	✓		
Waste collection trucks	✓		
Backup generators	✓		
Snowmobiles			✓
Regional planes		✓	✓
ZE steel production		✓	
Mining and ore processing		✓	



# Conclusion

- Hydrogen can boost wind power
- HAEOLUS will test relevant cases for Europe and beyond
- Many possibilities for hydrogen use—the most promising still to develop, though

# Conclusion

- Hydrogen can boost wind power
- HAEOLUS will test relevant cases for Europe and beyond
- Many possibilities for hydrogen use—the most promising still to develop, though



*Thank you for your attention!*



## Hydrogen-Aeolic Energy with Optimised eLectrolysers Upstream of Substation

This project has received funding from the Fuel Cells and Hydrogen 2 Joint Undertaking under the European Union's Horizon 2020 research and innovation programme under grant agreement № 779469.





## Hydrogen Export to Svalbard Exploiting Stranded Wind in Finnmark

Federico Zenith, SINTEF Mathematics & Cybernetics

Input Meeting for Svalbard's Future Energy Supply  
November 9, 2018, Oslo, Norway

# Outline

---

Motivation

Opportunity: The HAEOLUS Project

Quantification

# Outline

---

Motivation

Opportunity: The HAEOLUS Project

Quantification



# Hydrogen Import to Svalbard

---

- Not considered in Multiconsult's report
- Can exploit better green H<sub>2</sub> sources
  - Wind in Finnmark
- H<sub>2</sub> can be readily imported
  - Container solutions available
  - (Initially) also non-green H<sub>2</sub>?
- Combined heat & power (CHP) fuel cells
  - High efficiency (45 % + 45 %)
  - Market ready



# Flexibility & Scalability in Deployment

---

- Fuel cells are modular
- Can be introduced gradually
  - Start with smaller pilot
  - Extend later: future-proof
  - LNG requires MW-class investment
- Can team up with local renewables later
- Distributed generation several places
  - Same efficiency
  - E.g. replacing boilers FH1–6
  - Better reliability with multiple systems
- Can make diesel generators obsolete



Hydrogenics “closet” with 4×33 kW fuel cells systems.

Each can be replaced individually.

Already deployed in 1 MW unit i Kolon, Korea (in a 40' container).

# Outline

---

Motivation

Opportunity: The HAEOLUS Project

Quantification

# The HAEOLUS Project

[haeolus.eu](http://haeolus.eu), @HaeolusProject , @Haeolus , Haeolus 

- Hydrogen production from wind power
- Similar to Utsira project, but larger: 50 kW  $\Rightarrow$  2.5 MW
- Stranded wind power in Varanger
  - 320 MW concession, 95 MW built
  - Bottleneck in Varangerbotn
  - Resseruser opptil 2000 MW
- Norway's best capacity factor, 50 %
- No significant hydro power for storage
- Can import 160 MW to maintain H<sub>2</sub> production
- Vision: produce and export hydrogen worldwide



# HAEOLUS Facts & Plans

---

- Production start: summer 2019
- Location: Berlevåg harbour
- Capacity: 1 ton H<sub>2</sub> per day
- Total committed production: 120 tons
- Project duration: 4 years
- Own power line to Raggovidda
- Total budget about 7 M€, EU contribution 5 M€



Berlevåg and the plant site at the harbour.

# HAEOLUS Consortium & Objectives

---

## Objectives:

- Demonstration of multiple use modes
  - Also mini-grid, relevant for Svalbard
- Hydrogen valorisation
- Sale of grid services
- Remote operation
- Control algorithms development
- Minimised maintenance by prognostics
- **33** public deliverables (18 reports)

## Consortium:

- SINTEF (coordinator)
- Hydrogenics
- Varanger Kraft
- Tecnalia
- UniSannio
- UBFC
- KES

# Outline

---

Motivation

Opportunity: The HAEOLUS Project

Quantification

# Data Sources

---

- Energy cost from wind in Finnmark: 215 NOK/MWh<sup>1</sup>
- Electrolyser: 9.3 MNOK/MW, OPEX 7 % derav<sup>2</sup>
- Compressors: 6 MNOK/MW<sub>H<sub>2</sub></sub>, OPEX 4 % derav<sup>2</sup>
- 40' container, 780 kg<sub>H<sub>2</sub></sub>: 3 MNOK
- Logistics Berlevåg-Longyearbyen: 10 NOK/kg<sub>H<sub>2</sub></sub>
- CHP fuel cells: 25 kNOK/kW, 22 years<sup>3</sup>

## Sources:

1. Multiconsult LCOE calculation for Davvi wind power plant
2. [Noack et al.](#) (DLR, LBST, Fraunhofer, KBB)
3. FCH JU's Multi-Annual Implementation Plan (MAWP)



# Full Deployment with only Imported Hydrogen

All Items are NPV over 25 years with 4 % Discounting Rate

Energy costs (262.6 GWh/y)	882 MNOK
30 MW Electrolysers	279 MNOK
Electrolyser OPEX	304 MNOK
Compressors	158 MNOK
Compressor OPEX	70 MNOK
243 hydrogen containers	729 MNOK
Logistics over 25 years	789 MNOK
Fuel cells in Longyearbyen	212 MNOK
<hr/>	
<b>Total</b>	<b>3423 MNOK</b>
Energy cost	0.91 NOK/kWh

- Not very competitive with alternatives...
- ... but actually OK kWh price
- 60 MW new wind power @ Raggovidda
- Burning some H<sub>2</sub> for heat—wasteful
- What can improve in time?
  - Fuel cell cost
  - Electrolyser cost and OPEX
  - Cheaper H<sub>2</sub> storage in Longyearbyen
  - Heat savings (–40 %)
- It can land at about 2000 MNOK

# Pilot Deployment in Conjunction with HAEOLUS

Adapted to a 1 t/d production in Berlevåg

## Investments

Compressor	8 MNOK
Fuel cells	16 MNOK
10 containers	30 MNOK

---

<i>Total investments</i>	54 MNOK
--------------------------	---------

---

## Yearly OPEX

Energy	4.1 MNOK/y
Logistics	3.6 MNOK/y
Compressor OPEX	0.3 MNOK/y

---

<i>Total OPEX</i>	8 MNOK
-------------------	--------

---

- Budget within range of an EU demo project
  - FCH JU call coming in January...
- Proceed in steps:
  - Replace diesel gensets
  - Supplement local renewables
  - Combine with battery storage (day cycle)
  - Gradually expand capacity
- Optimise battery+hydrogen+import
- Finally, take coal plant offline

# Conclusions

---

- Hydrogen import to Svalbard is economically viable (0.91 NOK/kWh)
- Hydrogen import is more expensive than alternatives, if stand-alone
- Storage and logistics are major expenses; unlikely to drop
- Use import as support to local wind/solar to achieve zero emission
- Gradually introduce hydrogen, complete by 2038 (coal plant decommissioning)

## Conclusions

---

- Hydrogen import to Svalbard is economically viable (0.91 NOK/kWh)
- Hydrogen import is more expensive than alternatives, if stand-alone
- Storage and logistics are major expenses; unlikely to drop
- Use import as support to local wind/solar to achieve zero emission
- Gradually introduce hydrogen, complete by 2038 (coal plant decommissioning)

***Thank you for your attention!***

# H<sub>2</sub> A EOLUS

## Hydrogen-Aeolic Energy with Optimised eLectrolysers Upstream of Substation

This project has received funding from the Fuel Cells and Hydrogen 2 Joint Undertaking under the European Union's Horizon 2020 research and innovation programme under grant agreement № 779469.





Technology for a better society



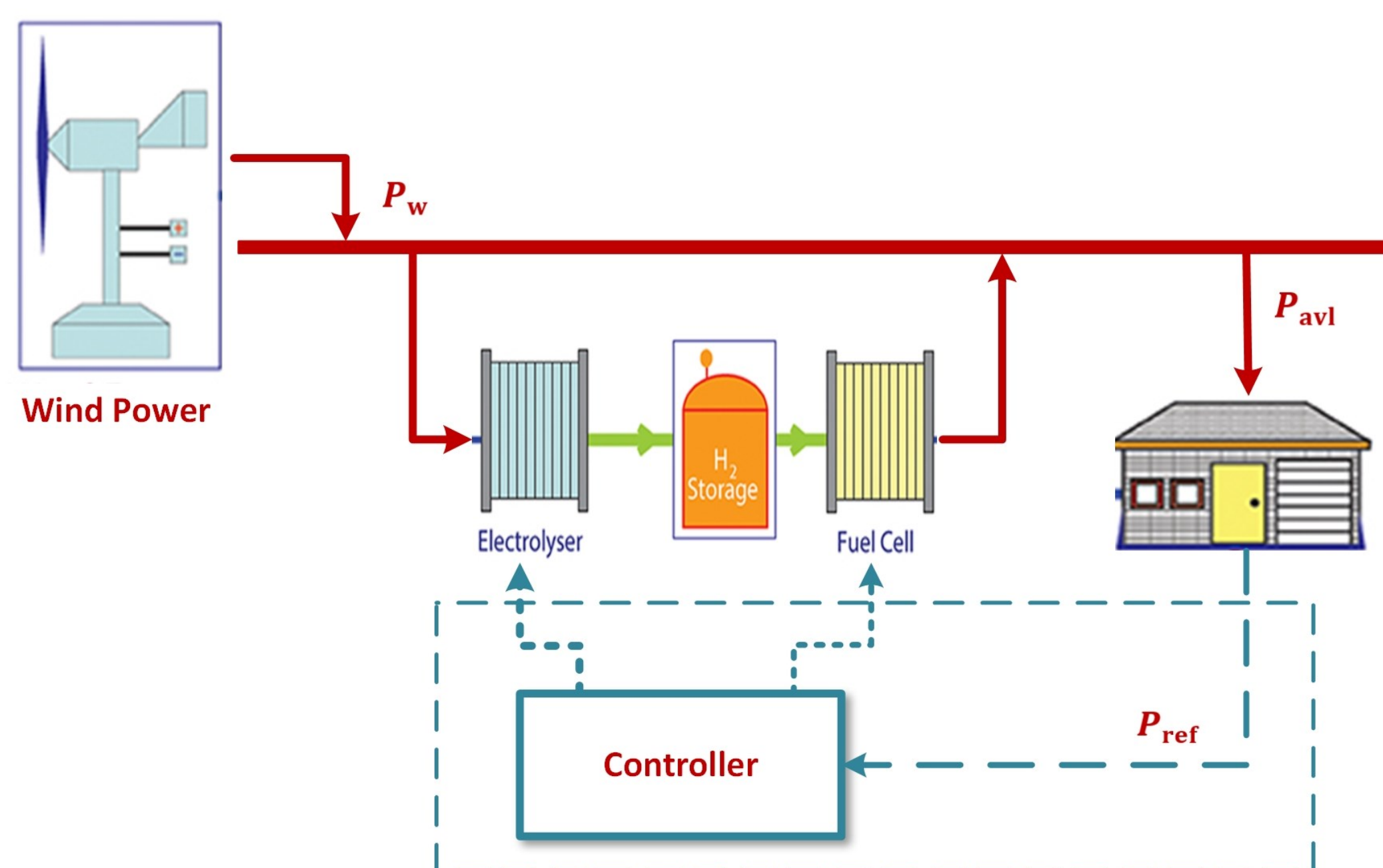
# H<sub>2</sub> A $\Xi$ L U S

## Hydrogen-Aeolic Energy with Optimised eLectrolysers Upstream of Substation



### IL PROGETTO

Il progetto HAEOLUS, finanziato dalla UE per il contenuto innovativo, prevede la realizzazione di un sistema dimostrativo di produzione ed accumulo dell'idrogeno ("elettrolizzatore") prodotto da un impianto eolico situato in Norvegia, il Raggovidda Wind Park.



Il progetto affronta tre importanti argomenti identificati dall'Agenzia Internazionale per l'Energia:

- ⇒ Accumulo dell'energia
- ⇒ Mini-grid
- ⇒ Produzione energetica

Per ognuno di questi aspetti nel progetto saranno sviluppate e sperimentate per circa 4 anni le strategie operative, ottimizzando le operazioni in funzione delle previsioni meteorologiche e del prezzo (variabile) dell'energia, ma anche dei vincoli tecnologici e gestionali.

Tutto il sistema sarà monitorato e controllato a distanza, sia per le difficoltà di accesso al sito (oltre il circolo polare artico) sia per verificarne l'affidabilità ed il livello di automazione



### GLI OBIETTIVI



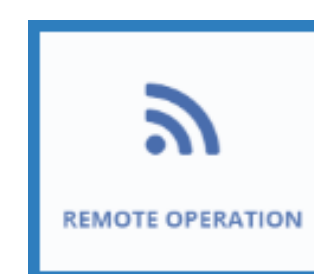
PIÙ ENERGIA EOLICA



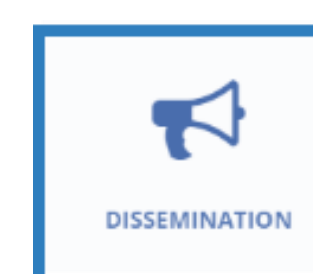
ELETTROLIZZATORE DA 2,5 MW



PIÙ CASI D'USO



GESTIONE REMOTA



DIFFUSIONE



### IL CONSORZIO

#### SINTEF

Il più grande istituto di ricerca indipendente della Scandinavia e leader del progetto

<https://www.sintef.no/>

#### UBFC

Una federazione di università francesi tra cui l'Université de Franche-Comté (UFC) e Université de Technologie Belfort-Montbéliard (UTBM)

<http://www.ubfc.fr/>

#### UNIVERSITA' DEGLI STUDI DEL SANNIO

Ateneo nato nel 1990 caratterizzato da eccellenze nei dipartimenti di ingegneria, economia e giurisprudenza

<https://www.unisannio.it/it>

#### KES

Una PMI focalizzata sullo sviluppo di soluzioni software innovative in ambito smart city e tecnologie IoT

<http://www.kesitaly.it/>

#### TECNALIA

Il più grande centro di ricerca ed organizzazione tecnologica in Spagna ed uno dei più grandi d'Europa

<http://www.tecnalia.es/>

#### VARANGER KRAFT

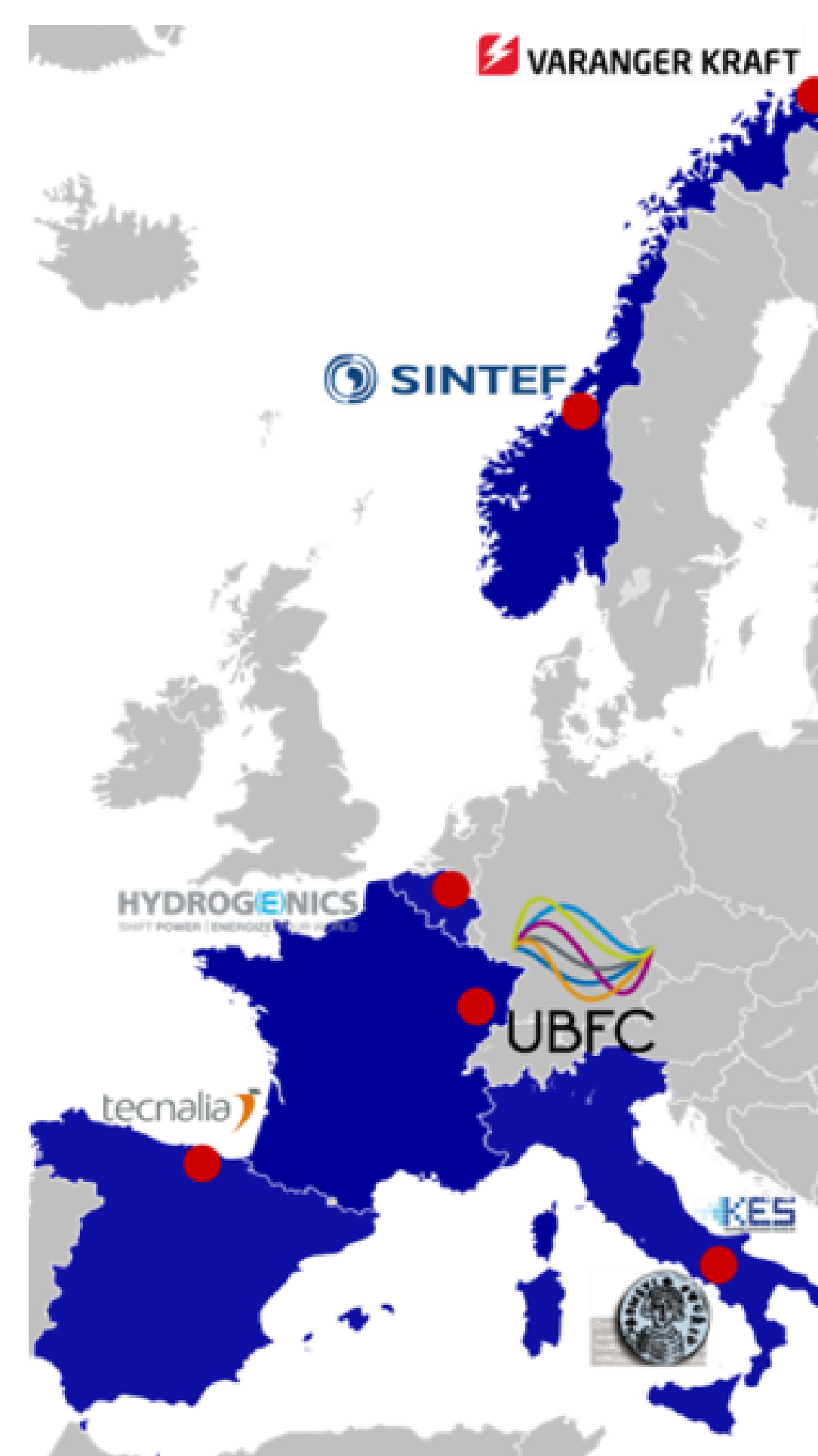
Un utility energetica che gestisce il Raggovidda Wind Park

<http://www.varanger-kraft.no>

#### HYDROGENICS

Leader mondiale nella progettazione e realizzazione di sistemi commerciali per la produzione di idrogeno

<https://www.hydrogenics.com/>



This project has received funding from the Fuel Cells and Hydrogen 2 Joint Undertaking under the European Union's Horizon 2020 research and innovation programme under grant agreement No 779469







# Visjoner for hydrogen og vind i Finnmark

- Hydrogen i vinden, 21.03.2019



# Agenda

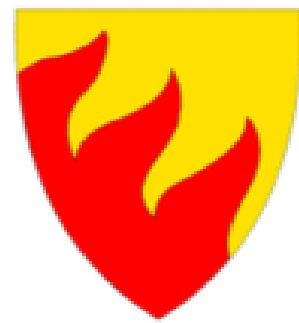
Visjoner for hydrogen og vind i Finnmark

---



# Varanger Kraft

## Konsernstruktur



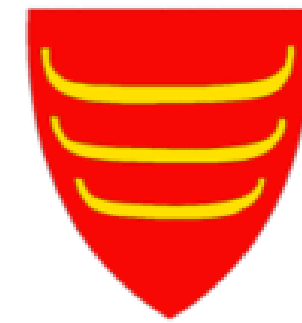
**Sør-Varanger**  
(31,25 %)



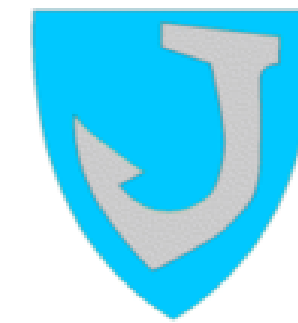
**Vadsø**  
(21,87 %)



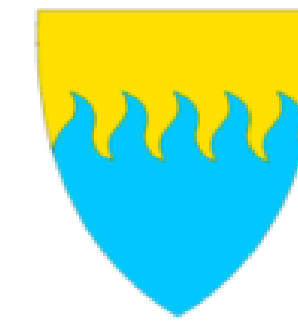
**Vardø**  
(12,50 %)



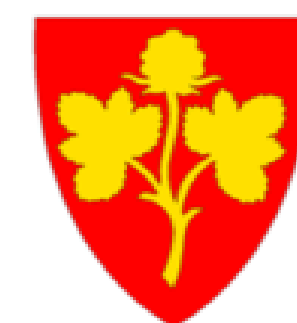
**Tana**  
(12,50 %)



**Båtsfjord**  
(9,38 %)



**Berlevåg**  
(6,25 %)



**Nesseby**  
(6,25 %)

**Varanger Kraft AS**  
~160 ansatte  
Omsatte for 750 MNOK i 2018

**VK Vind AS**  
191 GWh  
(>400 GWh fra 2021)

**Pasvik Kraft AS**  
420 GWh  
4 vannkraftverk

**VK Nett AS**  
3300 km nett  
16000 leveransepunkt

**VK Entreprenør AS**  
46 Ansatte

**VK Marked AS**  
13000 Kunder

**VK Utvikling AS**  
6000 Kunder

**VK Hydrogen AS**  
390 tonn H<sub>2</sub> pr/år  
kapasitet i 2020

# Bakgrunn

Nettsituasjon i Nord





# Raggovidda

Produksjon i verdensklasse | 200 MW Konsesjon

---

## Raggo 1

- ~191 GWh/år – 49% Kap.faktor
- 15 turbiner
- 45 MW
- Capex 604 MNOK (2014)

**103,4 MW ubrukt konsesjon**

## Raggo 2

- ~215 GWh AEP
- 12 turbiner
- 51,6 MW
- Capex ~450 MNOK





# Løsningen på innestengt kraft?

- Hydrogenproduksjon
- Objektiv – Varanger Kraft
  - Bidra til dekarbonisering
  - Utnytte vindressurs i verdensklasse
  - Selge hydrogen – drivstoff, industri
- Objektiv – EU: Haeolus
  - Energilagring
  - Vindpenetrasjon i energisystemer
  - Mini-grid / Nettbalansering
  - Remote location





# Haeolus

Partnere

---



**Varanger Kraft**

Vindpark



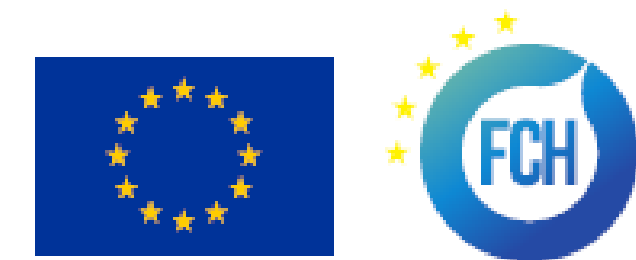
**Hydrogenics**

Leverandør av elektrolyser og brenselcelle



**SINTEF**

Prosjektkoordinator



**EU, FCH2 JU**

Sponsor



**Univeristy UnniSannio**

Dynamisk modellering



**Tecnalia University**

Systemdesign



**Universtiy UBFC**

Diagnose og prognoser for systemet



**KES**

Fjernstyring





# Haeolus

## Teknologi

- PEM - elektrolysør
- 2.5 MW
  - **Verdens største elektrolysør koblet til vindpark**
- Kapasitet – 1 tonn/døgn
- 100 kW Brenscelle

## Prosjekt

- Produsere min. 120 tonn
- Produsere strøm tilbake til nett
- Autonomt og fjernstyrt



# Haeolus

Bygning og elektrolysør

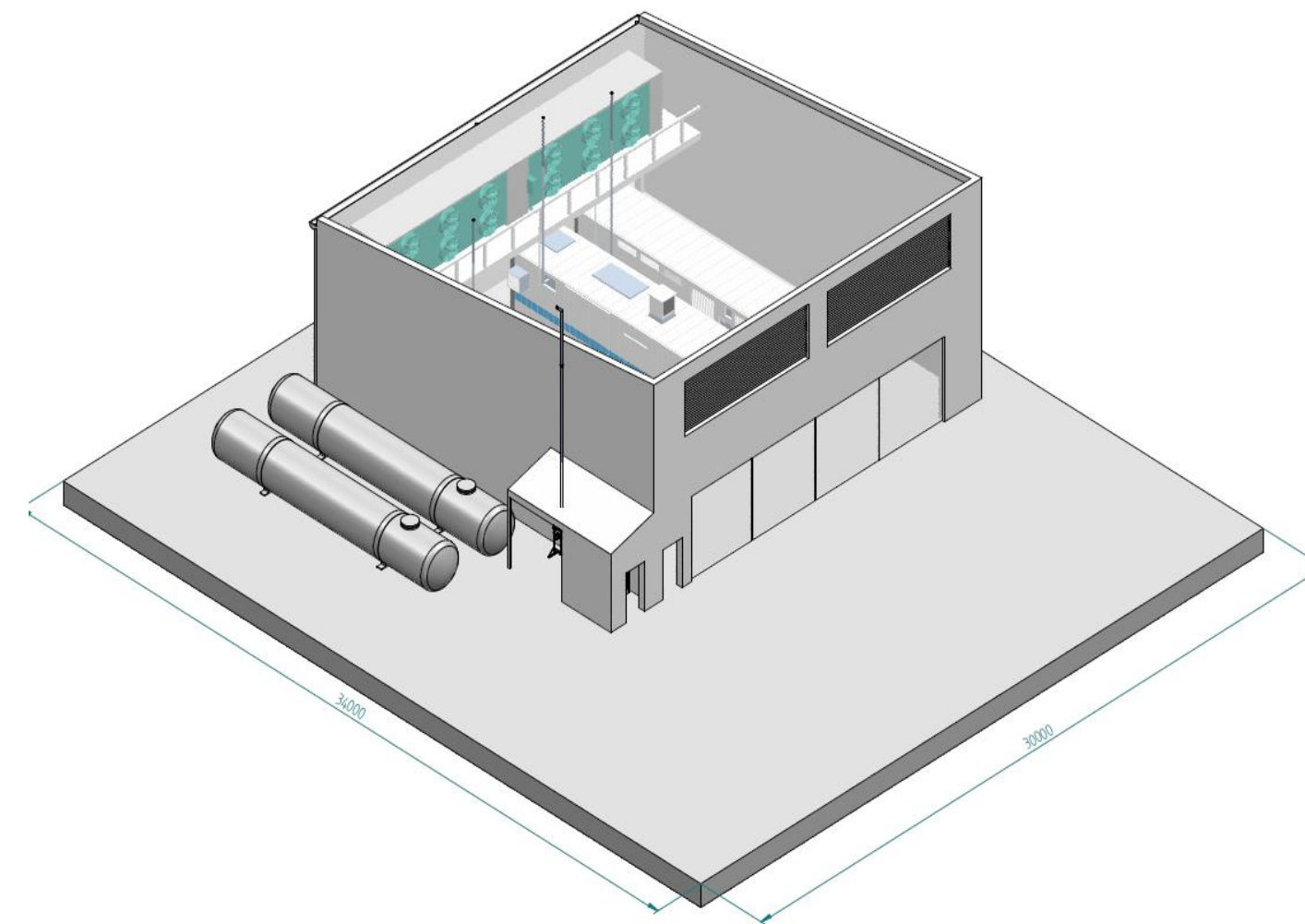


Plassering

**Berlevåg, Revnes**

Bra logistikkmuligheter for sjøtransport

Stort areal tilgjengelig



Bygning

**325 m<sup>2</sup>**

140 kg lagring ved 30 bar (oppstartsløsning)

Naturlig ventilasjon



PEM elektrolysør-stack

**2.5 MW fra Hydrogenics**

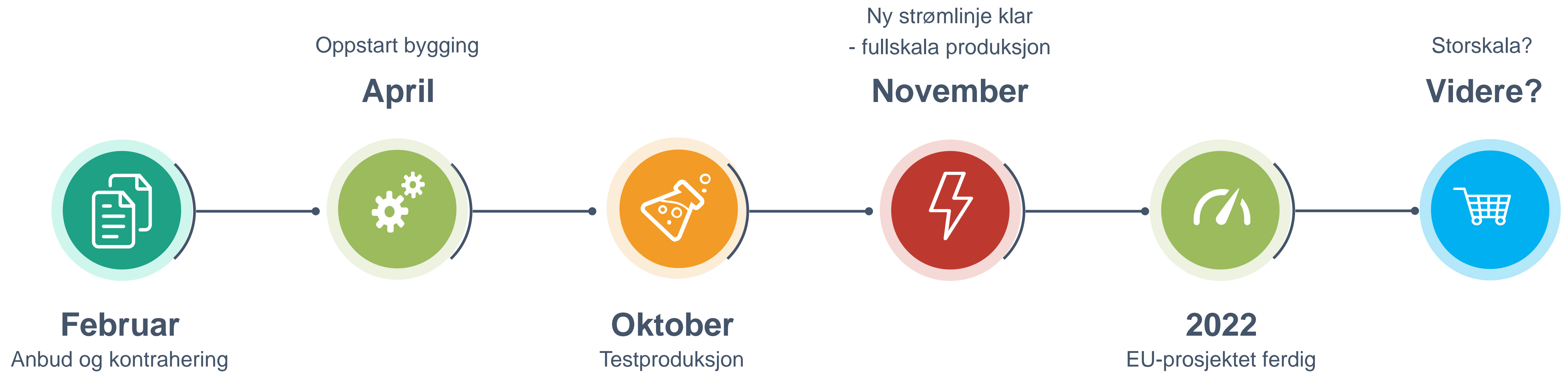
Start/stop <30 sekund

Størrelse: minikjøleskap



# Tidsplan

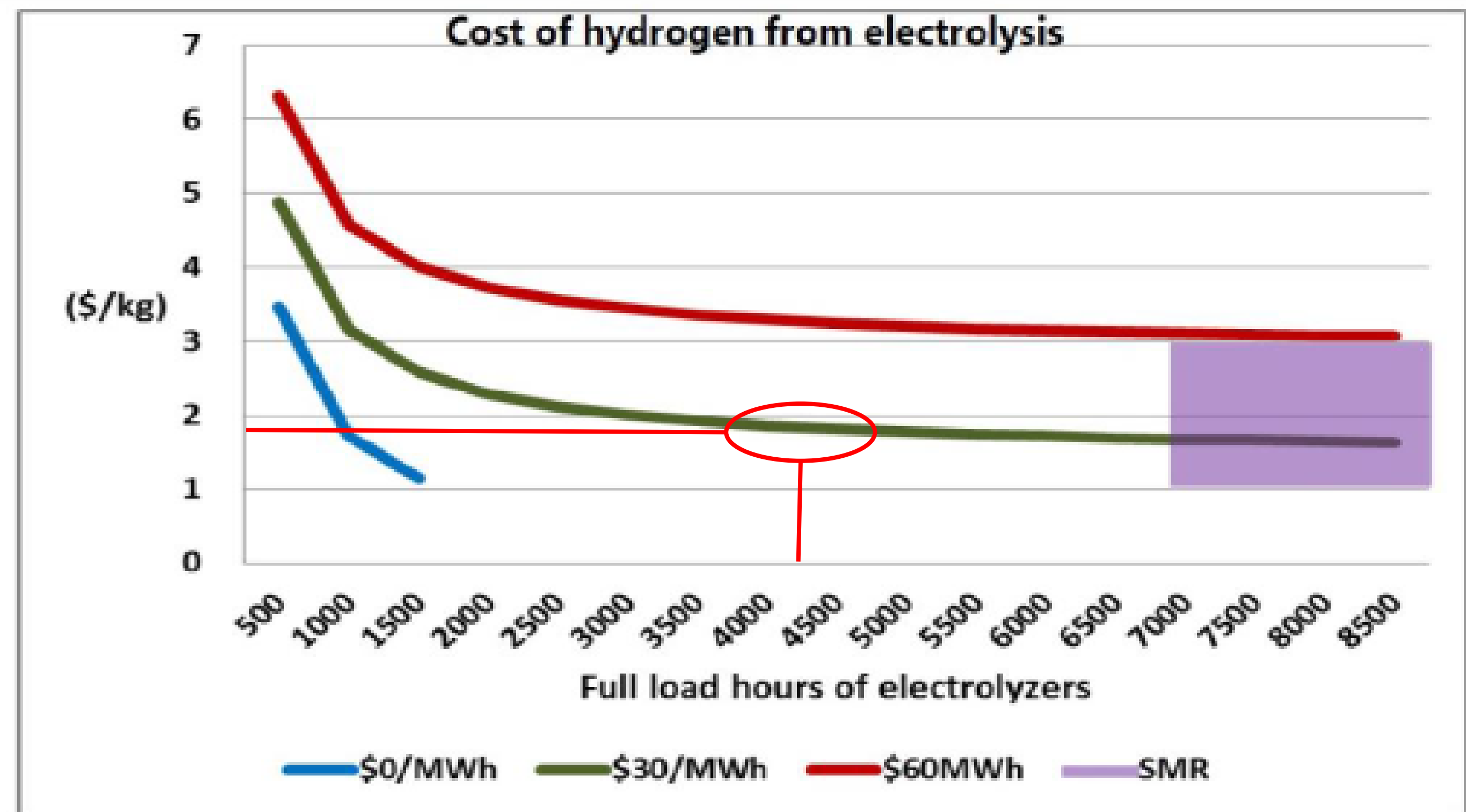
Haeolus – Oppstart 2019



# Våre fordeler

- Miljøaspektet
  - I dag: ~95% av  $H_2$  fra karbonholdige kilder
  - Vind til hydrogen = grønn hydrogen!
- Konkurransefortrinn
  - Billig strøm
  - Vindforhold i verdensklasse
  - “Grønneste”  $H_2$  i verden
  - Konkurransedyktig pris?
  - Tidlig ute

## Producing hydrogen from cheap solar and wind power

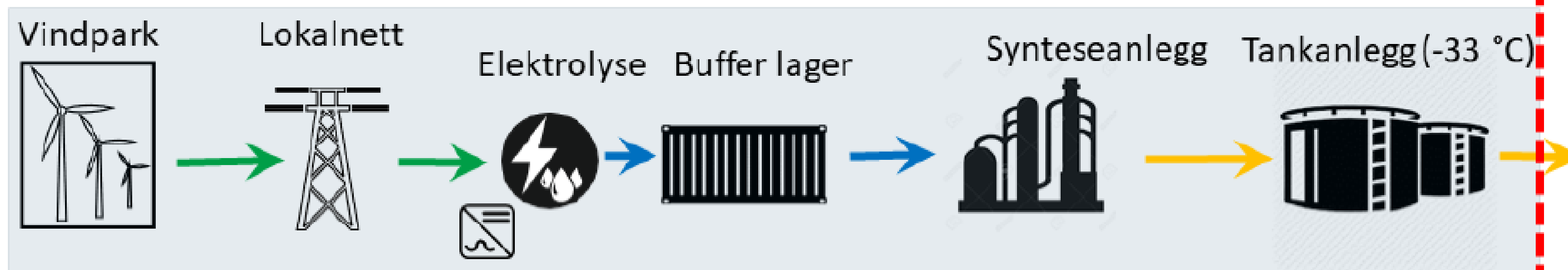


Kilde: IEA Report October 2017 - Producing ammonia and fertilizers: new opportunities from renewables

# Raggstrøm

Hydrogen til Ammoniakk | Elektrifisering av Svalbard

Prosessering N<sub>2</sub> fra luft



# H<sub>2</sub>-produksjon i Finnmark

Enormt potensiale

---

## Vind til hydrogen

105 MW til H<sub>2</sub>-produksjon = ~16.000 tonn H<sub>2</sub> / år

49% kapasitetsfaktor

Tilnærmet null “carbon footprint”







## Varanger Kraft Hydrogen

Christian Bue

[christian.bue@varanger-kraft.no](mailto:christian.bue@varanger-kraft.no)

+47 982 88 083



## Varanger Kraft Vind

Tore Martinsen

[tore.martinsen@varanger-kraft.no](mailto:tore.martinsen@varanger-kraft.no)

+47 982 88 034



## Varanger Kraft, CEO

Terje Skansen

[Terje.skansen@varanger-kraft.no](mailto:Terje.skansen@varanger-kraft.no)

+47 901 42 554

# KONTAKT OSS

[WWW.VARANGER-KRAFT.NO](http://WWW.VARANGER-KRAFT.NO)

# A Feature-based Prognostics Strategy For PEM Fuel Cell Operated Under Dynamic Conditions

Meiling Yue  
FEMTO-ST, FCLAB, CNRS  
Univ. Bourgogne Franche-Comté  
Belfort, France  
meiling.yue@femto-st.fr

Zhongliang Li  
LIS Laboratory  
Aix-Marseille University  
Marseille, France  
zhongliang.li@lis-lab.fr

Robin Roche  
FEMTO-ST, FCLAB, CNRS  
Univ. Bourgogne Franche-Comté  
Belfort, France  
robin.roche@utbm.fr

Samir Jemei  
FEMTO-ST, FCLAB, CNRS  
Univ. Bourgogne Franche-Comté  
Belfort, France  
samir.jemei@univ-fcomte.fr

Nouredine Zerhouni  
FEMTO-ST, FCLAB, CNRS  
Univ. Bourgogne Franche-Comté  
Besançon, France  
zerhouni@ens2m.fr

**Abstract**—Proton exchange membrane (PEM) fuel cell has been widely used in diverse applications, especially in automotive field. However, durability and cost are two principle barriers to take PEM fuel cell into wide commercial use. The discipline of prognostics and health management (PHM) tends to help against this problem. PHM aims at deploying predictive maintenance and anticipating degradation mitigation strategies for PEM fuel cell. This paper focuses on the prognostics of PHM and an adapted data-driven fuel cell prognostics approach based on multiplicative feature decomposition and echo state network is proposed to predict the fuel cell degradation behaviour under dynamic operation conditions. Experimental data is used to verify the effectiveness of the proposed algorithm.

**Keywords**—Echo state network, Feature decomposition, PEM fuel cell, Prognostics

## I. INTRODUCTION

Thanks to the reliable use of hydrogen energy, fuel cell technology has seen a promising future in vehicular applications. Proton exchange membrane (PEM) fuel cell is the most versatile fuel cell type used in automotive field thanks to its high energy density, relatively low operation temperature and corrosion. However, a central issue holding back the critical achievement of fuel cell electric vehicles is the durability problem. Analysis of the on-road fuel cell electric vehicles data provided by National Renewable Energy Laboratory has shown that the maximum projected durability has been more than quadrupled over the last ten years, increasing from 950 hours in 2006 to 2,500 hours in 2009, and reaching 4,100 hours in 2016 [1]. In 2016, the Department of Energy (DOE) Fuel Cell Technologies Office made the decision to increase the ultimate target for fuel cell durability from 5,000 hours to 8,000 hours, which effectively expands the metric so that vehicles can achieve 150,000 miles in slower-speed driving conditions [2]. An increasing demand emerges in improving the durability of PEM fuel cell systems.

Prognostics and health management (PHM) is a newly emerging discipline that performs predictive maintenance and have started to be applied in PEM fuel cell applications. It is deployed to offer feasible solutions to predict and protect the integrity of the system and to design control strategies to avoid unanticipated operational problems leading to performance deficiencies, degradation, and adverse effects to mission safety [3]. The predictive nature of prognostics provides accurate estimation of the remaining useful life (RUL) of the system, based on which control and management strategies on the operation conditions could be properly designed to avoid further degradation of the system. As PEM fuel cell system is such a complex multi-physical system whose degradation behaviour is difficult to model analytically, data-driven prognostics has been widely used in fuel cell PHM studies thanks to its model-free nature [4]-[10]. Without any knowledge of physical or chemical phenomenon, data-driven prognostics method is able to derive the behaviour model directly from the available data. To perform prognostics for PEM fuel cells, the methods developed in most works are validated with “in-lab” experimental data obtained under long-term static operation conditions [10]. In these studies, the system response has often been considered as the health index. However, practically the PEM fuel cells are rarely operated with constant current and the operation conditions varied according to the utilisation in automotive applications. In this case, the dynamic response of the system can no longer be used directly for prognostics [11].

To solve the difficulties of the prognostics for PEM fuel cell operated under dynamic operation conditions, a novel prognostics strategy is proposed in this paper. The degradation behaviour of the PEM fuel cell is supposed to be multiplicative and a feature extraction method is applied to select the degradation feature as the performance indicator, which is then used as the training dataset to train a recurrent neural network (RNN) and get the degradation behaviour model. Among variable RNNs applied in time series forecasting problems, echo state network (ESN) is adapted here to perform prognostics for

the PEM fuel cell degradation given the reason that it is simple and fast.

The paper is organized as follows: the proposed prognostics strategy based on feature extraction and echo state network is proposed in Sections II and is validated by a long-term degradation experimental dataset in Section III, results are presented and discussed in the same section. This work is concluded in Section IV.

## II. PROGNOSTICS UNDER DYNAMIC OPERATION CONDITION

The proposed prognostics strategy consists of two steps: time series feature extraction and prognostics, as shown in Fig. 1. The measure signal is firstly processed and decomposed into several components, whereas the trend component is used as the extracted degradation feature. The selected feature is then be trained through echo state network. When the input is no long available, the predicted values are obtained based on the previous inputs and the trained network model. Then RULs are calculated by defining a corresponding end-of-life (EOL) threshold.

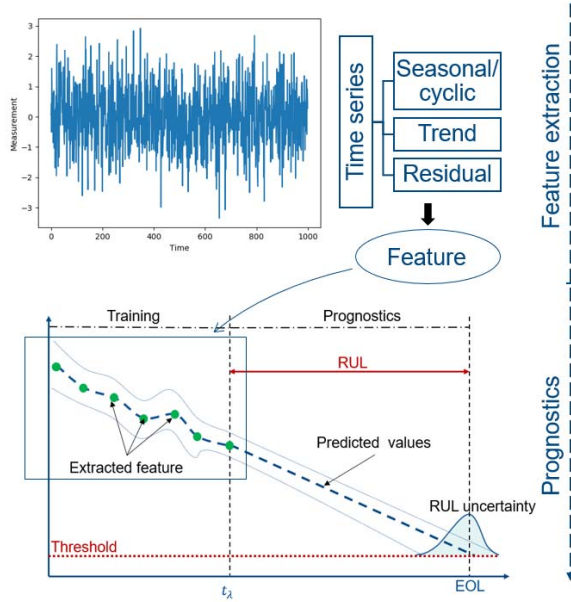


Fig. 1. Proposed prognostics strategy

### A. Time series feature extraction

For time series data, in many cases, it could be decomposed into trend, seasonal or cyclic pattern and the residual. A trend exists when there is a long-term, linear or non-linear, increasing or decreasing tendency in the data, which sometimes could be regarded as a “changing direction”. A seasonal pattern means that the time series is affected by seasonal factors, which is always of fixed and known frequency, while cyclic pattern refers to the data exhibit rises and falls that are not of a fixed frequency.

Decomposition is primarily used for time series analysis and forecasting, which can split the time series into different components with different features: trend, seasonality, cycles, etc. The time series, therefore, could be decomposed in a structured way, which simplified the forecasting and prediction

problem comparing to the methods featured by great model complexity and parameter uncertainty. For example, a multiplicative model suggests that the components in a time series could be multiplied together as follows:

$$y(t) = Level * Trend * Seasonality * Residual \quad (1)$$

and an additive decomposition can be written as:

$$y(t) = Level + Trend + Seasonality + Residual \quad (2)$$

The additive decomposition is used when the magnitude of the seasonality does not vary with the level of the time series and the multiplicative model is used when the time series increases in magnitude and the seasonal variation increases as well. The choice of decomposition model should be made by reconstructing the time series with decomposed trend and seasonal elements to find the one that can better explain the variations of the original signal.

For a PEM fuel cell operated under dynamic operation conditions, the component “Trend” can then be extracted as a degradation indicator as the power provided by the fuel cell can no long reach the same level as its initial state due to ageing phenomenon. After obtaining a degradation-oriented feature, the next step is to train the available measurements and predict the future values to calculate the RULs using for anticipative maintenance.

### B. ESN adapted for prognostics purpose

The Echo State Network (ESN) is a novel recurrent neural network proposed by Jaeger in 2001 [12] and has been widely applied for time series predictions. ESN is proposed based on traditional recurrent neural networks, in which the concept of “reservoir pool” is introduced that can cope well a wide range of nonlinear systems. ESN has demonstrated high prediction performance. Comparing with traditional neural networks, it can also overcome the problems of large computational complexity, low training efficiency and local optimization. The implementation of ESN is shown in Fig. 2.

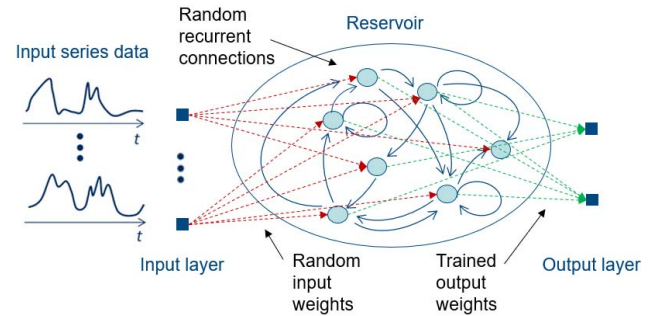


Fig. 2. ESN structure illustration

The state update model of ESN is written as:

$$\tilde{u}(t) = f(w_{res}u(t-1) + w_{in}x(t)) \quad (3)$$

$$y(t) = g(w_{out}u(t)) \quad (4)$$

where  $x(t)$  and  $y(t)$  are the input and output,  $u(t)$  is the internal state in the reservoir and  $\tilde{u}(t)$  is its update,  $\tilde{u}(t) = u(t) - u(t-1)$ ,  $w_{in}$  is the input weight matrix,  $w_{res}$  is the recurrent weight matrix in the reservoir and  $w_{out}$  is the output weight matrix. The  $\tanh$  function is generally adopted as the activation function  $f(\bullet)$  of the reservoir, and  $g(\bullet)$  of the output layer could be defined with a simple linear function such as  $g(\bullet) = 1$ .  $w_{in}$  and  $w_{res}$  are initialized randomly and they are constant so that there is no need to train them. Only  $w_{out}$  is going to be trained by linear regression.

In prediction problem, a training window and a prediction window are usually needed to be selected. Training window length is the length of the input sequence and the prediction window length is how many steps are going to be predicted following the input sequence. In fuel cell prognostics application, the training window length is decided according to the volume of available input data and the prediction window is set as 1 when a one-step ahead prediction is conducted.

To adapt ESM for prognostics purpose, the regular implementation of one-step ahead prediction is modified in the test phase in order to perform multi-time step prediction, shown in Fig. 3. Supposing the available measurements are until  $x_t$ , the data with a length of  $l$  is used as the input sequence and one predicted value is the model output. To continue the prediction, the predicted value of the last step is reinjected to the input sequence of the next step, so that the input sequence is reformulated with a predicted value. Repeat this process until the test phase is finished.

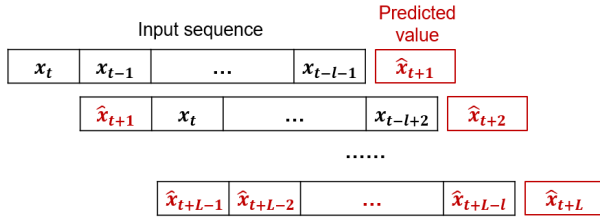


Fig. 3. ESN adapted for prognostics purpose

### III. RESULTS

The proposed prognostics strategy is verified in this section with experimental dataset. Results are demonstrated and discussed.

#### A. Experimental data description

The fuel cell stack confronted in the experiment is a 73.5 W PEM fuel cell stack, which is designed with the structure of open cathode and dead-end anode. A long-term test aiming at evaluating the degradation of the fuel cell stack for transport application has been launched in FCLAB Research Federation [9]. Some parameters of the operation condition are listed in Table I. The degradation test has run for 1750 hours with a current profile obtained from the real motive application, which varied from 0 to 8 A. Some details of the current evolution are shown in Fig. 4.

TABLE I. FUEL CELL STACK PARAMETERS

Number of cells	15
Active surface area	33.625 cm <sup>2</sup>
Temperature	25-72 °C
Current density	0-0.238 A/cm <sup>2</sup>
Anodic relative humidity	0
Cathodic relative humidity	45-55 %
Maximum allowable pressure difference between the anode and the cathode	0.35 bar
Pressure at air inlet	atm
Pressure at hydrogen inlet	1.35 bar

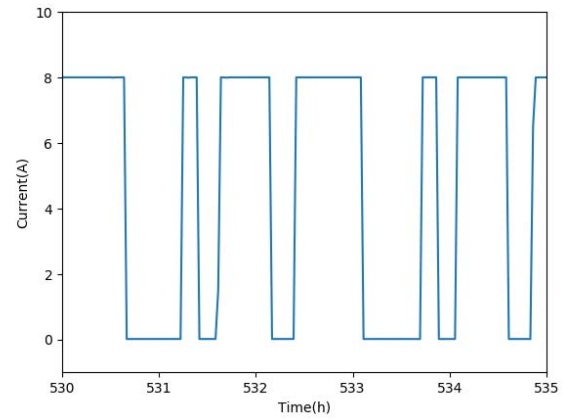


Fig. 4. Current profile

The measured stack voltage is plotted in Fig. 5 and details of the stack voltage corresponding to the current length of Fig. 4 is plotted in Fig. 6.

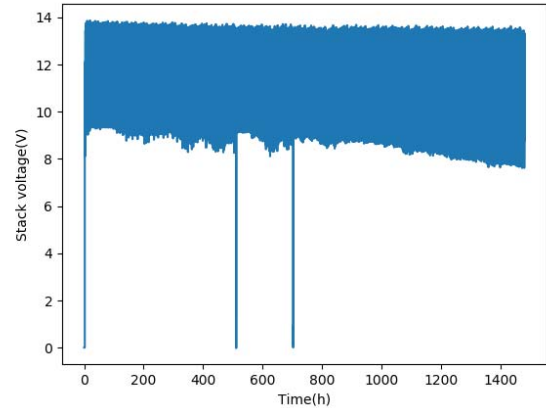


Fig. 5. Evolution of the fuel cell stack voltage

#### B. Feature extraction results

As the fuel cell is operated under dynamic conditions, the



trend, rather than the magnitude of the stack voltage, is the key element to determine the degradation of the fuel cell. As the magnitude of the time series may change due to ageing phenomenon, multiplicative decomposition is used to decompose the signal into trend, seasonal values and residual values, as shown in Fig. 7.

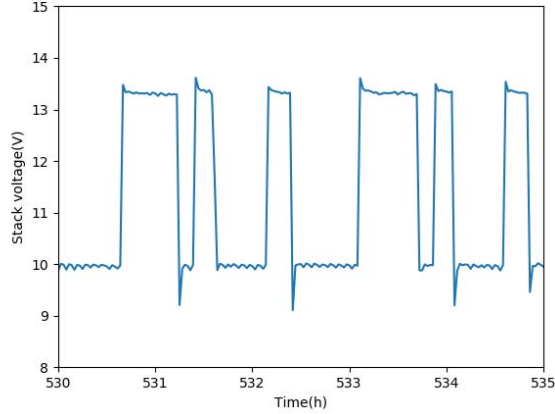


Fig. 6. Details of the stack voltage corresponding to the current length of Fig. 4

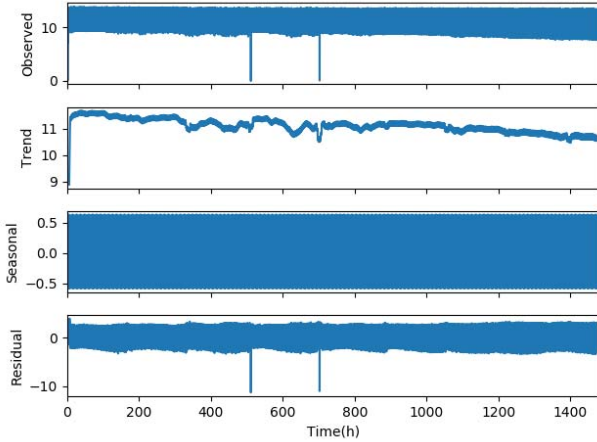


Fig. 7. Multiplicative decomposition result

In the decomposition results, the trend refers to the decreasing value of the time series, the seasonal values refer to the repeating short-term cycles in the series and the residual values refer to the random variation in the series, which in our case, are the noise in the voltage measurement. Therefore, to indicate the degradation of the stack, the trend of the decomposition is extracted as the degradation feature and will be used to train the prognostics network to calculate the RULs, shown in Fig. 8.

### C. Prognostics results

The data described above is used as the input of ESN. To validate the proposed method, the first 30000 points (60% of the total) are used as the training set. The number of neurons is set as 1000 and the leaking rate is 0.5. After training the available

data, multiple time steps prediction is done according to the proposed prognostics strategy. As the initial weights in ESN are randomly allocated, to evaluate the uncertainty of the prognostic strategy, the same procedure is repeated 100 times to demonstrate the confidence level of the results. Fig. 9 shows the 100 prediction results. Due to the randomly allocated weights of ESN, the predictions cannot have the same trace (represented by the coloured lines).

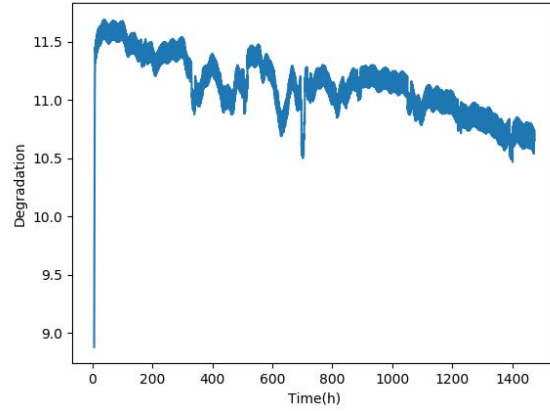


Fig. 8. Degradation feature extraction result

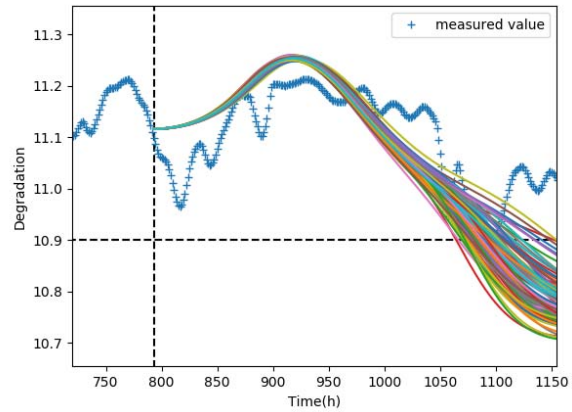


Fig. 9. Prediction results using 60% training set (Colored thin lines: predicted results of 100 repetitions)

Assuming the prediction results follow standard Gaussian distribution, the confidence interval of the predictions can be calculated as:

$$\text{Confidence interval } (\pm) = \overline{\hat{x}_{t+L}} \pm \theta * \sigma_{t+L} \quad (5)$$

where  $\overline{\hat{x}_{t+L}}$  is the mean value of the predictions at time instant  $t + L$ ,  $\theta$  is the critical value related to the confidence level and  $\sigma_{t+L}$  is the standard deviation of the predictions at  $t + L$ . For a confidence level of 95%,  $\theta$  equals to 1.96. The mean value and the corresponding confidence intervals of the prognostics results in Fig. 9 are shown in Fig. 10.

It can be seen from the results that the confidence interval of 95% of the multi-time step long-term prediction have enclosed the real end-of-life of the measured values.

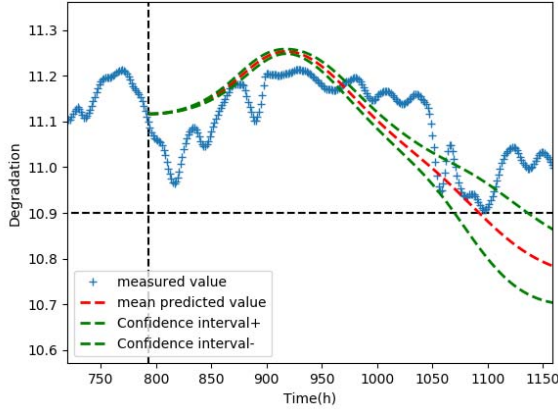


Fig. 10. Mean prediction results and confidence intervals of 95%

#### D. Result evaluation

Root Mean Square Error (RMSE) is used to in this paper to evaluate the prediction results, which is commonly used to quantify the difference between a forecasted signal and its real target. It is calculated as:

$$RMSE = \sqrt{\frac{\sum_{k=1}^n (x_t - \hat{x}_t)^2}{n}} \quad (6)$$

and the normalized RMSE is calculated as:

$$NRMSE = RMSE / (\max(\hat{x}_t) - \min(\hat{x}_t)) \quad (7)$$

To compare the results, the prognostics method based on particle filtering proposed in [13] has also been implemented to get the prediction results. The state model used for predicting is written as:

$$x_{k+1} = -\alpha \cdot \ln\left(\frac{t_{k+1}}{t_k}\right) - \beta \cdot (t_{k+1} - t_k) + x_k \quad (8)$$

The average RMSE and NRMSE of the results of the both methods are calculated by starting prediction at the same time instant indicated in Fig. 9. They are compared in Table II.

TABLE II. RESULTS COMPARISON

Prognostics method	ESN	Particle filtering
Average RMSE	0.070	0.320
Average NRMSE	0.171	0.675

Dealing with the prognostics-oriented feature shown in Fig. 8, the ESN-based prognostics method has seen a better accuracy than the particle filtering method due to the reason that the ESN can better catch the internal characteristics of the data with a training process, while the particle filtering method can only reach a good prediction when the state space model is properly

chosen. Besides, the implementation time of ESN is nearly 10 times faster than running particle filtering.

#### IV. CONCLUSION

This paper has proposed a feature-based prognostics strategy for predicting the degrading performance of the PEM fuel cell operated under dynamic conditions. A multiplicative decomposition is used to extract the degradation trend from the experimental data and a prognostics method based on adapted ESN is used to train the behaviour model and predict the future states. The prediction results are compared with the particle filtering prognostic method and the results show that the proposed prognostics strategy has reached better accuracy and shorter implementation time.

For the perspectives, the proposed prognostics method can be used to estimate RULs and perform predictive maintenance in other applications, for example, electrolyzers and/or the components. Further efforts will be made to improve the robustness of the proposed method and discussions on prognostics horizon and failure threshold will be undertaken in the authors' future work.

#### ACKNOWLEDGMENT

This work received funding from the Fuel Cells and Hydrogen 2 Joint Undertaking under the project HAEOLUS, grant agreement No. 779469 (<https://www.haeolus.eu>). This work was also supported by the project PHYTie (2016Y-04574) funded by the French region of Bourgogne Franche-Comté and the Project PRODIG (1494C0045) funded by French Environment and Energy Management Agency.

#### REFERENCES

- [1] Jennifer Kurtz, Sam Sprik, Chris Ainscough, and Genevieve Saur. National renewable energy laboratory: Fuel cell electric vehicle evaluation.
- [2] Adria Wilson, Jason Marcinkoski, and Dimitrios Papageorgopoulos. On-road fuel cell stack durability – 2016.
- [3] Marine Jouin, Rafael Gouriveau, Daniel Hissel, Marie-Cécile Marion-Péra, and Noureddine Zerhouni. Prognostics and health management of pemfc - state of the art and remaining challenges. *International Journal of Hydrogen Energy*, 38:15307–15317, 11 2013.
- [4] Rui Ma, Tao Yang, Elena Breaz, Zhongliang Li, Pascal Briois, and Fei Gao. Data-driven proton exchange membrane fuel cell degradation prediction through deep learning method. *Applied Energy*, 231:102–115, 2018.
- [5] Kamran Javed, Rafael Gouriveau, Noureddine Zerhouni, and Daniel Hissel. Prognostics of proton exchange membrane fuel cells stack using an ensemble of constraints based connectionist networks. *Journal of Power Sources*, 324:745 – 757, 2016.
- [6] Simon Morando, S Jemei, Rafael Gouriveau, Noureddine Zerhouni, and Daniel Hissel. Fuel cells prognostics using echo state network. In *IECON Proceedings (Industrial Electronics Conference)*, pages 1632–1637, 11 2013.
- [7] Rosa Silva, Rafael Gouriveau, S Jemei, Daniel Hissel, Loïc BOULON, K Agbossou, and Nadia Yousfi-Steiner. Proton exchange membrane fuel cell degradation prediction based on adaptive neuro-fuzzy inference systems. *International Journal of Hydrogen Energy*, 39:11128–11144, 07 2014.
- [8] M. Ibrahim, N. Y. Steiner, S. Jemei, and D. Hissel. Wavelet-based approach for online fuel cell remaining useful lifetime prediction. *IEEE Transactions on Industrial Electronics*, 63(8):5057–5068, Aug 2016.
- [9] Z. Li, S. Jemei, R. Gouriveau, D. Hissel and N. Zerhouni, "Remaining Useful Life Estimation for PEMFC in Dynamic Operating Conditions,"

- 2016 IEEE Vehicle Power and Propulsion Conference (VPPC), Hangzhou, 2016, pp. 1-6. doi: 10.1109/VPPC.2016.7791762
- [10] Simon Morando, Samir Jemei, Daniel Hissel, Rafael Gouriveau, and Nouredine Zerhouni. Proton exchange membrane fuel cell ageing forecasting algorithm based on echo state network. *International Journal of Hydrogen Energy*, 42(2):1472 – 1480, 2017.
- [11] Z. Li, Z. Zheng and R. Outbib, "Adaptive Prognostic of Fuel Cells by Implementing Ensemble Echo State Networks in Time-Varying Model Space," in *IEEE Transactions on Industrial Electronics*, vol. 67, no. 1, pp. 379-389, Jan. 2020. doi: 10.1109/TIE.2019.2893827
- [12] H. Jaeger, "The echo state approach to analyzing and training recurrent neural networks". Technical Report GMD Report 148, German National Research Center for Information Technology, 2001.
- [13] Marine Jouin, Rafael Gouriveau, Daniel Hissel, Marie-Cécile Péra, and Nouredine Zerhouni. Joint particle filters prognostics for proton exchange membrane fuel cell power prediction at constant current solicitation. *IEEE Transactions on reliability*, 65(1):336–349, 2016.

# LA OPORTUNIDAD DE LA HIBRIDACIÓN ENTRE LOS SISTEMAS EÓLICOS Y LOS DE HIDRÓGENO ALMACENAMIENTO Y SERVICIOS A LA RED

H<sub>2</sub>AΞOLUS



(\*) This project has received funding from the Fuel Cells and Hydrogen 2 Joint Undertaking under the European Union's Horizon 2020 research and innovation programme under grant agreement No 779469  
Any contents herein reflect solely the authors' view. The FCH 2 JU and the European Commission are not responsible for any use that may be made of the information herein contained



PhD Maider Santos-Mugica

19 Noviembre 2020

JORNADA

Internacional

online

Análisis Operativo  
de PARQUES EÓLICOS

>> 19 y 20 NOVIEMBRE de 2020

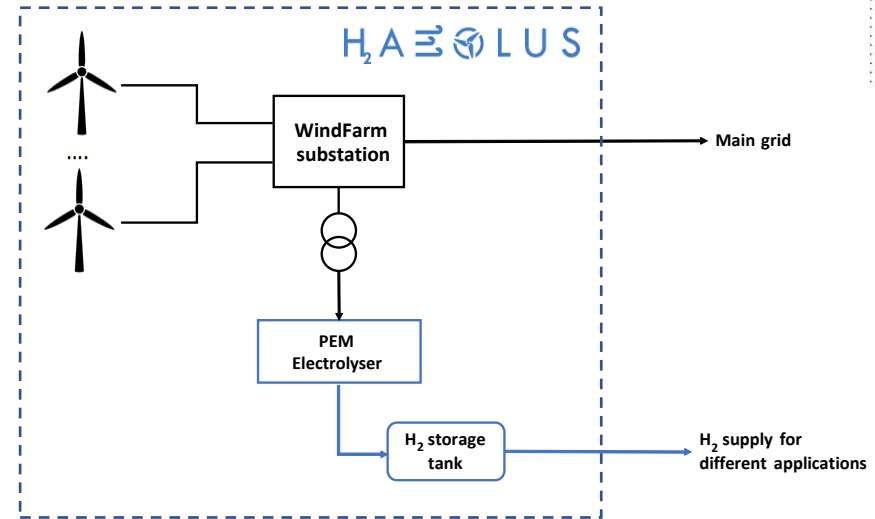


## Approach of the study

## HAEOLUS Project\* Concept

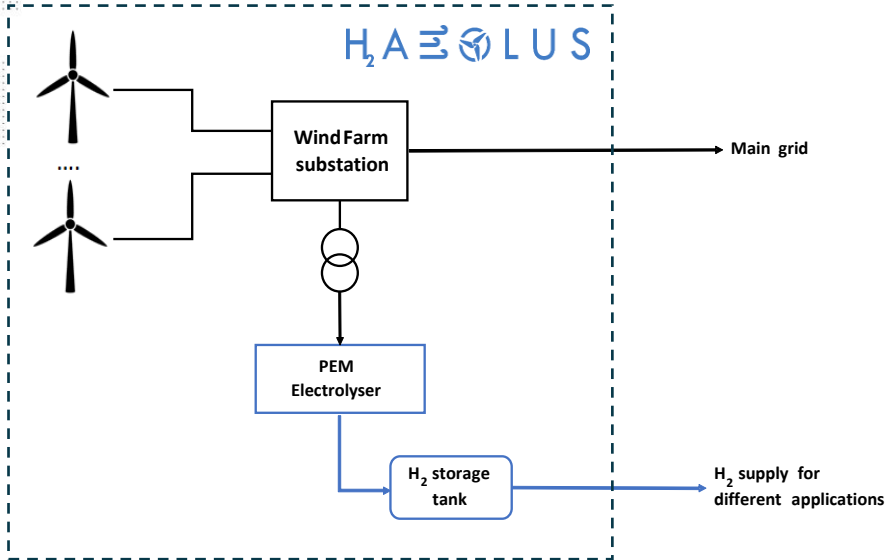
**New operation strategies that include the hybridisation of generation and storage technologies and the participation in new services for the different energy, regulation and flexibility markets, and H<sub>2</sub>**

- To analyse the operation of the Wind-H<sub>2</sub> system and the coordinated operation from a techno-economical perspective
- Asses the capacity to provide network services such as secondary regulation
- The LCOH<sub>2</sub> has been used as the economic profitability parameter
- The option of re-electrification by means of a fuel cell has not been considered
- The LCOH<sub>2</sub> when the integrated system operates at the market price will be used as a basis for comparison




$$LCOH_2 \left( \frac{\text{€}}{\text{kg}} \right) = \frac{NPV_{Base Case} - NPV_{wind+H_2}}{\sum_{i=1}^n H_2 production_i \cdot \left( \frac{1+e}{1+d} \right)^i}$$

## HAEOLUS Project Concept



## WIND FARM INPUT DATA

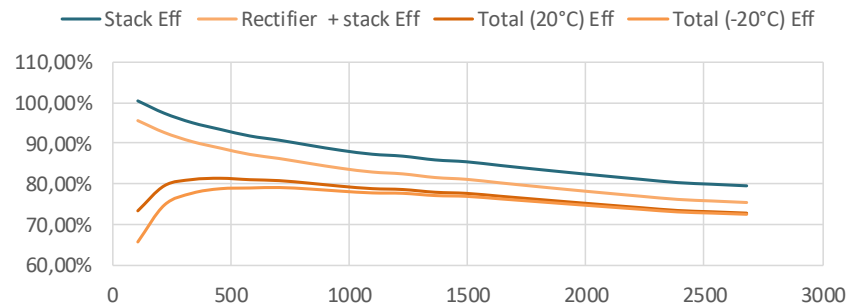
- **Real data from**
  - Raggovidda provided by  **VARANGER KRAFT**
  - Moncayuelo provided by Acciona
- **Wind Farm costs (CAPEX/OPEX)**
  - CAPEX: 0.9 €/kW, OPEX: 60 €/kW·year
  - Green tariffs in Norway
- **Energy prices affects to the H<sub>2</sub> production costs (€/t).**
  - The studies are based on 2017 data

## ELECTROLYSER

- Technical data provide by Hydrogenics

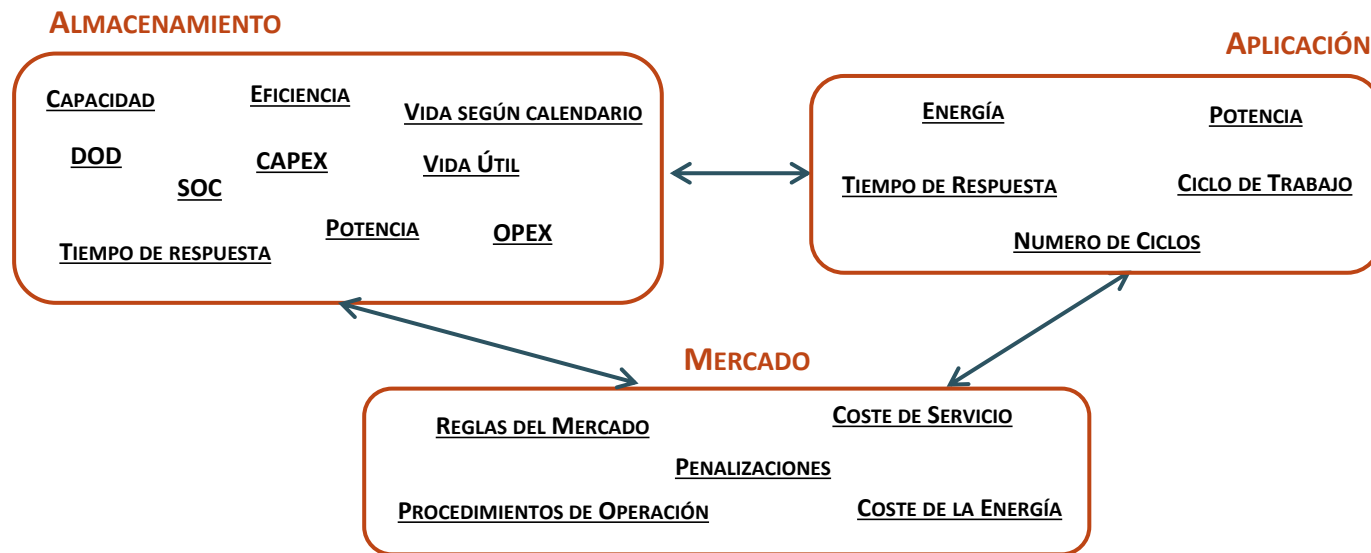
- Efficiency
  - Efficiency curves
  - Efficiency degradation (%/year)

**HYDROGENICS**  
SHIFT POWER | ENERGIZE YOUR WORLD



Electrolyser costs (€/kW)			
Year	CAPEX	OPEX	Overhaul costs (stack replacement)
2017	1328	60	354
2023	538	60	144

## Energy Storage systems analysis tools



- Techno-economic analysis of scenarios
- Battery technology selection and sizing
- Power flows studies

- Algorithms developments and testing
- Design and validation phase



## Scenarios

### Optimal H<sub>2</sub> production on the basis of spot prices

- Operation of the electrolyser based on the energy prices, producing H<sub>2</sub> when the energy prices is lower than a certain threshold.

### Secondary Frequency Regulation

- Participation of the wind farm in the secondary regulation market by modifying the consumption of the electrolyser

### Twofold objective

- Determine the LCOH<sub>2</sub> under different operation strategies and scenarios
- Analyze the optimal economical performance of the electrolyser within the wind farm

## Optimal Hydrogen Production

### Considerations

- H<sub>2</sub> production cost on the basis of:
  - CAPEX & OPEX of the electrolyser
  - The cost of electricity consumption
- The objective
  - Optimization of H<sub>2</sub> production costs
  - Production of at least 120t in 2,5 years

### Operation strategies

#### Fixed price threshold

- Different prices have been defined to determine the H<sub>2</sub> lowest sell price (≥120t-2,5years)

#### Variable price threshold

- A variable threshold has been defined so that the minimum tones (≈120t) are generated assuring that the electrolyser works everyday

## Secondary Frequency Regulation

### Considerations

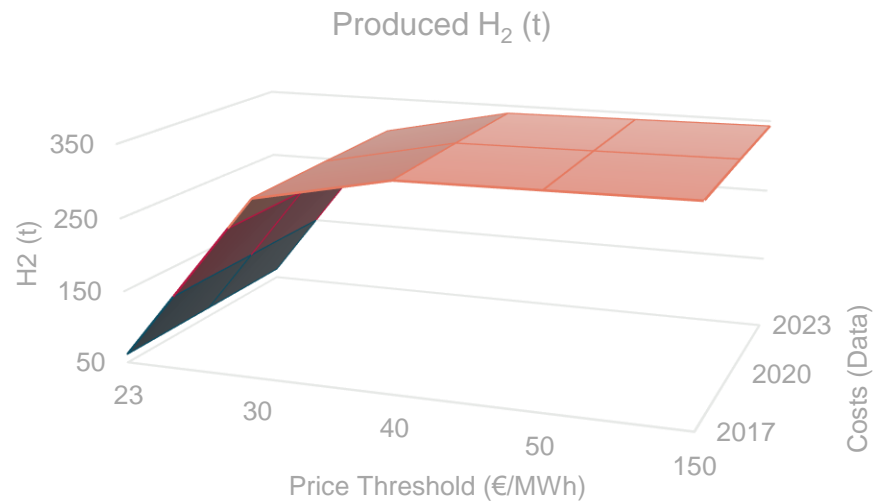
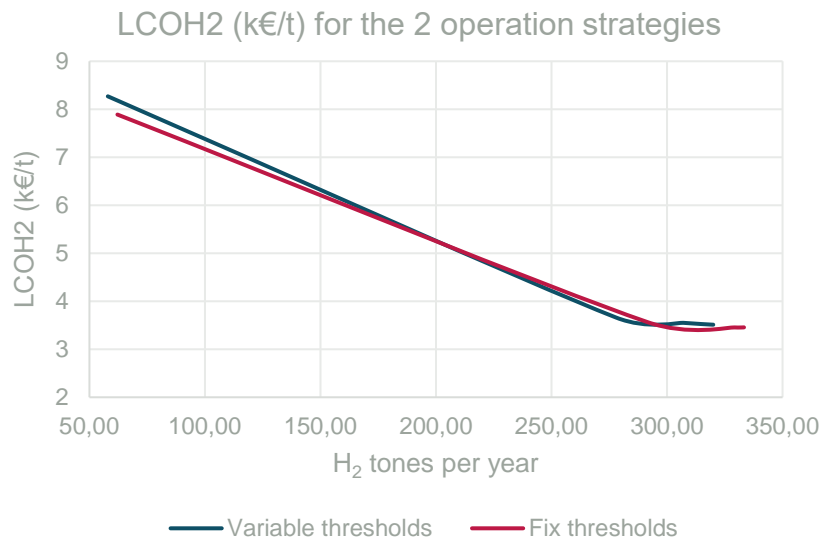
- Operation of the electrolyser based on frequency regulation service requirements

### Operation strategies

- Operation strategy as demand response system
- Adjusting the operation point of the electrolyser so that to offer the required power band for up and down regulation
- When upregulation is required the electrolyser reduces the consumption accordingly and when downregulation it increases the consumption

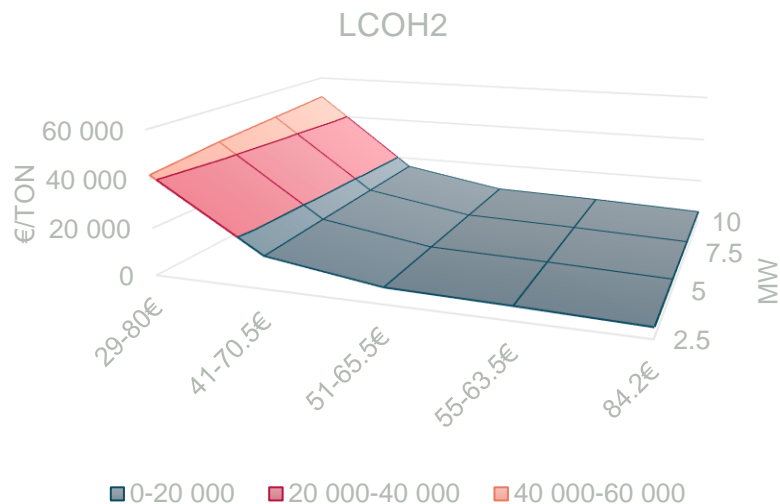
## Raggoidea

## Optimal Hydrogen production. Scenario 1: Fixed price vs Variable threshold (D5.1)

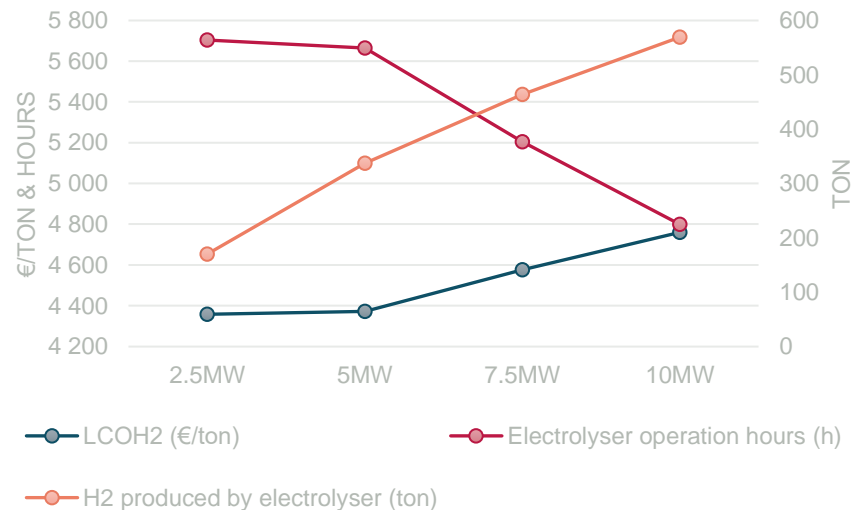


## Moncayuelo

### Optimal Hydrogen production. Fixed price threshold



### Frequency Regulation



## Conclusiones

Se ha realizado un análisis técnico-económico de un Sistema Integrado Eólico-H<sub>2</sub>

- Reducción de los costes de generación de H<sub>2</sub>
- Provisión de servicios de red => frecuencia

La operación del Sistema Integrado Eólico-H<sub>2</sub> necesita de un conocimiento profundo de ambos sistemas por separado y un control centralizado del Sistema como una única entidad

El Sistema Integrado Eólico-H<sub>2</sub> es capaz de proveer servicios de red tales como el control de frecuencia

### Viabilidad económica

- Los costes de operación difieren mucho dependiendo del caso de uso
- Producir la mayor cantidad de H<sub>2</sub> posible (gran peso del CAPEX). Siempre y cuando haya mercado para el H<sub>2</sub> generado
- Precios de H<sub>2</sub> competitivos
- Combinación de varias estrategias de operación

ESKERRIK ASKO  
GRACIAS  
THANK YOU  
MERCI



*maider.santos@tecnalia.com*

blogs.tecnalia.com



www.tecnalia.com



# Degradation identification and prognostics of proton exchange membrane fuel cell under dynamic load

Meiling Yue<sup>a,\*</sup>, Zhongliang Li<sup>b</sup>, Robin Roche<sup>c</sup>, Samir Jemei<sup>a</sup>, Noureddine Zerhouni<sup>d</sup>

<sup>a</sup> FEMTO-ST Institute, FCLAB, Univ. Bourgogne Franche-Comté, CNRS, Belfort, France

<sup>b</sup> LIS Laboratory, Aix-Marseille University, CNRS, Marseille, France

<sup>c</sup> FEMTO-ST Institute, FCLAB, Univ. Bourgogne Franche-Comté, UTBM, CNRS, Belfort, France

<sup>d</sup> FEMTO-ST Institute, FCLAB, Univ. Bourgogne Franche-Comté, ENSMM, CNRS, Belfort, France

## ARTICLE INFO

### Keywords:

Dynamic load  
Echo state network  
PEM fuel cell  
Health indicator  
Prognostics

## ABSTRACT

Proton exchange membrane (PEM) fuel cell has seen its recent increasing deployment in both automotive and stationary applications. However, the unsatisfied durability of the fuel cell has barriered in the way of its successful commercialization. Recent research on prognostics and predictive maintenance has demonstrated its effectiveness in predicting the system failure and improving the durability of the PEM fuel cell. This paper contributes to developing a degradation identification method for the PEM fuel cell operating under dynamic load. A degradation indicator is proposed based on the polarization model and the nonlinear regression method is applied to extract the degradation feature by segmenting the voltage measurement. To perform prognostics, a machine learning method based on a multi-step echo state network is developed, in which a sliding window is used to recursively reformulate the input sequence with predicted values in the prediction phase. The length of the sliding window is optimized by a genetic algorithm. The proposed method is verified on the experimental PEM fuel cell degradation data and improves the prediction performance on both accuracy and computation speed when comparing with other prognostics methods.

## 1. Introduction

Although fossil fuels still account for the majority of global energy demand, an energy transition is taking place. Hydrogen, as one of the cleanest fuels, has driven increasing attention around the world, which is regarded as a potential solution to today's environmental problems and resource exhaustion. Using hydrogen as the fuel, fuel cells can convert the chemical energy of the hydrogen into electrical energy directly with an efficiency up to 60 to 80%, while the by-product is only water. Among different types of fuel cells, proton exchange membrane (PEM) fuel cells, which take advantages of their fast start-up characteristics and low operating temperatures, are now commercially applied in a variety of stationary and embedded applications (Kong, Bressel, Hilaiet, & Roche, 2020).

On the road to the massive commercialization of PEM fuel cells, enhancing their durability is a prior challenge. The currently achieved durability of PEM fuel cells in automotive applications is around 4000–5000 h, while an 8000-hour lifetime is the ultimate goal (Kurtz & Dinh, 2018). Efforts have been made to investigate PEM fuel cell degradation mechanisms, especially for those operating under dynamic load (Keller, Ding, Müller, & Stolten, 2017; Luna, Usai, Husar, & Serra, 2017). For example, dynamic vehicle cycles in rated and idling conditions are

simulated in Wang, Huang, Yu, Wen, and Tu (2018), in which the PEM fuel cell is subjected to different degradation mechanisms causing varying stack voltage degradation rate. An accelerated degradation test is conducted in Han, Han, and Yu (2020) with normal vehicle driving cycles where signification degradation of the fuel cell has been observed. Varying thermal/humidity state, changing reactant demand and voltage cycling are identified as the principal reasons for PEM fuel cell degradation in dynamic operating conditions (Ren, et al., 2020).

Fuel cell performance loss can be easily observed by evaluating the stack voltage degradation and under constant operating conditions, it is measured directly. Various works on PEM fuel cell degradation estimation and prognostics have been conducted using the stack voltage as the direct health indicator (Jouin, Gouriveau, Hissel, Péra, & Zerhouni, 2014; Ma, et al., 2018). For example, Bressel et al. have proposed to estimate the health state of the PEM fuel cell using an observer-based prognostics algorithm and a state variable was created to track its degradation (Bressel, Hilaiet, Hissel, & Ould Bouamama, 2016). Wu et al. have predicted the stack voltage degradation of PEM fuel cells by developing a self-adaptive relevance vector machine, which is able to provide 20 h ahead forecast time (Wu, Breaz, Gao, Paire, & Miraoui, 2016). Both model-based and data-driven prognostics methods have

\* Corresponding author.

E-mail address: [meiling.yue@femto-st.fr](mailto:meiling.yue@femto-st.fr) (M. Yue).

been developed. For example, Pan et al. have proposed a model-based prognostics method based on Electrochemical Impedance Spectroscopy (EIS) measurement and an analytical equivalent circuit model, in which the parameters are obtained by linear regression (Pan, Yang, Wang, & Chen, 2020). A semi-empirical model-based prognostics method based on the adaptive unscented Kalman filter (AUKF) algorithm has been proposed in Liu, Chen, Zhu, Su, and Hou (2017) to improve the initial parameters setting problem. Recent researches have seen increasing interests in developing data-driven prognostics methods, which can reflect the inherent relationships between the input and output by simulating neural networks and avoid the study of complicated physical mechanisms. Data-driven methods have gradually become the main methodology for fuel cell prognostics due to their easy-to-use and flexible modelling properties (Liu, Chen, Hissel, & Su, 2019; Ma, et al., 2019; Ma, et al., 2020; Zhou, Al-Durra, Zhang, Ravey, & Gao, 2019). For example, echo state network (ESN) has been deployed to fuel cell prognostics in recent works thanks to its improve computation efficiency (Hua, Zheng, Péra, & Gao, 2020; Li, Zheng, & Outbib, 2020; Morando, Jemei, Hissel, Gouriveau, & Zerhouni, 2017). It was first applied to the prediction of the mean cell voltage of a degrading fuel cell in Morando, Jemei, Gouriveau, Zerhouni, and Hissel (2013) where the accuracy and the computation time are studied regarding the ESN parameters. Furthermore, for predicting the fuel cell health state, a multi-reservoir ESN has been developed in Mezzi, et al. (2018) to optimize the parameterization process and in Hua, Zheng, Péra, and Gao (2020), an advanced structure of using moving weight matrix has been proposed to improve the prediction accuracy. However, these studies are limited to the stack level and have not fully considered variable and dynamic loads that may exist in most automotive applications. In those cases, the degradation of the PEM fuel cells cannot be easily quantified using the measured stack voltage, whose value is also affected by system operating dynamics (Li, Jemei, Gouriveau, Hissel, & Zerhouni, 2016). A degradation indicator reflecting intrinsic degradation level in dynamic operating conditions is required. Some researchers have proposed hybrid degradation indexes in multi-time scales for online operation, however, they are limited to certain components and the accuracy is not satisfying (Liu, et al., 2020). Li et al. have proposed to represent the dynamic voltage response of the PEM fuel cell using linear parameter-varying models, and then obtained a real-time health indicator based on the online identified model (Li et al., 2020). However, the proposed health index in Li et al. (2020) only evaluates the overall performance loss and lacks the insights of fuel cell intrinsic degradation analysis. As the degradation of the fuel cell is related not only to the ageing phenomenon but also to the time-varying online operating conditions, developing a degradation identification method adapted to random external conditions is required.

This paper contributes to proposing an innovative degradation identification method for the PEM fuel cell operating in real time, especially under dynamic load. A degradation indicator is proposed based on the fuel cell polarization model, which is extracted using a non-linear regression process regardless of the operation conditions. Following that, a multi-step window-sliding ESN prognostics method is applied to predict the future evolution of the degradation indicator which is identified online. The parameterization of the ESN is optimized by a genetic algorithm that ensures improved prediction performance. The proposed degradation identification and prognostics methods are verified with a long-term operation experimental dataset of PEM fuel cell. As the measurements are obtained non-intrusively and the proposed method directly uses the output voltage signal, the prognostics can thus be performed in real time.

The main contributions of this paper can be summarized as follows:

1. A real-time degradation indicator of PEM fuel cells is proposed that can be extracted in both static and dynamic/random operation conditions;
2. An enhanced multi-step ESN-based prognostics strategy is adapted for the prediction purpose;

**Table 1**

Parameters of the studied fuel cell stack module.

Parameter	Value
Active surface	33.625 cm <sup>2</sup>
Number of cells	15
Nominal pressure at hydrogen inlet	0.35 bar
Nominal output power	73.5 W
Maximum operating temperature	75 °C
Maximum current	13.45 A (0.4 A/cm <sup>2</sup> )
Lowest permitted stack voltage	7.5 V
Pressure interval at hydrogen inlet	0.1 to 0.4 bar

3. The configuration of the proposed prognostics strategy is optimized through a genetic optimization algorithm;
4. The proposed prognostics strategy is validated by the long-term experimental PEM fuel cell degradation data.

The rest of the paper is organized as follows: Section 2 describes the long-term fuel cell degradation experiment and the dataset used to validate the proposed method. Section 3 explains the degradation identification method and Section 4 presents the enhanced multi-step window-sliding ESN prognostics strategy. Finally, Section 5 concludes the paper.

## 2. Data description

A long-term fuel cell degradation experiment was carried out in FCLAB Research Federation,<sup>1</sup> France, and supported by the PRODIG project, which received funding from region Aquitaine, France. The test bench consists of a hydrogen tank, a pressure reducer, purge valves and hydrogen inlet valves, DC electric loads, DC power modules, two fuel cell stack modules, a compact data acquisition system and a computer for control and data logging. The structure of the two-fuel-cell-stack-module is shown in Fig. 1. One of the stack modules is used for the dynamic load test, which is supposed to be applied in electric bicycles and is, therefore, tested using a dynamic load profile acquired in real operating conditions. The fuel cell stack is designed with an open cathode and dead-end anode structure and a 24 Vdc air fan is integrated with the stack for air supply and temperature regulation. The speed of the air fan is regulated by varying the duty cycle of an input PWM signal of 25 kHz so that the temperature is controlled at the optimal level. Moreover, in the cathode side, the air is supplied with an air fan. With the air fan, sufficient quantity of air is guaranteed in normal operation. In other words, the fuel cells always work in the high stoichiometry mode. The pressure in the cathode side is kept equal to the atmosphere pressure. On the anode side, the pressure of hydrogen is fixed, and a purge is performed every 30 s. The fuel cells are self-humidified. Some critical parameters of the studied fuel cell stack module are listed in Table 1.

The dynamic load profile is obtained in real operating conditions of a hydrogen bike, which is supplied by a 36 V battery, while the fuel cell is used as a range extender, connected in parallel with the battery. Both are used to supply the bike with an average power demand of 53.6 W. A 2.5-hour operation profile is shown in Fig. 2, in which the fuel cell starts up to charge the battery until the battery's state-of-charge (SOC) gets to a pre-defined threshold and shuts down when the battery is fully charged. Based on this profile, the current load profile for the long-term PEM fuel cell degradation experiment is reproduced to reach 1500 h of operation time. The stack voltage and the current are recorded with a sampling frequency of 5 Hz and the characterization of the stack is performed every week by collecting polarization curves.

The measured stack voltage is shown in Fig. 3. Some details of the stack voltage and the corresponding current profile are plotted in Figs. 4(a) and 4(b), respectively. Some unintentional stops happen during the experiment due to test bench incidents. As the degradation of the fuel cell is on a longer time scale, i.e., thousands of hours, the stops have little influence on its long-term performance loss.

<sup>1</sup> FCLAB Research Federation: <http://www.fclab.fr/>.



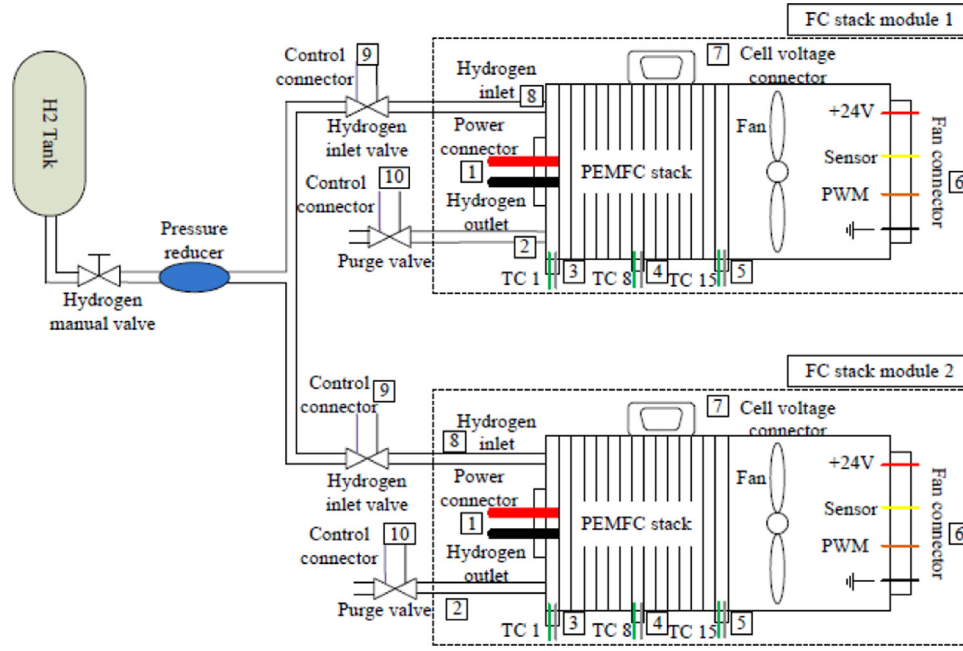


Fig. 1. Two-fuel-cell-module structure.

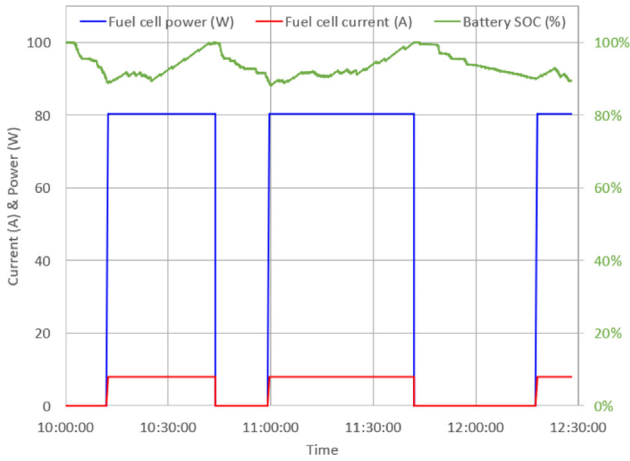


Fig. 2. Test profile of a hydrogen bike.

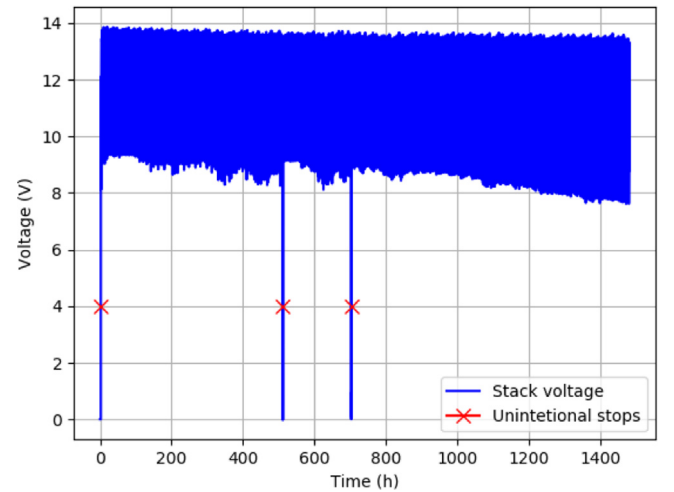


Fig. 3. Stack voltage evolution in the dynamic operating test.

### 3. Degradation identification

The performance loss process of the PEM fuel cell stack shown in Fig. 3 may be due to different causes, e.g., varying thermal and humidity state, fuel starvation, cycling with large voltage dynamics, etc. It is hard to represent its performance loss by the stack voltage evolution as it is also dependent on the load characteristics and system dynamics. Confronted with this problem, a degradation indicator is proposed in this section to evaluate the degradation of the PEM fuel cell operating under such dynamic load.

#### 3.1. Fuel cell polarization model

The polarization test is a common method to characterize a fuel cell. Polarization curve displays the stack voltage output  $V_{fc}$  against its operating current  $i$ . The polarization curve model of a  $n$ -cell fuel cell can be built as the reversible cell voltage  $V_0$  subtracting several irreversible losses including the activation losses and the crossover

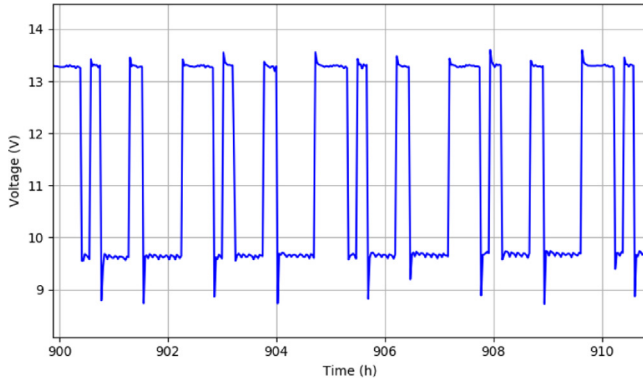
losses  $V_{act+cross}$ , the ohmic losses  $V_{ohmic}$ , the concentration losses  $V_{conc}$ :

$$V_{fc} = nV_{cell} = n(V_0 - V_{act+cross} - V_{ohmic} - V_{conc}) \quad (1)$$

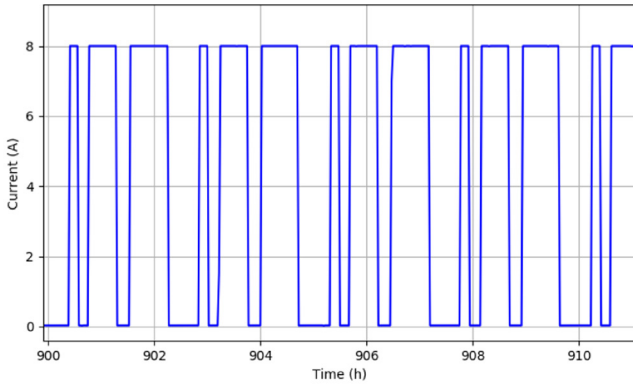
A detailed parametric model of  $V_{cell}$  is derived in Sharaf and Orhan (2014) and Jouin, Gouriveau, et al. (2016):

$$V_{cell}(i) = V_0 - \frac{RT}{2aF} \ln \left( \frac{i_{loss} + i}{i_0} \right) - iR_{eq} - B_c \ln \left( 1 - \frac{i}{i_L} \right) \quad (2)$$

where  $R$  is the gas constant,  $T$  is the operating temperature,  $F$  is the Faraday constant,  $a$  is charge transfer coefficients of the electrodes,  $i_{loss}$  is the stack internal current, which is assumed to be assimilated to the hydrogen crossover current alone and there is no current caused by membrane shorting,  $i_0$  is the exchange current at the electrodes,  $R_{eq}$  is the equivalent ohmic resistance,  $B_c$  is an empirical parameter considering the water and gas accumulation effects and  $i_L$  is the limiting current at the cathode (Jouin, Gouriveau, et al., 2016).

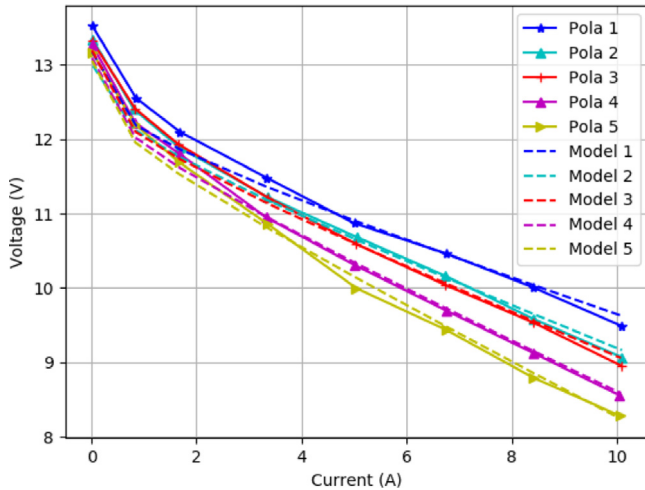


(a) Details of the stack voltage evolution



(b) Details of the current profile

Fig. 4. Details of the stack voltage and the corresponding current profile.

Fig. 5. Polarization curves fitted with different  $\alpha$  values.

### 3.2. Degradation description

To find an adequate degradation indicator for the PEM fuel cell operating under dynamic current, it is important to know that which component degradation will cause which parameter varies in (2). Some parameters, like  $R$  and  $F$ , are constant.  $T$  is controlled in the experiment so that it is also regarded as constant, so as  $V_0$ . Some parameters are difficult to know whether they vary with time or not, therefore,

they are set to fit the model with the measurements, namely  $a$  and  $B_c$ .  $i_{loss}$  is not considered as it is assumed to be assimilated to the hydrogen crossover current. Thus, the variations of the left three parameters,  $R_{eq}$ ,  $i_0$  and  $i_L$ , should be considered as the source of degradation.

$R_{eq}$ : The resistance increase can be caused by various phenomena. It includes the electronic and contact resistance increase, as well as the ionic resistance increase related to the membrane degradation (Jouin, Gouriveau, et al., 2016). The increase of the electronic and contact resistance can be observed at the surface layer of the bipolar plates, the electrode/electrolyte interface, etc, while the increase of the ionic resistance is dominant by the electrolyte materials and influenced by the membrane water concentration and temperature (Husar, Strahl, & Riera, 2012).

$i_0$ : The effective exchange current is a function of the electrode catalyst loading and the catalyst specific surface area (Barbir, 2013). For the fuel cell operated under dynamic load, the cycling will lead to the major degradation of the electrodes: the catalyst layer degradation and the carbon support degradation, especially, the catalyst loss is aggravated by the potential cycles (Khan, et al., 2021).

$i_L$ : The limiting current on the cathode varies due to the changes on the diffusivity of oxygen, the gas pressure and the thickness of the gas diffusion layer (Morgan & Datta, 2014). The diffusivity and the pressure of the oxygen at the cathode are dominated cause of the concentration loss, which are influenced by the gas and water accumulation and can be recovered or mitigated by proper water management. The thickness of the gas diffusion layer cannot change over some nano-metres, therefore, it can be ignored (Jouin, Gouriveau, et al., 2016).

Some works have modelled the variation of the three parameters using physical models or semi-empirical models, however, some of them are developed with assumptions, which have not been validated (Jouin, Gouriveau, et al., 2016). Moreover, complex parameters bring difficulties when performing prognostics and some measurements needed in the model are not economically or technically feasible, therefore, establishing a degradation indicator that can track the degradation of the PEM fuel cell is necessary.

### 3.3. Degradation indicator $\alpha$

Fig. 5 plots the polarization curves measured in the 2nd, 4th, 5th, 8th and 9th weeks, which indicates different degrees of fuel cell degradation. The polarization curves were obtained by varying the current value between 0 and the maximum (10 A). 8 current values, as shown in Fig. 5, were set increasingly to the test stack through an electronic load. For each test point, the current value was maintained for 10 min to get a stable voltage measurement. Then the polarization curves were formed by interconnecting the 8 test points in current-voltage coordinate plane.

The model of (2) is identified with different values of  $R_{eq}$ ,  $i_0$  and  $i_L$ , whereas the evolutions of the parameters are shown in Fig. 6. From Fig. 6, it is found that the equivalent resistance  $R_{eq}$  increases by approximately 80%, while the exchange current  $i_0$  decreases by a rather same value. The fitting result of  $i_L$  has remained nearly constant. It is due to that under the dynamic cycling load, the water accumulation is well managed and contributes rarely to the concentration loss. This observation inspires us to assume the same linear evolution of  $R_{eq}$  and  $i_0$  and assign a constant value to  $i_L$ . Therefore, a unique time-varying variable  $\alpha(t)$  is chosen to describe the deviation of the parameters, which reflects the state of health of the fuel cell:

$$R_{eq} = R_{eq,init} \cdot (1 + \alpha(t)) \quad (3)$$

$$i_0 = i_{0,init} \cdot (1 - \alpha(t)) \quad (4)$$

The introduction of variable  $\alpha(t)$  ensures the identification of the fuel cell degradation level in the dynamic operation of the fuel cell. Even if the stack is operated under random load and the degradation cannot be directly identified by the voltage signal,  $\alpha(t)$  can be used as a degradation indicator to indicate the health state of the fuel cell.

As degradation can only be observed over long periods of at least several hundred hours, the fuel cell degradation is supposed to be quasi-constant on a short time scale, i.e., several hours (Bressel et al., 2016; Jouin, Bressel, et al., 2016). It allows us to segment the operation time into short periods and fits the model with different  $\alpha$  values on each segment. This is realized by wrapping the pre-defined function as a model, which contains several parameters and an independent variable  $\alpha$ , and fitting it using the Levenberg–Marquardt algorithm (Moré, 1978). The pseudo-code is shown in Algorithm 1.

**Algorithm 1** Identification of the degradation indicator  $\alpha$

```

Load available measurement data of  $I, V$                                 ▷ Load data
Initialize the parameters in model (2)                                ▷ Initialization
Define:
Interval =  $l$ 
Number of steps =  $j$ 
Time step  $i = 0$ 
for  $i = 0, \dots, j$  do,
    Define model (2) with (3) and (4)                                ▷ Model definition
    Input  $X = I[0 + i * l : l + i * l]$                                 ▷ Segmentation
    Output  $Y = V[0 + i * l : l + i * l]$ 
    Fit the model with  $\alpha$  and find the best fit                        ▷ Model fit
end for

```

The identification result is shown in Fig. 7 and the details are in Fig. 8, in which the voltage measurement is segmented with an interval of 3 h. It can be noticed that the voltage dynamics in load transition periods are not well established using the identified degradation indicator and the polarization curve model. In fact, the voltage dynamics in transition states are mainly caused by system dynamics, such as thermal dynamics, which is not considered in the polarization curve model. The evolution of the extracted  $\alpha$  is shown in Fig. 9, in which some recoveries in the signal are observed. These recoveries are reversible degradation phenomena due to the characterizations, which are of different operating conditions that affect the gas and water diffusion within the cells are affected. However, these reversible phenomena are part of transient regimes and will disappear once the stack comes back to a permanent regime. As the implementation of prognostics relies on the degradation information contained in the signal, the extracted  $\alpha$  is smoothed using a Savitzky–Golay filter to avoid the influence of disturbing information.

#### 4. ESN-based prognostics method

A data-driven prognostics method based on neural network modelling is proposed in this section. The idea is to use the available dataset to build the system behaviour model and to project the current system state to the future. Data-driven prognostics methods have the model-free advantage that can be applied regardless of the physical characteristics of the system. In this section, a typical recurrent neural network (RNN), i.e., the ESN, is adapted for the prognostics purpose.

##### 4.1. Principle of ESN

The ESN has seen its wide use in time-series prediction applications (Jaeger, 2001). Different from traditional RNNs, the ESN uses a “reservoir pool” to build the structure of nonlinear systems, which achieves high prediction speed and competitive prediction performance. The implementation of the ESN is shown in Fig. 10 and explained in what follows.

The state update model of ESN is written as:

$$\tilde{\mathbf{u}}(t) = f(\mathbf{w}_{res} \mathbf{u}(t-1) + \mathbf{w}_{in} \mathbf{x}(t)) \quad (5)$$

$$\mathbf{u}(t) = (1 - k)\mathbf{u}(t-1) + k\tilde{\mathbf{u}}(t) \quad (6)$$

$$\mathbf{y}(t) = g(\mathbf{w}_{out} \mathbf{u}(t)) \quad (7)$$

where  $\mathbf{x}(t) \in \mathbb{R}^{N_x}$  and  $\mathbf{y}(t) \in \mathbb{R}^{N_y}$  are the input and output, which, in this study, are the sequences of the degradation indicator  $\alpha$ ,  $\mathbf{u}(t) \in \mathbb{R}^{N_u}$  is the internal state in the reservoir and  $\tilde{\mathbf{u}}(t) \in \mathbb{R}^{N_u}$  is its update,  $\tilde{\mathbf{u}}(t) = \mathbf{u}(t) - \mathbf{u}(t-1)$ ,  $\mathbf{w}_{in} \in \mathbb{R}^{N_u \times (1+N_x)}$  is the input weight matrix,  $\mathbf{w}_{res} \in \mathbb{R}^{N_u \times N_u}$  is the recurrent weight matrix in the reservoir, and  $\mathbf{w}_{out} \in \mathbb{R}^{N_y \times (1+N_x+N_u)}$  is the output weight matrix.  $k$  is the leaking rate with a range of (0, 1]. The  $\tanh$  function is generally adopted as the activation function  $f(\bullet)$  of the reservoir, and  $g(\bullet)$  of the output layer could be defined with a simple linear function such as  $g(\bullet) = 1$ .  $\mathbf{w}_{in}$  and  $\mathbf{w}_{res}$  are initialized randomly and they are constant so that there is no need to train them. Only  $\mathbf{w}_{out}$  is going to be trained by linear regression. When the training dataset is provided, denoted as  $\mathbf{X}_t = [\mathbf{x}(1), \dots, \mathbf{x}(N_t)]$  and  $\mathbf{Y}_t = [\mathbf{y}(1), \dots, \mathbf{y}(N_t)]$ , where  $N_t$  is the number of sequences in the input and the output, the corresponding reservoir states,  $\mathbf{U}_t = [\mathbf{u}(1), \dots, \mathbf{u}(N_t)]$  can be calculated according to (5) and (6). The output weight matrix is calculated as:

$$\mathbf{w}_{out} = (\Psi_t^T \Psi_t + \lambda \mathbf{I})^{-1} \Psi_t^T \mathbf{Y}_t \quad (8)$$

where  $\mathbf{I}$  is  $N_u$  order unit matrix,  $\lambda$  is the regulation parameter and

$$\Psi = [1; \mathbf{X}_t; \mathbf{U}_t] = \begin{bmatrix} 1 & 1 & \dots & 1 \\ \mathbf{x}(1) & \mathbf{x}(2) & \dots & \mathbf{x}(N_t) \\ \mathbf{u}(1) & \mathbf{u}(2) & \dots & \mathbf{u}(N_t) \end{bmatrix} \quad (9)$$

The general working procedure is as following:

1. Choose the size of the reservoir  $N_u$  and other parameters concerning the level of sparsity of connection, as well as the leakage;
2. Generate the input weights  $\mathbf{w}_{in}$  by sampling from a random binomial distribution;
3. Generate the reservoir weights  $\mathbf{w}_{res}$  by sampling from a uniform distribution;
4. Calculate the update of the state in the reservoir as the activation function  $f(\bullet)$  of the input at the current time step multiplied by the weights plus the previous state multiplied by the reservoir weights, as written in (5);
5. Create input sequences and connect them to the desired outputs using linear regression and obtain the trained ESN.

Based on the procedure of training an ESN, an input window and a prediction window need to be defined, which are used to formulate the input sequences and the output sequences of the ESN, respectively. The input window length is the length of the input sequence and the prediction window length is how many steps are going to be predicted following the input sequence. The input window length and the prediction window length are selected according to the volume of available input data. Supposing the number of available measurements  $s$  is up to  $N$ , a window length of  $p$  is used for the input sequence, written as:

$$\mathbf{x}(i) = [s(i+1), s(i+2), \dots, s(i+p)], \quad i = 0, \dots, N-p \quad (10)$$

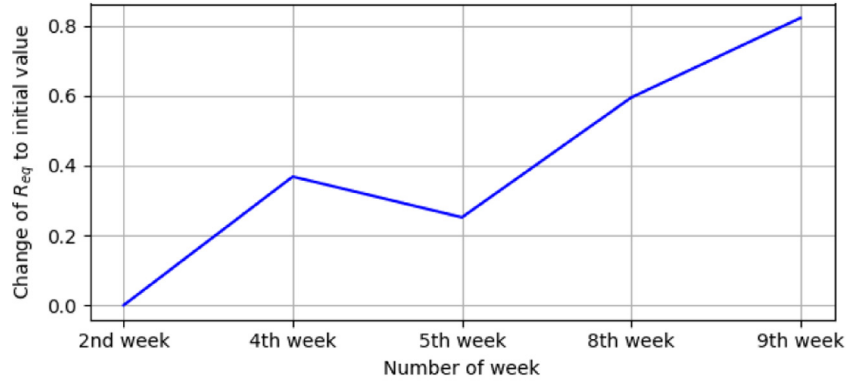
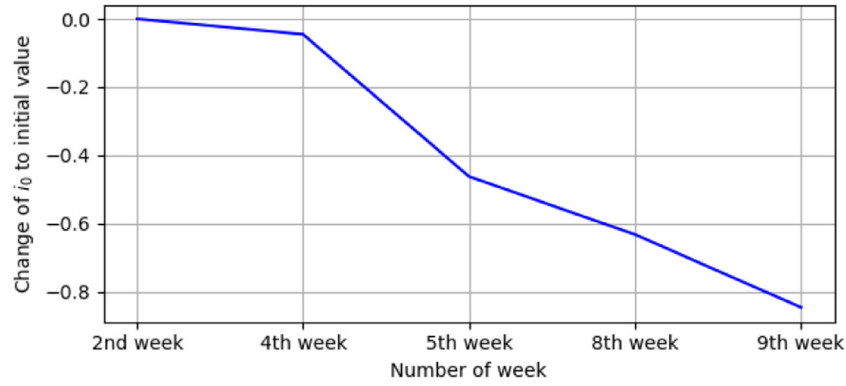
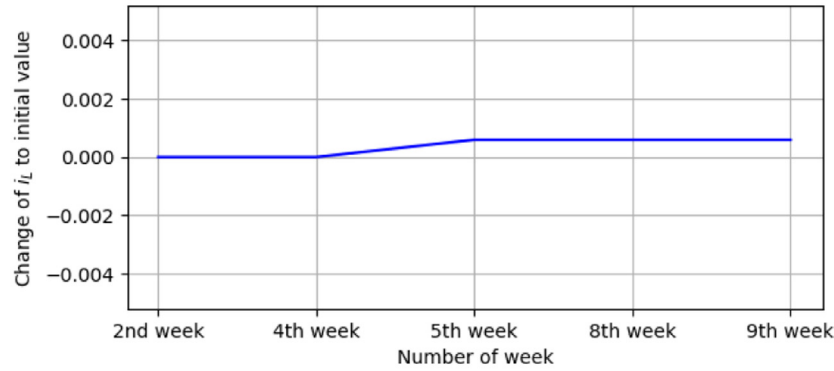
For simplicity, it is written  $\mathbf{x}(i) = [s(i+1) : s(i+p)]$  in the following text. Then, the corresponding output with a prediction window length of  $q$  is written as:

$$\mathbf{y}(i) = [\hat{s}(i+p+1), \hat{s}(i+p+2), \dots, \hat{s}(i+p+q)], \quad i = 0, \dots, N-p \quad (11)$$

Similarly, it is written with the form of  $\mathbf{y}(i) = [\hat{s}(i+p+1) : \hat{s}(i+p+q)]$  in the following text.

##### 4.2. Adapt ESN for prognostics purpose

The prognostics process can be summarized as a process of estimating a system's remaining useful life and the uncertainties. The international organization for standardization (ISO) committee has defined prognostics as (ISO13381-1, 2004):

(a) Change of  $R_{eq}$  to its initial value(b) Change of  $i_0$  to its initial value(c) Change of  $i_L$  to its initial valueFig. 6. Evolution of degradation parameters  $R_{eq}$ ,  $i_0$  and  $i_L$ .

Standard ISO 13381 (2004). *The aim of prognostics is the “estimation of time to failure and risk for one or more existing and future failure modes”.*

Therefore, to perform prognostics, we need to predict the system performance until the system failure. Based on the time series forecasting process described in Section 4.1, the last  $p$ -length sequence in the training phase is used to predict a sequence with the length of  $q$ . Then, the prognostics starts, in which we cannot predict the subsequent states because the input sequences run out, the prediction cannot continue. As we need to continue to predict the time series until the end of life of the system, new input sequences should be formulated to successively move

the input window. Thus, to retain the degradation tendency and to manage the prediction uncertainty, the predicted values of the last step with a sliding window of length  $m$  are reinjected to the input sequence of the next step, as shown in Fig. 11. Therefore, the last  $m$  values of the input sequence are indeed the predicted values. This process allows the continuous formulation of the input even without measurements so that the prognostics can be realized. This process is repeated until reaching the end-of-life (EOL) threshold, which, in this paper, is supposed to be the value of 0.423, 97% of the maximum degradation of the tested fuel cell regarding the length of the experiment.

The pseudo-code of implementing ESN adapted for prognostics purpose is shown as Algorithm 2, where  $N_{train}$  is the number of training



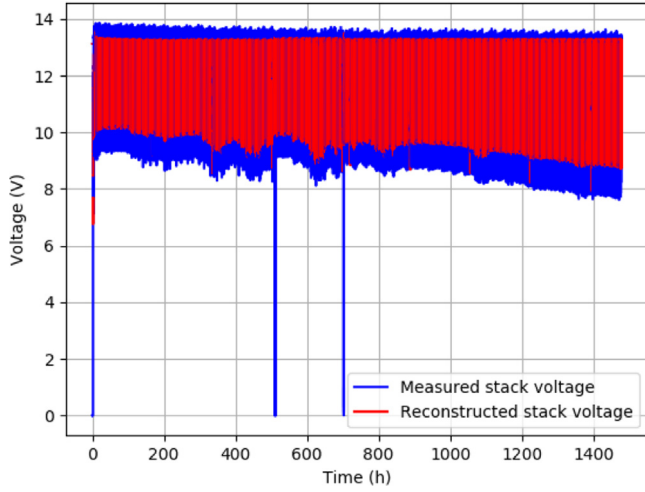


Fig. 7. Reconstructed and measured stack voltages.

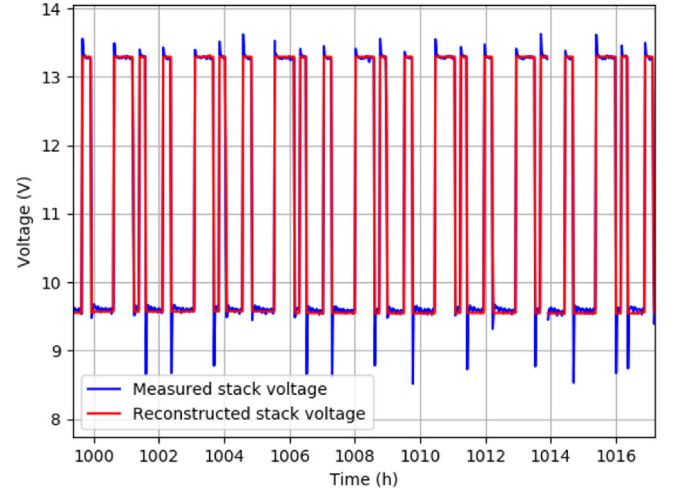


Fig. 8. Details of the reconstructed and the measured stack voltages.

steps equal to  $N-p$  and  $N_{predict}$  is the prediction steps until the system's EOL.

---

**Algorithm 2** ESN for prognostics purpose
 

---

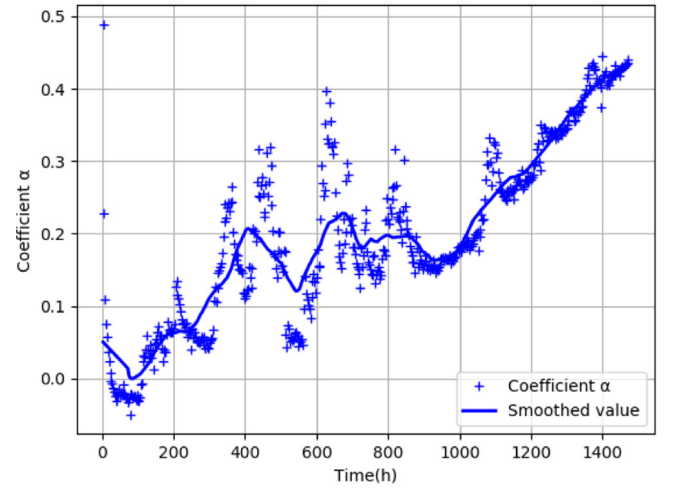
```

Load training dataset  $s$                                 ▷ Load data
Smooth the training data                                ▷ Smoothing
Normalize the training data                             ▷ Normalization
Define:
Input window length =  $p$ 
Prediction window length =  $q$ 
Sliding window length =  $m$ 
Number of training steps =  $N_{train}$ 
Number of prediction steps =  $N_{predict}$ 
Time step  $i = 0$ 
while  $x_i < x_{EOL}$  do
  for  $i = 0, \dots, N_{train}$  do                                ▷ Training phase
     $y_{train}[i, :] = s[i + p + 1 : i + p + q]$  ▷ Prepare input and output
     $x_{train}[i, :] = s[i : i + p]$ 
  end for
  Fit the ESN with prepared input  $x_{train}$  and output  $y_{train}$ 
  Initialize  $x_{predict}[0, :]$  by connecting  $x[N_{train} + m : N_{train} + p]$  and
   $y_{train}[-1, 0 : m]$ 
  for  $i = 0, \dots, N_{predict}$  do                                ▷ Start prognostics
    Predict  $y_{predict}[i]$  using the fitted ESN and  $x_{predict}[i, :]$ 
    Reformulate  $x_{predict}[i, :]$  by connecting  $x_{predict}[i - 1, m : p]$  and
     $y_{predict}[i, 0 : m]$                                 ▷ Reformulate input
  end for
end while
  
```

---

#### 4.3. Implementation of ESN-based prognostics

In order to optimize the configuration of the ESN, the proposed ESN-based prognostics method consists of three phases: training phase, evaluation phase and prediction phase. The length of the identified degradation indicator  $\alpha$ , shown in Fig. 9, is also divided into three parts for the use of each phase. The ESN is trained in the training phase using the prepared input and output sequences and then, the following 400 h are regarded as the evaluation phase. During the evaluation phase, the measurement is supposed to be unavailable so that the output sequence is reformulated by the predicted values of the last step. The trained ESN model is used to output the predictions of  $\alpha$  and the real values of  $\alpha$  is used to evaluate the performance of the prognostics. Here, the result of prognostics is evaluated by calculating the root mean square

Fig. 9. Evolution of the dynamic degradation indicator  $\alpha$ .

error (RMSE), written as (12). In order to find the optimal settings of the ESN, an optimization method, i.e., the genetic algorithm (GA), is applied to generate different parameter combinations and run the prognostics algorithm repeatedly until find the optimal settings. The idea is to code the unknown parameters into binary digits, known as a chromosome, then, calculate the RMSE on the evaluation phase by selecting, crossover and mutating the chromosomes repeatedly until finding the optimal solution (Chipperfield, Fleming, & M. Fonseca, 1994). The advantage of GA is its ability to locate the global optimum or near-global optimum solution without exhausting search of the solution space. Besides, the processing time only increased as the square of the project size and not exponentially. Some configured parameters of the proposed ESN-based prognostics method and the adopted GA are listed in Table 2, where the length of the sliding window of  $m$  and the number of reservoir neurons  $N$  are optimized by the GA. The influence of other ESN parameters in prognostics results is not so critical and the configuration method in Lukoševičius (2012) has been adopted.

$$RMSE = \sqrt{\frac{\sum_{k=1}^n (x_k - \hat{x}_k)^2}{n}} \quad (12)$$

Finally, in the prediction phase, no measurement is available while the ESN has already been optimized and validated by the evaluation phase, therefore, the data of both the training phase and the evaluation phase are entered into the trained ESN model and output the prediction

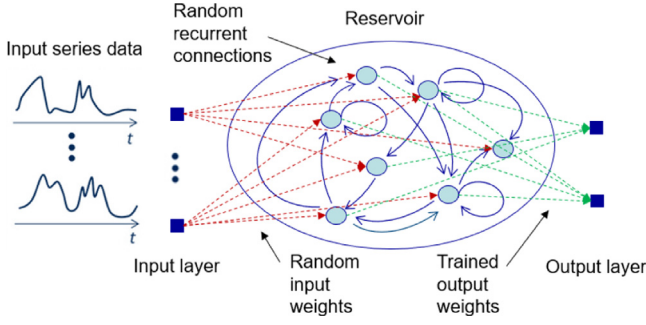


Fig. 10. ESN structure illustration.

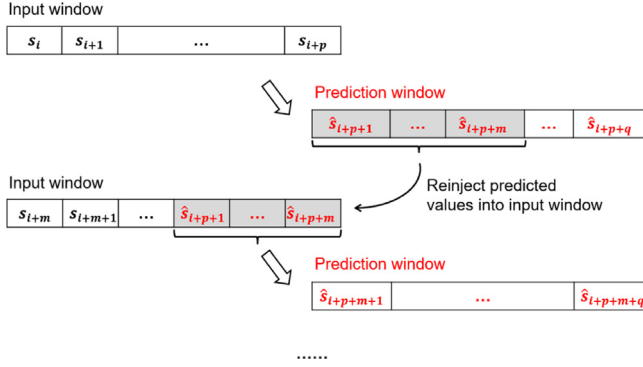


Fig. 11. ESN adapted for prognostics purpose.

**Table 2**  
Configuration of ESN-based prognostics method.

Parameter	Value
Input window length $p$	50
Prediction window length $q$	10
Leaking rate	0.2
Spectral radius	0.6
Regression parameter	0.01
GA population size	100
Number of generations	400
Length of chromosome	10

results. The whole procedure is shown in Fig. 12. The prognostics results are discussed in the following section.

#### 4.4. Result discussion

For comparison, at first,  $m$  is fixed at 1. The optimal  $N$  is found between 10 and 400 using an iterating loop. The optimal values of  $N$ , the RMSEs of the prognostics results in both evaluation and prediction phases and the implementation time with different training data lengths are recorded in Table 3. The prognostics performance on the evaluation phase and the prediction phase, as well as the errors are shown in Fig. 13 for a visual check. The beginning of the training phase has lower accuracy because of the insufficient training data. After 200 h, the training error is closed to zero, which demonstrates that the configure ESN is of good performance. During the evaluation phase, the measurement is supposed to be unavailable so that the output sequence is reformulated by the predicted values of the last step, as described in Section 4.2. The optimal result is plotted in red dashed line. However, when it comes to the prediction phase, the RMSEs get worse. This is because there is only one predicted value being considered in the next step, which could be accidental and cannot transfer enough information. Moreover, the implementation time of GA is less than 1 min, while the implementation time of ESN-based prognostics is less than 1 s.

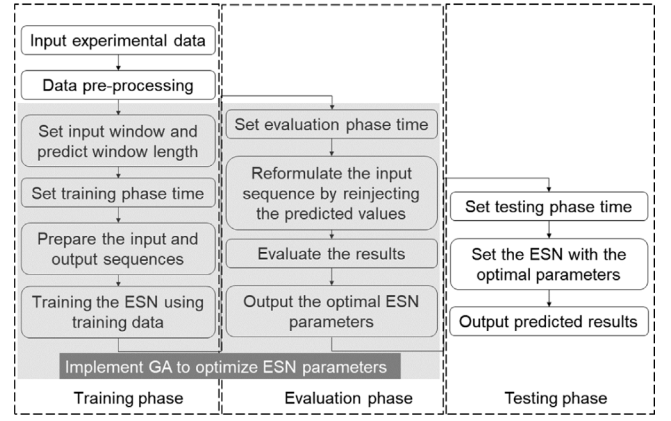


Fig. 12. Procedure of ESN-based prognostics method.

**Table 3**  
ESN-based prognostics results ( $m=1$ ).

Training data length (hours)	500	600	700	800
$m$	1	1	1	1
$N$	90	94	83	81
RMSE of training	0.036	0.019	0.012	0.017
RMSE of evaluation	0.030	0.032	0.056	0.039
RMSE of prediction	0.112	0.140	0.304	0.182
Prognostics implementation time	0.93s	0.94s	0.93s	0.94s

**Table 4**  
GA optimization and ESN-based prognostics results (optimizing  $m$ ).

Training data length (hours)	500	600	700	800
Optimized $m$	3	5	3	3
Optimized $N$	95	80	234	265
RMSE of training	0.017	0.019	0.019	0.005
RMSE of evaluation	0.031	0.039	0.047	0.033
Improvements of evaluation	-3.3%	2.5%	16.1%	1.5%
RMSE of prediction	0.051	0.017	0.028	0.020
Improvements of prediction	54.5%	87.9%	90.8%	89.0%
Prognostics implementation time	0.91s	0.90s	1.12s	1.03s

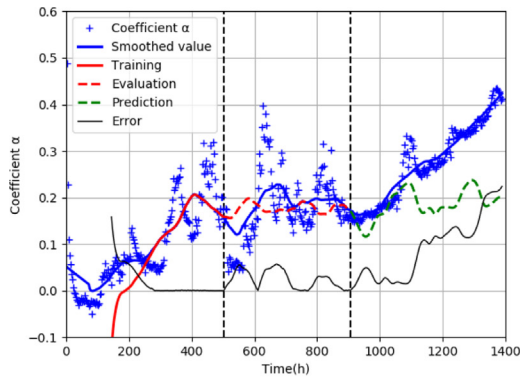
**Table 5**  
Model parameters of particle filter prognostics method.

Parameter	Value
Input dimension	1
Output dimension	1
Number of state variables	7
Number of particles	2000

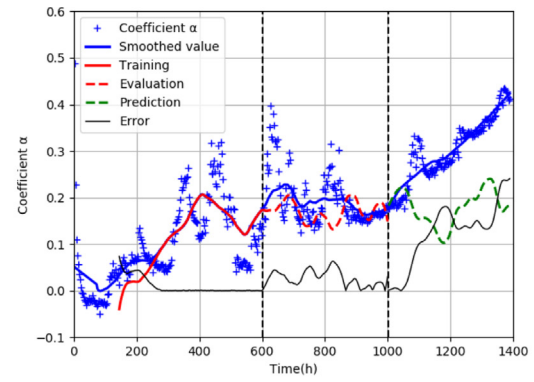
Fig. 14 shows the prognostics results with different training data lengths, in which both  $m$  and  $N$  are optimized. The GA optimization results of the two parameters and the RMSEs of both the evaluation phase and the prediction phase, together with the improvements compared with Table 3 are shown in Table 4. By optimizing the number of values that are reinjected into the input sequence of the next step, prognostics results in the prediction phase have been improved up to 90.8%.

#### 4.5. Comparison with different methods

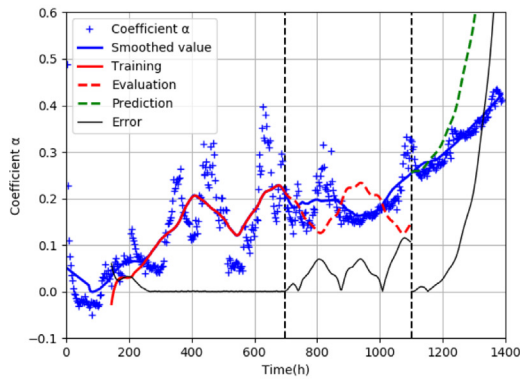
The proposed prognostics method is compared with different methods in the literature. The comparison methods include particle filter (Jouin et al., 2014) and stacked long short-term memory (LSTM) (Wang, Cheng, & Hsiao, 2020). The training phase considers the same generated samples. In the compared particle filter method, a second order exponential model is used, and the details of model parameters of particle filter prognostics method is listed in Table 5. The stacked LSTM



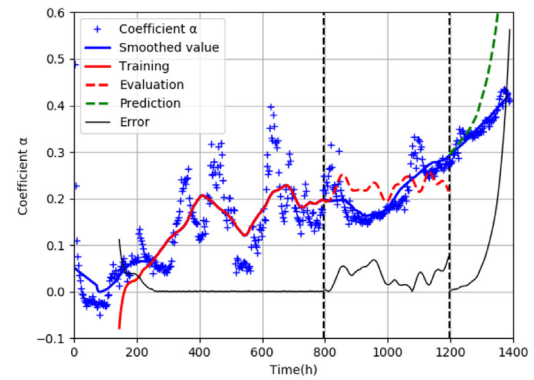
(a) Prediction result with training data length = 500 hours



(b) Prediction result with training data length = 600 hours



(c) Prediction result with training data length = 700 hours



(d) Prediction result with training data length = 800 hours

Fig. 13. Implementation of prognostics with different training data lengths (optimizing  $N$ ). (For interpretation of the references to colour in this figure legend, the reader is referred to the web version of this article.)

Table 6

Model parameters of stacked LSTM prognostics method.

Parameter	Value
Time steps	4
Number of neurons on hidden layer 1	100
Number of neurons on hidden layer 2	100
Number of neurons on dense layer	1
Optimizer	adam
Loss	mean squared error
Epoch number	50
Batch size	50
Dropout rate	0.01

used for comparison is with two hidden layers and a dense (output) layer for prediction. The details of the configuration of the stacked LSTM prognostics method is shown in Table 6.

The performance of the three different prognostics method is compared in Table 7. As it can be seen from Table 7, the proposed multi-step ESN-based prognostics method has achieved the best prediction accuracy at 600-hour, 700-hour and 800-hour training data length, while the accuracy is worse than the particle filter method at 500-hour training data length. This is because when more information is fed to the model, the model can leverage more trend information, thus improving the prediction accuracy. Besides, the performance of stacked LSTM prognostics method is the worst due to the non-optimized configurations. When comparing the implementation time, the proposed ESN runs the fastest, which is more competitive for online applications.

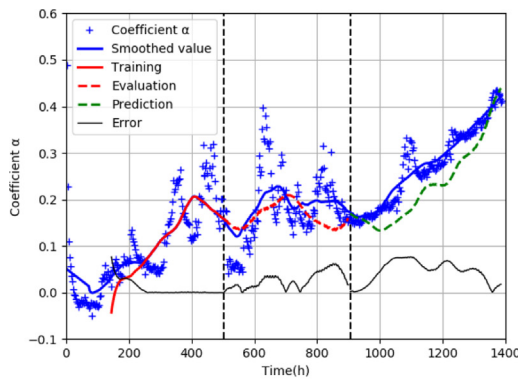
## 5. Conclusion

A degradation identification and prognostics method for real-time operating PEM fuel cells was proposed in this paper. The degradation indicator was derived based on the polarization model and could be extracted from the stack voltage measurements with random system dynamics. To perform prognostics, an enhanced multi-step ESN was adapted for the prediction purpose and the parameters of the ESN were optimized through an evaluation phase by a genetic algorithm. Compared to non-optimized case, the RMSEs of the predictions were improved up to 90.8% by introducing an optimized sliding window length when reformulating the input of the ESN in the prognostics phase. Moreover, the proposed method achieved better accuracy and less computation time when comparing with other prognostics methods.

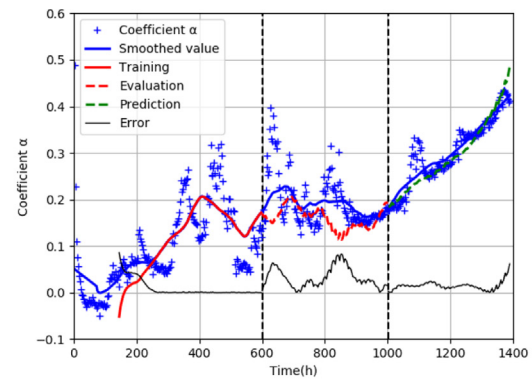
The proposed method of degradation identification and prognostics allows one to estimate and predict the PEM fuel cell health state under variable and dynamic operating conditions. The degradation identification can be realized in real time without using supplementary measurements and the prognostics strategy is model-free. This method is control-oriented and can facilitate the development of degradation tolerant control strategies as well as advanced predictive maintenance solutions. The ongoing work is also being conducted to investigate systematically the effect of different factors in dynamic operating conditions, such as the internal water dynamics.

## Declaration of competing interest

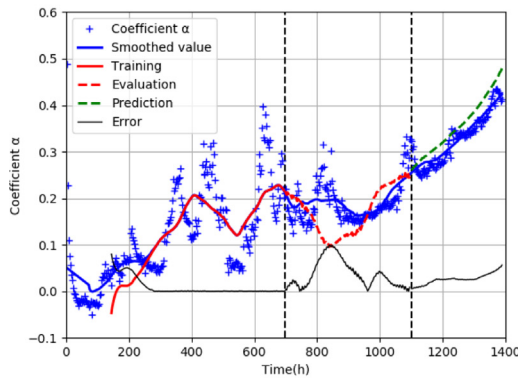
The authors declare that they have no known competing financial interests or personal relationships that could have appeared to influence the work reported in this paper.



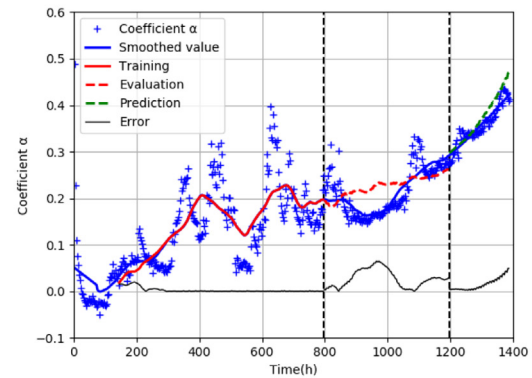
(a) Prediction result with training data length = 500 hours



(b) Prediction result with training data length = 600 hours



(c) Prediction result with training data length = 700 hours



(d) Prediction result with training data length = 800 hours

Fig. 14. Implementation of prognostics with different training data lengths (optimizing  $m$  and  $N$ ).Table 7  
Comparison of prognostics methods.

Training data length (hour)	500		600		700		800	
	RMSE	Time	RMSE	Time	RMSE	Time	RMSE	Time
Partile filter (Jouin et al., 2014)	0.042	4.19 s	0.035	4.45 s	0.049	4.73 s	0.047	5.25 s
Stacked LSTM (Wang et al., 2020)	0.079	6.81 s	0.078	7.31 s	0.078	7.11 s	0.051	7.47 s
Proposed ESN	0.051	0.91 s	0.017	0.90 s	0.028	1.12 s	0.020	1.03 s

## Acknowledgements

This paper is supported by the project HAEOLUS, funded by the Fuel Cells and Hydrogen 2 Joint Undertaking under the European Union's Horizon 2020 research and innovation program under grant agreement No 779469. Any contents herein reflect solely the authors' view. The FCH 2 JU and the European Commission are not responsible for any use that may be made of the information herein contained. This work is also supported by the EIPHI Graduate School (contract ANR-17-EURE-0002) and the project PRODIG (1494C0045) funded by French Environment and Energy Management Agency.

## References

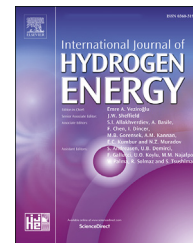
- Barbir, F. (2013). Chapter five - fuel cell operating conditions. In F. Barbir (Ed.), *PEM fuel cells* (2nd ed.). (pp. 119–157). Boston: Academic Press, <http://dx.doi.org/10.1016/B978-0-12-387710-9.00005-9>.
- Bressel, M., Hilaret, M., Hissel, D., & Ould Bouamama, B. (2016). Remaining useful life prediction and uncertainty quantification of proton exchange membrane fuel cell under variable load. *IEEE Transactions on Industrial Electronics*, 63(4), 2569–2577. <http://dx.doi.org/10.1109/TIE.2016.2519328>.
- Chipperfield, A., Fleming, P., & M. Fonseca, C. (1994). Genetic algorithm tools for control systems engineering. *Proceedings of Adaptive Computing in Engineering Design and Control*, 23, [http://dx.doi.org/10.1016/S1474-6670\(17\)49015-X](http://dx.doi.org/10.1016/S1474-6670(17)49015-X).
- Han, J., Han, J., & Yu, S. (2020). Experimental analysis of performance degradation of 3-cell PEMFC stack under dynamic load cycle. *International Journal of Hydrocarbon Engineering*, 45(23), 13045–13054. <http://dx.doi.org/10.1016/j.ijhydene.2020.02.215>.
- Hua, Z., Zheng, Z., Péra, M. C., & Gao, F. (2020). Data-driven prognostics for PEMFC systems by different echo state network prediction structures. In *2020 IEEE transportation electrification conference expo* (pp. 495–500). <http://dx.doi.org/10.1109/ITEC48692.2020.9161581>.
- Hua, Z., Zheng, Z., Péra, M.-C., & Gao, F. (2020). Remaining useful life prediction of PEMFC systems based on the multi-input echo state network. *Applied Energy*, 265, Article 114791. <http://dx.doi.org/10.1016/j.apenergy.2020.114791>.
- Husar, A., Strahl, S., & Riera, J. (2012). Experimental characterization methodology for the identification of voltage losses of PEMFC: Applied to an open cathode stack. *International Journal of Hydrocarbon Engineering*, 37(8), 7309–7315. <http://dx.doi.org/10.1016/j.ijhydene.2011.11.130>, III Iberian Symposium on Hydrogen, Fuel Cells and Advanced Batteries, HYCELTEC-2011.
- ISO13381-1 (2004). Condition monitoring and diagnostics of machines e prognostics e Part1: general guidelines. *International Organization for Standardization*.
- Jaeger, H. (2001). The “echo state” approach to analysing and training recurrent neural networks: GMD Report 148, GMD - German National Research Institute for Computer Science.
- Jouin, M., Bressel, M., Morando, S., Gouriveau, R., Hissel, D., Péra, M.-C., et al. (2016). Estimating the end-of-life of PEM fuel cells: Guidelines and metrics. *Applied Energy*, 177, 87–97. <http://dx.doi.org/10.1016/j.apenergy.2016.05.076>.
- Jouin, M., Gouriveau, R., Hissel, D., Marion-Péra, M.-C., & Zerhouni, N. (2016). Degradations analysis and aging modeling for health assessment and prognostics of PEMFC. *Reliability Engineering & System Safety*, 148, 78–95. <http://dx.doi.org/10.1016/j.res.2015.12.003>.



- Jouin, M., Gouriveau, R., Hissel, D., Péra, M.-C., & Zerhouni, N. (2014). Prognostics of PEM fuel cell in a particle filtering framework. *International Journal of Hydrocarbon Engineering*, 39(1), 481–494. <http://dx.doi.org/10.1016/j.ijhydene.2013.10.054>.
- Keller, R., Ding, S., Müller, M., & Stolten, D. (2017). Fault-tolerant model predictive control of a direct methanol-fuel cell system with actuator faults. *Control Engineering Practice*, 66, 99–115. <http://dx.doi.org/10.1016/j.conengprac.2017.06.008>.
- Khan, S. S., Shareef, H., Kandideyeni, M., Boulon, L., Amine, A., & Abdennebi, E. H. (2021). Dynamic semiempirical PEMFC model for prognostics and fault diagnosis. *IEEE Access*, 9, 10217–10227. <http://dx.doi.org/10.1109/ACCESS.2021.3049528>.
- Kong, S., Bressel, M., Hilairat, M., & Roche, R. (2020). Advanced passivity-based, aging-tolerant control for a fuel cell/super-capacitor hybrid system. *Control Engineering Practice*, 105, Article 104636. <http://dx.doi.org/10.1016/j.conengprac.2020.104636>.
- Kurtz, J. M., & Dinh, H. N. (2018). *Fuel cell technology status: Degradation: Tech. rep., National Renewable Energy Lab.(NREL), Golden, CO (United States)*.
- Li, Z., Jemei, S., Gouriveau, R., Hissel, D., & Zerhouni, N. (2016). Remaining useful life estimation for PEMFC in dynamic operating conditions. In *2016 IEEE vehicle power and propulsion conference* (pp. 1–6). <http://dx.doi.org/10.1109/VPPC.2016.7791762>.
- Li, Z., Zheng, Z., & Outbib, R. (2020). Adaptive prognostic of fuel cells by implementing ensemble echo state networks in time-varying model space. *IEEE Transactions on Industrial Electronics*, 67(1), 379–389. <http://dx.doi.org/10.1109/TIE.2019.2893827>.
- Liu, H., Chen, J., Hissel, D., Lu, J., Hou, M., & Shao, Z. (2020). Prognostics methods and degradation indexes of proton exchange membrane fuel cells: A review. *Renewable and Sustainable Energy Reviews*, 123, Article 109721. <http://dx.doi.org/10.1016/j.rser.2020.109721>.
- Liu, H., Chen, J., Hissel, D., & Su, H. (2019). Short-term prognostics of PEM fuel cells: A comparative and improvement study. *IEEE Transactions on Industrial Electronics*, 66(8), 6077–6086. <http://dx.doi.org/10.1109/TIE.2018.2873105>.
- Liu, H., Chen, J., Zhu, C., Su, H., & Hou, M. (2017). Prognostics of proton exchange membrane fuel cells using a model-based method. *IFAC-PapersOnLine*, 50(1), 4757–4762. <http://dx.doi.org/10.1016/j.ifacol.2017.08.947>, 20th IFAC World Congress.
- Lukoševičius, M. (2012). A practical guide to applying echo state networks. In G. Montavon, G. B. Orr, & K.-R. Müller (Eds.), *Neural networks: Tricks of the trade: second edition* (pp. 659–686). Berlin, Heidelberg: Springer, [http://dx.doi.org/10.1007/978-3-642-35289-8\\_36](http://dx.doi.org/10.1007/978-3-642-35289-8_36).
- Luna, J., Usai, E., Husar, A., & Serra, M. (2017). Enhancing the efficiency and lifetime of a proton exchange membrane fuel cell using nonlinear model-predictive control with nonlinear observation. *IEEE Transactions on Industrial Electronics*, 64(8), 6649–6659. <http://dx.doi.org/10.1109/TIE.2017.2682787>.
- Ma, R., Li, Z., Breaz, E., Liu, C., Bai, H., Briois, P., et al. (2019). Data-fusion prognostics of proton exchange membrane fuel cell degradation. *IEEE Transactions on Industry Applications*, 55(4), 4321–4331. <http://dx.doi.org/10.1109/TIA.2019.2911846>.
- Ma, J., Liu, X., Zou, X., Yue, M., Shang, P., Kang, L., et al. (2020). Degradation prognosis for proton exchange membrane fuel cell based on hybrid transfer learning and intercell differences. *ISA Transactions*, <http://dx.doi.org/10.1016/j.isatra.2020.06.005>.
- Ma, R., Yang, T., Breaz, E., Li, Z., Briois, P., & Gao, F. (2018). Data-driven proton exchange membrane fuel cell degradation predication through deep learning method. *Applied Energy*, 231, 102–115. <http://dx.doi.org/10.1016/j.apenergy.2018.09.111>.
- Mezzi, R., Morando, S., Steiner, N. Y., Péra, M. C., Hissel, D., & Larger, L. (2018). Multi-reservoir echo state network for proton exchange membrane fuel cell remaining useful life prediction. In *IECON 2018 - 44th annual conference of the IEEE industrial electronics society* (pp. 1872–1877). <http://dx.doi.org/10.1109/IECON.2018.8591345>.
- Morando, S., Jemei, S., Gouriveau, R., Zerhouni, N., & Hissel, D. (2013). Fuel cells prognostics using echo state network. In *IECON 2013 - 39th annual conference of the IEEE industrial electronics society* (pp. 1632–1637). <http://dx.doi.org/10.1109/IECON.2013.6699377>.
- Morando, S., Jemei, S., Hissel, D., Gouriveau, R., & Zerhouni, N. (2017). Proton exchange membrane fuel cell ageing forecasting algorithm based on echo state network. *International Journal of Hydrocarbon Engineering*, 42(2), 1472–1480. <http://dx.doi.org/10.1016/j.ijhydene.2016.05.286>.
- Moré, J. J. (1978). The levenberg-marquardt algorithm: Implementation and theory. In G. A. Watson (Ed.), *Numerical analysis* (pp. 105–116). Berlin, Heidelberg: Springer.
- Morgan, J. M., & Datta, R. (2014). Understanding the gas diffusion layer in proton exchange membrane fuel cells. I. How its structural characteristics affect diffusion and performance. *Journal of Power Sources*, 251, 269–278. <http://dx.doi.org/10.1016/j.jpowsour.2013.09.090>.
- Pan, R., Yang, D., Wang, Y., & Chen, Z. (2020). Health degradation assessment of proton exchange membrane fuel cell based on an analytical equivalent circuit model. *Energy*, 207, Article 118185. <http://dx.doi.org/10.1016/j.energy.2020.118185>.
- Ren, P., Pei, P., Li, Y., Wu, Z., Chen, D., & Huang, S. (2020). Degradation mechanisms of proton exchange membrane fuel cell under typical automotive operating conditions. *Progress in Energy and Combustion Science*, 80, Article 100859. <http://dx.doi.org/10.1016/j.pecs.2020.100859>.
- Sharaf, O. Z., & Orhan, M. F. (2014). An overview of fuel cell technology: Fundamentals and applications. *Renewable and Sustainable Energy Reviews*, 32, 810–853. <http://dx.doi.org/10.1016/j.rser.2014.01.012>.
- Wang, F.-K., Cheng, X.-B., & Hsiao, K.-C. (2020). Stacked long short-term memory model for proton exchange membrane fuel cell systems degradation. *Journal of Power Sources*, 448, Article 227591. <http://dx.doi.org/10.1016/j.jpowsour.2019.227591>.
- Wang, G., Huang, F., Yu, Y., Wen, S., & Tu, Z. (2018). Degradation behavior of a proton exchange membrane fuel cell stack under dynamic cycles between idling and rated condition. *International Journal of Hydrocarbon Engineering*, 43(9), 4471–4481. <http://dx.doi.org/10.1016/j.ijhydene.2018.01.020>.
- Wu, Y., Breaz, E., Gao, F., Paire, D., & Miraoui, A. (2016). Nonlinear performance degradation prediction of proton exchange membrane fuel cells using relevance vector machine. *IEEE Transactions on Energy Conversion*, 31(4), 1570–1582. <http://dx.doi.org/10.1109/TEC.2016.2582531>.
- Zhou, D., Al-Durra, A., Zhang, K., Ravey, A., & Gao, F. (2019). A robust prognostic indicator for renewable energy technologies: A novel error correction grey prediction model. *IEEE Transactions on Industrial Electronics*, 66(12), 9312–9325. <http://dx.doi.org/10.1109/TIE.2019.2893867>.

Available online at [www.sciencedirect.com](http://www.sciencedirect.com)

ScienceDirect

journal homepage: [www.elsevier.com/locate/he](http://www.elsevier.com/locate/he)

# Two-stage model predictive control for a hydrogen-based storage system paired to a wind farm towards green hydrogen production for fuel cell electric vehicles<sup>☆</sup>

Muhammad Bakr Abdelghany<sup>a,\*</sup>, Muhammad Faisal Shehzad<sup>b</sup>,  
Valerio Mariani<sup>a</sup>, Davide Liuzza<sup>c</sup>, Luigi Glielmo<sup>a</sup>

<sup>a</sup> Group for Research on Automatic Control Engineering, Department of Engineering, University of Sannio, Piazza Roma 21, 82100 Benevento, Italy

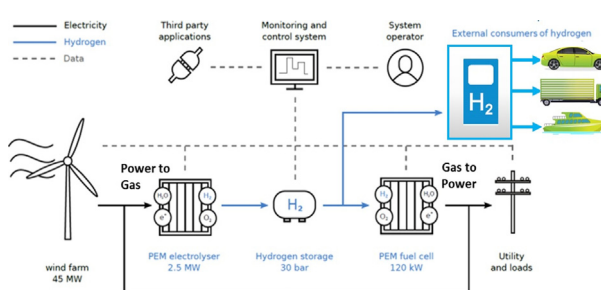
<sup>b</sup> Department of Mechanical Engineering, University of Victoria, 3800, Finnerty Road Victoria, Canada

<sup>c</sup> ENEA Fusion and Nuclear Safety Department, Via Enrico Fermi 45, 00044 Frascati, Rome, Italy

## HIGHLIGHTS

- A novel dynamic model of wind-hydrogen for a multi-level controller.
- Development of an energy storage system to produce hydrogen as a fuel for commercial road vehicles.
- Design of a multi-level MPC to target hydrogen and electricity demands via sequential optimization.
- Degradation issues due to start-up/down, standby, cold and warm sequences included in the model.
- Minimization of the overall operational costs and maximization the profits.

## GRAPHICAL ABSTRACT



## ARTICLE INFO

### Article history:

Received 10 December 2021

Received in revised form

13 July 2022

## ABSTRACT

This study proposes a multi-level model predictive control (MPC) for a grid-connected wind farm paired to a hydrogen-based storage system (HESS) to produce hydrogen as a fuel for commercial road vehicles while meeting electric and contractual loads at the same time. In particular, the integrated system (wind farm + HESS) should comply with the “fuel production” use case as per the IEA-HIA report, where the hydrogen production for fuel cell

<sup>☆</sup> The authors gratefully acknowledge the financial support by the Fuel Cells and Hydrogen 2 Joint Undertaking under the project HAELUS, grant agreement No. 779469.

\* Corresponding author.

E-mail addresses: [bmhammad@unisannio.it](mailto:bmhammad@unisannio.it) (M.B. Abdelghany), [mshehzad@uvic.ca](mailto:mshehzad@uvic.ca) (M.F. Shehzad), [vmariani@unisannio.it](mailto:vmariani@unisannio.it) (V. Mariani), [davide.liuzza@enea.it](mailto:davide.liuzza@enea.it) (D. Liuzza), [glielmo@unisannio.it](mailto:glielmo@unisannio.it) (L. Glielmo).

<http://dx.doi.org/10.1016/j.ijhydene.2022.07.136>

0360-3199/© 2022 The Author(s). Published by Elsevier Ltd on behalf of Hydrogen Energy Publications LLC. This is an open access article under the CC BY license (<http://creativecommons.org/licenses/by/4.0/>).

Accepted 17 July 2022

Available online xxx

**Keywords:**

Energy management

Hydrogen energy conversion

Energy storage

Multi-level model predictive control

Multi-objective optimization

electric vehicles (FCEVs) has the highest unconditional priority among all the objectives. Based on models adopting mixed-integer constraints and dynamics, the problem of external hydrogen consumer requests, optimal load demand tracking, and electricity market participation is solved at different timescales to achieve a long-term plan based on forecasts that then are adjusted at real-time. The developed controller will be deployed onto the management platform of the HESS which is paired to a wind farm established in North Norway within the EU funded project HAEOLUS. Numerical analysis shows that the proposed controller efficiently manages the integrated system and commits the equipment so as to comply with the requirements of the addressed scenario. The operating costs of the devices are reduced by 5%, which corresponds to roughly 300 commutations saved per year for devices.

© 2022 The Author(s). Published by Elsevier Ltd on behalf of Hydrogen Energy Publications LLC. This is an open access article under the CC BY license (<http://creativecommons.org/licenses/by/4.0/>).

Nomenclature			
<i>Devices parameters</i>		$P_g^s$	Grid power of the control layer [kW]
$C^{OM}$	Operating and maintenance cost of the $i$ device [€/h]	$z^s, z_{sell}^s$	Auxiliary variables for hiding a non-linearity in the product of decision variables
$C_{rep}$	Replacement cost of the $i$ device [€/h]	$z^{\geq \gamma}, z^{\leq \gamma}$	Auxiliary variable for combing the discrete logical states of the devices with their corresponding operating powers
$T$	Prediction horizon according to control layer [h]	$\delta^\beta$	Logical variable according to modes of the $i$ device
$H^{max}$	Maximum hydrogen stored in storage tank [kg]	$\sigma_\alpha^\beta$	State transition from $\alpha$ to $\beta$ of the $i$ device
$H^{min}$	Minimum hydrogen stored in storage tank [kg]		
$M$	Upper bound of the function $P$ [kW]	Notations	
$m$	Lower bound of the function $P$ [kW]	$\wedge$	Logical operator AND
$NH$	Cycle life hours of $i$ device [h]	$R^n$	Space of $n$ -dimensional (column) vectors with real entries
$NY$	Number of working hour per year of the $i$ device [h]	$s$	the control layer $s$
$p^{CLD}$	Cold starts power of the $i$ device [kW]	$\alpha, \beta$	Logical states
$p^{max}$	Maximum power of the $i$ device [kW]	$\gamma, \bar{\gamma}$	Power values corresponding to logical state
$p^{min}$	Minimum power of the $i$ device [kW]	$\rho$	Penalty weighting factor
$p^{STB}$	Stand-by power of the $i$ device [kW]		
$p^{WRM}$	Warm starts power of the $i$ device [kW]	Acronyms/Abbreviations	
$R$	Ramp up limits of the $i$ device [kW/h]	BEV	Battery electric vehicle
$T_s$	Sample time for high-level control [h]	CAPEX	Capital expenditure
$\epsilon$	Controller minimum tolerance	EMS	Energy management system
$\eta_i$	Hydrogen storage charging/discharging efficiency	ESS	Energy storage system
$\pi_{pch}^s$	Purchasing energy price [€/kW h]	FCEV	Fuel cell electrical vehicle
$\pi^{sc}$	Energy spot price [€/kWh]	HESS	Hydrogen-based energy storage system
$\pi_{sell}^s$	Selling energy price [€/kWh]	HIA	Hydrogen implementing agreement
<i>Decision and logical variables</i>		HLC	High-level control
$H^s$	Stored level of hydrogen of the control layer [kg]	IEA	International energy agency
$H_{exc}$	Exchange of hydrogen with external consumers [kg]	LLC	Low-level control
$P_{avl}^s$	Available system power of the control layer [kW]	MILP	Mixed-integer linear programming
$P_e^s$	Electrolyzer input power of the control layer [kW]	MLD	Mixed logic dynamic
$P_f^s$	Fuel cell output power of the control layer [kW]	MPC	Model predicative control
		RES	Renewable energy source

**Introduction**

In recent years, many political institutions, at national and international level, have been trying to meet the growing energy demand with increasing production of sustainable and clean energy in response to global climate change and in view

of the limited nature of fossil fuel resources [1,2]. In particular, the transport sector consumes a high percentage of energy that amounts to about 31.8% of the total energy consumed worldwide per year, as the expert group on future transport fuels (EG-FTF) shows [3]. Among all the transportation means, 72.3% of the total consumption comes from road transports. From the point of view of energy vectors, road transportation

significantly (86.3%) depends on oil products (fuel oil, gasoline, diesel, natural gas, liquefied petrol gas, biofuels), and diesel is the most used. For these reasons, scientific research has oriented to the development of alternative solutions to fossil fuels also in this sector.

Currently, zero-emission vehicles are considered as a promising option for the evolution of standard vehicles towards sustainability [4,5]. Examples of zero-emission vehicles are battery electric vehicles (BEVs) and fuel cell electric vehicles (FCEVs). In particular, fast refueling time, higher energy density and modularity characterize the fuel cell systems and, consequently, FCEVs seem more attractive than BEVs. In contrast, the lower reliability and durability of FCEVs compared to conventional vehicles, higher manufacturing costs and lack of hydrogen refueling infrastructure limit their commercialization [6]. Regarding this last point, many strategies can be implemented. Among them, those that can come by leveraging solutions to problems in other domains such as, e.g., energy systems and their green transition, are very appealing because they can imply low costs. For instance, within the main topics of the green transition of energy systems, the integration of renewable energy sources, particularly wind, is an important case. Indeed, the International Energy Agency-Hydrogen Implementing Agreement (IEA-HIA) published a report where three different use cases regarding the possible operations for a wind farm equipped with a hydrogen-based storage system (HES) are identified [7]. The main features that any possible control strategy can lend to the integrated system (wind farm + HES) are presented and discussed for each use case. Among them, the fuel production use case requires that the integrated system be operated to its full range to produce hydrogen for other purposes than re-electrification, such as the provision to FCEVs. Undoubtedly, this operating mode can positively impact the spread of hydrogen technologies for mobility, among others. In addition to the main goal, the IEA-HIA Task 24 final report highlights that additional functionalities should be considered for an integrated system since operating it only toward hydrogen production “[...] plays no role in the management of wind power, as it does not respond to the variable output of either local or distant wind turbines”.

This study regards the development of an MPC strategy to suitably operate HESSs paired to wind farms such as in the framework of the above mentioned IEA-HIA. In particular, the hydrogen is produced to meet the demand for commercial road FCEVs as the main objective and must simultaneously meet electrical and contractual loads with tunable priorities. The degradations due to the working cycles of the HES components where these have a major impact, i.e., the electrolyzer and the fuel cell, are also taken into account through an appropriate modeling using the mixed logic dynamic (MLD) framework [8], which enables to consider the devices' logical states and corresponding switchings in the implemented MPC scheme. The electrolyzers and fuel cells are usually expensive, and their untimely wearing can hinder the widespread adoption of HESSs and the penetration of the integrated systems into the grid as an immediate consequence.

This paper extends the studies presented in Refs. [9,10] by developing and solving a different scenario by means of a

multi-level MPC that takes into account external hydrogen consumer requests, optimal load demand tracking, and electrical market participation. The multi-level architecture is kept across all the previous works because the different control algorithms that are correspondingly developed will be integrated into a unique and consistent software module in the final release of the control platform that will be in charge of operating the system targeted by the HAEOLUS project. The wind-HES is described using MLD to take fully into account device switching dynamics and state formulation. Moreover, the cold and warm starts of the devices have also been included in the system models to achieve feasible real-time optimal operations. Considering such logic states into the control strategy allows for setting control references that result in the reduction of premature unit failures, and also for improving the real-time operations toward the maximization of the revenues by the interaction with external hydrogen consumers and with the utility grid.

In order to achieve the objectives, this paper presents a new energy management strategy such that the integrated system pursues two main objectives:

1. To meet hydrogen demand for road vehicles;
2. To sell energy to the grid through electrical market participation and to supply a local load, after any excess of renewable generation has met the hydrogen demand.

To this aim, two timescales across which the relevant dynamics take place are considered. A larger timescale addresses the control objectives on a daily basis, i.e., the controller has to allocate the optimal amount of hydrogen to be sold to FCEVs based on the day-after expected aggregate demand. Then, based on such allocation, all the extra hydrogen achieved via the wind-power conversion can either be sold to the market to maximize the profit or used to supply a local load. A smaller timescale addresses the deviations due to the inherent unreliability of the forecasts used for the larger timescale and only addresses the market participation and the local load supply.

This research study has important novelties compared to the control strategies that are covered in the literature reviewed in Section Literature review. For instance, the system which controls the real-time energy management of renewable energy systems has been studied, which must react to external disturbances within a short time interval of the order of seconds or minutes. The systems reviewed in the literature cannot exploit the economic benefits of hydrogen demand satisfaction for road vehicles that are made in long-term planning of the energy storage system (ESS). However, long-term planning cannot be applied for real-time power applications, e.g., microgrids, as a great deal of computational effort is required which implies a slowdown in responses.

In summary, the main contributions of the paper are:

1. The development of an MPC scheme for integrated systems targeting the fuel production use case as per the IEA-HIA Task 24 final report;
2. The implementation of a multi-level and multi-stage control architecture such that different and competing control objectives are addressed at the relevant time-scales along with



corresponding priority levels. In particular, unconditional and conditional priority levels are consistently handled;

3. The comprehensive addressing of physical, economical and practical aspects, such as, e.g., the equipment operating and switching costs, their operating constraints, the impact of cold and warm starts in terms of costs during operations and time delays they introduce on the devices switchings, etc.

The paper is organized as follows: the literature review is reported in Section [Literature review](#); the material and methods are shown in Section [Material and methods](#); in Section [Results analysis and discussion](#) simulation results show the validity of the proposed control approach; Section [Conclusions](#) concludes the paper.

## Literature review

Green hydrogen as a fuel for commercial vehicles has attracted the attention of the transportation industry always looking for alternatives to fossil fuels. Moreover, its re-electrification through fuel cells has also been considered as a back-up source to meet the local and contractual loads [11,12]. Particularly, hydrogen production as a fuel for the transport industry gives environmentally friendly advantages over conventional fuels [13]. The authors in Ref. [14] have proposed a modified Weibull distribution function and a log law to model and determine optimal windy sites and turbine configurations to produce wind electricity for hydrogen production. In addition, a policy for hydrogen powered commercial vehicles has been provided with the aim of quick integration into the transportation industry.

The vehicular applications of fuel cells for hydrogen operated vehicles are getting the attention of the transportation industry these days [15]. The microgrid economic dispatch problem, while interacting with external agents, such as FCEVs and BEVs, has been studied in Ref. [16]. There, a microgrid finds the optimal usage of its internal resources by acting in the day-ahead energy market through the forecasts of the generations and the energy price predictions. Depending on the economic schedule, the microgrid controller satisfies the hydrogen and energy demands of the FCEVs and, based on a specific energy market requested by an external agent, supplies the closest energy profile. An MPC-based controller, which includes microgrid feasibility, maintenance, operational and degradation costs, has been developed to dispatch microgrid with external consumers. In Ref. [17] the authors have presented and compared four different types of buses (hydrogen-based, electric-hybrid, conventional and electric-battery). They have concluded that the FCEVs among other buses technologies are the most promising and competitive option especially due to their high energy density. Further, the use of FCEVs in the context of European local public transport has been studied in Ref. [18]. On the other hand, the NewBusfuel project confirms the feasibility of using hydrogen as a fuel for public passenger transports under many situations and in twelve different locations [19].

Many authors have studied hydrogen production in the energy market participation for revenue maximization.

Among them, a novel supervisory MPC technique for HESSs of the power market management has been studied in Ref. [20]. Further, in Refs. [21,22] the MPC framework has been extended using hybrid-ESSs, applied for solar-powered microgrids and validated with respect to the control goals of improving microgrid operational costs and durability. In Ref. [23] a hierarchical MPC has been designed to satisfy the requested load by pairing the renewable energy sources (RESs) with the ESSs. A mixed-integer quadratic programming algorithm based on MPC in Ref. [24] has been designed to ensure the balancing between the power generated by the wind farm and the electrolyzer power consumption in an offshore plant. The wind-hydrogen plant mathematical modeling via mixed-integer linear programming (MILP), including the ESS operational costs, has been studied in Refs. [25–27]. An MILP approach has also been proposed in Ref. [28] to minimize the fuel cell and the battery lifespan degradations, and operation and maintenance costs in marine transportation. The results have demonstrated a reduction in the fuel cell degradations. In Ref. [29] the MPC technique has been used for load sharing in a microgrid equipped with HESS and ultra capacitor. However, important aspects such as the working cycles and the degradation issues of the devices are not included. The same applies to cold and warm starts.

With the provision of the local load satisfaction, an MPC-based algorithm has been implemented in Ref. [30] on an off-grid system. The MPC is characterized by the constraints to limit the charge within the operating ranges of the ESSs and, on the other hand, its objective consists in supplying the required electric load. An off-grid EMS has been proposed in Ref. [31] to control the power flow to and from the storages so as to track the user's requested electrical demand. Another fuel cell and ultracapacitor paired hybrid-ESS has been presented in Ref. [32] where an MPC scheme is used to track the user requested load. Moreover, an EMS based on MPC for a microgrid, which includes HESS, ESS and renewable energy resources, has been studied in Ref. [21]. The MPC strategy enables the electrical load satisfaction in hybrid-ESSs, i.e., systems which include hydrogen and battery for the long-term and short-term, respectively.

In several studies, the degradation issues are included in the cost functions of HESSs, as instance [33,34]. More specifically, these studies show how some aspects (for instance, the power fluctuations or device switching cycles) determine the devices' degradation in the wind-HESS. On the other hand, the models proposed sophisticated fast dynamic features, such as the standby, warm and cold start. Moreover, the study in Ref. [35] has modeled all the degradation issues, except the switching cycles. In Ref. [36], the authors have studied the durability of the proton exchange membrane technology subjected to the operating conditions which cause a lifetime reduction of the electrolyzer and the fuel cell. Consequently, the development of an EMS that both ensures the smooth operation of the devices and achieves other objectives such as high energy efficiency, resiliency, reliability and balance in demand and supply is a demanding challenge. The literature also includes some studies related to the improvement of the durability of the FCEVs. In particular, in Refs. [37,38] a parametric study based on convex optimization has been carried out for the analysis of

the transient power demand on the fuel cell stack. These studies have shown that the fluctuations due to a lack of constraints on the transient power variation affect the resulting power demand on the fuel cell.

As regards energy cost aspects, in Ref. [39] the objective functions take into account both the aging, maintenance and replacement of the devices, and the interaction with the electricity grid for the sale/purchase of energy. Therefore, the MPC controller satisfies both the load demand and maximizes the lifespan of the devices. However, the costs related to the working states switching and the devices' capital are not considered.

Other research studies can be found in the literature where the MPC is developed together with other advanced approaches to achieve optimal ESSs operations. For instance, a scheduling MPC framework has been implemented in Ref. [40] to regulate the state of charge of ESSs subject to stochastic wind and grid demand generations. In order to obtain the net grid power injected into the main grid, the optimization problem is based on a look-ahead policy in the ESS equipped wind farm; the authors in Ref. [41] have described a novel storage device with an embedded health monitoring algorithm based on predictive control with the aim of extending hydrogen devices life spans by minimizing the associated degradation. They have formulated a multi-objective optimization problem, where weighting factors are designed to minimize selected criteria. The results, when compared with the traditional EMSs designed for the FCEVs, have shown the savings on the economic costs for some speed profile, regulating the storage devices in safe range and significantly reducing the energy sources degradation. Furthermore, the MLD framework applied to the MPC controller has been developed for the RESSs-based hybrid co-generation power system in Ref. [42] and for distributed energy resources with a battery-based ESS in Ref. [43]. In Refs. [39,44] an MPC strategy for battery based microgrid optimization has been integrated, as proposed in Refs. [26,27,45] where the MILP has been used for capturing the correct behavior of the ESS paired with the renewable energy plant.

Hydrogen-based EMSs for FCEVs, in particular within the scope of heuristics and rule-based strategies, have also been studied in the literature. For instance, the authors in Ref. [46] have investigated an integrated energy system which includes hydrogen, wind power and photovoltaic systems. They have proposed a multi-objective optimization model to minimize both operating and environmental costs for day-ahead power dispatching. It is shown that carbon emissions are reduced by 3.5% with 2.8% increase of operating costs and operating cost carbon is reduced by 5.12% with 2.6% increase of environmental costs.

The literature also includes a number of other researches within the scope of fuzzy logic EMSs, see for example [47,48]. Their main advantage lies in the simple implementation even in real-time control applications. Moreover, the literature includes studies where authors have adopted adaptive fuzzy logic [49] or wavelet-fuzzy logic [50]. In this regard, a fuzzy logic based control strategy has been developed in Ref. [51] for extended-range FCEVs. The simulation results have shown that the hydrogen consumption by the FCEVs is lower than the on-off and the control power strategies, respectively.

Besides the optimal control schemes, heuristics and meta-heuristics approaches can also be found in the literature. The most adopted heuristic algorithms in the literature include genetic algorithm, simulated annealing, particle swarm optimization, ant colony optimization and duelist algorithm. For instance, the authors in Ref. [52] have presented an advanced EMS that aims at reducing the microgrid running costs via energy storage integration. In particular, they have implemented a battery-based EMS which is used as a backup source for providing power supplies to the load according to energy market profiles. The authors in Ref. [53] have presented a data driven hierarchical multi-objective optimization approach for optimal sizing of the renewable powered (wind and PVs) islanded hydrogen energy system.

The literature also deals with the economic side of the renewable energy production and its applications. Many countries around the globe are investing in the renewable solar to achieve the goals of the Paris Agreement. In this regard, the authors in Ref. [54] have investigated Saudi Arabia's potential for the solar industry, whose projection by 2032 is expected to be 41 GW. In this study, hourly base simulations, which have compared six different renewable power generation systems in several areas, have shown that the hybrid renewable energy system which integrates solar and wind resources through PV array and wind turbines with the battery storage system leads to the lowest cost of energy in Saudi Arabia. In Ref. [55] a techno-economic analysis of a hydrogen refueling station powered by a wind-PV hybrid power system to meet fuelling 25 vehicles per day in Turkey has been carried out. Coppitters et al. in Ref. [56] have presented a computationally efficient robust control strategy for the optimization of a hydrogen-based microgrid under different scenarios. The paper provides a robust optimization design by taking into account the techno-economic uncertainties of the hydrogen-based plants.

Contrarily to the above commented papers, this work does not adopt heuristic methods while it solves mixed-integer optimal problems by means of numerical commercial solvers. Through numerical analysis, it is shown that the derived control problem is solvable within the considered sampling intervals.

In conclusion, equipment costs and degradations aspects are not simultaneously studied in the literature examined above. To this extent, this is one of the novel aspects of this research work. Note instead that the local control of wind turbines is out of the scope of this paper.

## Material and methods

Fundamental notions and methodology are given to provide the control strategy of the integrated system under investigation.

### The MPC algorithm

The MPC was initially introduced for "slow" dynamic systems, such as those found in the process industry, with the idea that a control problem can be formulated as an optimization problem solved on a finite time horizon at each time-step. Then, at the next step, new measurements from the plant

are taken, the horizon is shifted ahead of one sample, and a new iteration occurs. In particular, let us consider the discrete-time dynamical system

$$x_{k+1} = f(x_k, u_k), \quad (1)$$

with state  $x_k, x_{k+1} \in \mathcal{X} \subset \mathbb{R}^n$ , input  $u_k \in \mathcal{U} \subset \mathbb{R}^m$  and initial conditions  $x_0$ . Let us also assume the cost function  $J(x_k, u_k)$  is available and models control objectives and possible requirements that have to be pursued. Other requirements are already taken into account through the state, input and disturbance definition sets that will be included as constraints in the optimization problem. Then, at each time instant  $k$ , the optimal input sequence  $u_k^* = [u_k^*, \dots, u_{k+T}^*]^\top$  over the horizon of duration  $T$  is computed by

$$u_k^* = \arg \min_{u_k^T} \sum_{j=0}^T J(x_{k+j}, u_{k+j}) \quad (2)$$

s.t.

$$x_{k+j+1} = f(x_{k+j}, u_{k+j}),$$

$$x_{k+j} \in \mathcal{X},$$

$$u_{k+j} \in \mathcal{U},$$

where  $j = 1, \dots, T$ . After computing  $u_k^*$ , only  $u_k^*$  is input to the plant, while all the other components are discarded. Then, the time is shifted to the next time-step  $k + 1$  and the procedure is repeated, such that a feedback policy is implemented. In general, optimization techniques provided by standard solvers are used to solve the problem (2).

The MPC technique can be applied for different variables (e.g., integer or logical decisions, hybrid/discontinuous dynamics) and operating constraints (e.g., time delays, working ranges, physical limits). Moreover, in order to use the MPC approach, a good formulation of the system is required. This task may not be trivial, especially for complex systems. The application of the multi-level MPC for solving the problem under consideration is one of the main contributions of this paper.

The MLD formulation introduced in Ref. [8] is used in this paper. Indeed, mixed logic inequalities are useful for modeling the integrated system under investigation which is identified by continuous dynamics (such as hydrogen-based storage units), economic scenarios (such as different electricity tariffs) and switching operating conditions (such as charge/discharge of HESS). Using the transformations in Ref. [8], this hybrid model can be easily expressed by using linear inequalities on which branch and bound techniques can be directly applied. The corresponding sets of inequalities for the structures of interest for this paper are reported in Table 1.

### Preliminaries and notation

Boolean or logical variables take only two values: false (denoted by 0) and true (denoted by 1). Scalars are indicated with lowercase, non-bold letters; column vectors are denoted by lowercase, bold letters; matrices are denoted by uppercase, non-bold letters;  $N = 3$  in case of the three states model and  $N = 5$  in case of the five states model. The subscript  $i$  identifies a particular device, i.e.,  $i = e$  identifies the electrolyzer, and  $i = f$  identifies the fuel cell; the superscript  $s$  identifies a particular

level, i.e.,  $s = \text{HLC}$  identifies the high-level automata, and  $s = \text{LLC}$  identifies the low-level automata. Then, the sets  $\mathcal{I} = \{e, f\}$  and  $\mathcal{S} = \{\text{HLC}, \text{LLC}\}$  are introduced. The formulation of the LLC model is achieved using the sets  $\mathcal{A}^{\text{LLC}}, \mathcal{B}^{\text{LLC}}, \mathcal{C}^{\text{LLC}}, \mathcal{D}^{\text{LLC}}$ , while the HLC model is formulated with the help of the sets  $\mathcal{A}^{\text{HLC}}, \mathcal{B}^{\text{HLC}}, \mathcal{C}^{\text{HLC}}, \mathcal{D}^{\text{HLC}}$ . In particular, for the LLC the sets are defined as  $\mathcal{A}^{\text{LLC}} = \{\text{OFF}, \text{STB}, \text{ON}, \text{CLD}, \text{WRM}\}$ ,  $\mathcal{B}^{\text{LLC}} = \{0, p^{\text{STB}}, p^{\text{min}}, p^{\text{CLD}}, p^{\text{WRM}}\}$  and  $\mathcal{C}^{\text{LLC}} = \{0, p^{\text{STB}}, p^{\text{max}}, p^{\text{CLD}}, p^{\text{WRM}}\}$ , and the set of ordered pairs  $\mathcal{D}^{\text{LLC}} = \{(0, 0), (p^{\text{min}}, p^{\text{max}}), (p^{\text{STB}}, p^{\text{STB}}), (p^{\text{CLD}}, p^{\text{CLD}}), (p^{\text{WRM}}, p^{\text{WRM}})\}$ . In a similar fashion, for the HLC it is  $\mathcal{A}^{\text{HLC}} = \{\text{OFF}, \text{STB}, \text{ON}\}$ ,  $\mathcal{B}^{\text{HLC}} = \{0, p^{\text{STB}}, p^{\text{min}}\}$ ,  $\mathcal{C}^{\text{HLC}} = \{0, p^{\text{STB}}, p^{\text{max}}\}$ , and the set of ordered pairs  $\mathcal{D}^{\text{HLC}} = \{(0, 0), (p^{\text{STB}}, p^{\text{STB}}), (p^{\text{min}}, p^{\text{max}})\}$ . For the convenience of the reader, these sets are reported in Table 2.

For the sake of completeness, the  $n$ -dimensional vector space over the real numbers is  $\mathbb{R}^n$ , the Kronecker product is denoted by  $\otimes$ ,  $\mathbf{1}_n = [1, \dots, 1]^\top$  and  $\mathbf{0}_n = [0, \dots, 0]^\top$  are column vectors of  $n$  unit and zero entries, respectively;  $\mathbf{0}_{n,n}$  and  $\mathbf{I}_n$  denote a  $n \times n$  zeros and identity matrices, respectively;  $\text{diag}(\mu_1, \dots, \mu_n)$  denotes the diagonal  $n \times n$  matrix with diagonal entries  $\mu_1, \dots, \mu_n$ ;  $\mathbf{e}_1 = [1, 0, \dots, 0]^\top, \dots, \mathbf{e}_n = [0, 0, \dots, 1]^\top$  denote the canonical basis of  $\mathbb{R}^n$ . Furthermore, let  $\|\mathbf{y}\|_M^2 = \mathbf{y}^\top \mathbf{M} \mathbf{y}$ . If  $\mathbf{M} = \mathbf{I}_n$ , then the Euclidean norm is obtained  $\|\mathbf{y}\|^2$ .

In this paper, the formulations are proposed in discrete time  $k$ . In particular, mapping to continuous time  $t$  can be obtained by assuming  $t = kT_s$ , where  $T_s$  is the sample time which is equal to 1 h or 10 min according to the considered control layer.

### System dynamic modeling

The HESS models are provided in this subsection. Specifically, discrete time state vector dynamics and physical and operating constraints are described.

#### Integrated system description

The main entities of the scenario under investigation are the wind farm, the HESS (hydrogen tank, electrolyzer and fuel cell), the hydrogen loads, and the local and the contractual loads, as Fig. 1 depicts. The solid green lines, the blue lines, and the red dashed lines refer to the energy flows, the hydrogen flows and data flows, respectively. The power by the wind generator is indicated with  $P_w$ , the input power to the electrolyzer is indicated with  $P_e^{\text{IN}}$ , the output power from the fuel cell is denoted by  $P_f^{\text{OUT}}$ ,  $H_{\text{ref}}$  is the hydrogen reference demand,  $P_g$  is the power injected into the grid, and  $P_{\text{ref}}$  is the local load demand which needs to be met by  $P_{\text{avi}}$ .

Fig. 2 reports the models developed for the implementation of the hierarchical MPC. One automaton modeling the electrolyzer and one automaton modeling the fuel cell are required for each control level. Since the HLC addresses larger timescales of the order of hours, the device cold and warm starts in time intervals of the order of minutes are neglected. Therefore, each corresponding automaton is an instantiation of that including only the red nodes and edges. Regarding the LLC, which is in charge of the real-time operations and therefore addresses shorter timescales of the order of minutes, the devices' cold and warm starts are of concern and cannot be neglected. Therefore, each

**Table 1 – MLD equivalences.**  $M$  is a “large” (w.r.t. to the order of magnitude of other quantities in the problem) positive number,  $m$  is a “small” negative number (e.g.,  $m = -M$ ) and  $\varepsilon$  is a “small” positive number which is typically the machine precision.

Relation	Logic	MLD inequalities
AND ( $\wedge$ )	$s_3 = s_1 \wedge s_2$	$\delta_3 \leq \delta_1$ $\delta_3 \leq \delta_2$ $\delta_3 \geq \delta_1 + \delta_2 - 1$
IFF ( $\Leftrightarrow$ )	$s_1 \Leftrightarrow s_2$ $[s = \text{true}] \Leftrightarrow [f \leq 0]$	$\delta_1 = \delta_2$ $f \leq M(1 - \delta)$ $f \geq \varepsilon + (m - \varepsilon)\delta$
IF-THEN-ELSE	$r_2 = \begin{cases} r_1 & \text{if } s = \text{true} \\ 0 & \text{if } s = \text{false} \end{cases}$	$r_2 \leq M\delta$ $r_2 \geq m\delta$ $r_2 \geq r_1 - M(1 - \delta)$ $r_2 \leq r_1 + m(1 - \delta)$

**Table 2 – Sets used in the paper.**

Set
$\mathcal{I} = \{e, f\}, \quad i \in \mathcal{I}$
$\mathcal{S} = \{\text{HLC}, \text{LLC}\}, \quad s \in \mathcal{S}$
$\mathcal{A}^{\text{LLC}} = \{\text{OFF}, \text{CLD}, \text{STB}, \text{WRM}, \text{ON}\}$
$\mathcal{A}^{\text{HLC}} = \{\text{OFF}, \text{STB}, \text{ON}\}$
$\mathcal{B}^{\text{LLC}} = \{0, p^{\text{CLD}}, p^{\text{STB}}, p^{\text{WRM}}, p^{\text{min}}\}$
$\mathcal{B}^{\text{HLC}} = \{0, p^{\text{STB}}, p^{\text{min}}\}$
$\mathcal{C}^{\text{LLC}} = \{0, p^{\text{CLD}}, p^{\text{STB}}, p^{\text{WRM}}, p^{\text{max}}\}$
$\mathcal{C}^{\text{HLC}} = \{0, p^{\text{STB}}, p^{\text{max}}\}$
$\mathcal{D}^{\text{LLC}} = \{(0, 0), (p^{\text{CLD}}, p^{\text{CLD}}), (p^{\text{STB}}, p^{\text{STB}}), (p^{\text{WRM}}, p^{\text{WRM}}), (p^{\text{min}}, p^{\text{max}})\}$
$\mathcal{D}^{\text{HLC}} = \{(0, 0), (p^{\text{STB}}, p^{\text{STB}}), (p^{\text{min}}, p^{\text{max}})\}$

corresponding automaton is instantiated including the red and blue nodes and edges. In all the following, the subscript refers to the device type that is dropped both for decision variables and for parameters to ease the notation.

The automata depicted in Fig. 2 are augmented with logical variables in order to highlight the link with the MLD modeling. In particular, the logical variable  $\delta^\alpha(k)$  is attached to state  $\alpha$  such that whenever the automata is in state  $\alpha$  at instant  $k$ , correspondingly  $\delta^\alpha(k) = 1$ , while  $\delta^\alpha(k) = 0$  otherwise. Similarly, the logical variable  $\sigma_\alpha^\beta(k)$  is linked to the edge connecting state  $\alpha$  to  $\beta$ , such that when the automata shifts from  $\alpha$  to  $\beta$  at time-step  $k$   $\sigma_\alpha^\beta(k) = 1$ , and  $\sigma_\alpha^\beta(k) = 0$  otherwise. It is important to highlight that at HLC, all the six possible transitions are enabled, while at LLC, this does not hold due to the electrolyzer and fuel cell features. Corresponding constraints will be considered in the MPC controller to prevent such transitions and enable feasible and realistic operations.

#### MLD state constraints

The MLD state constraints of both devices can be derived by taking into account their physical operations and the relevant powers in each operating mode. To start with, let us analyze a device in its ON state. In this case, the relevant power is the input power  $P^{\text{in}}$  which is bounded within  $[p^{\text{min}}, p^{\text{max}}]$ , and by

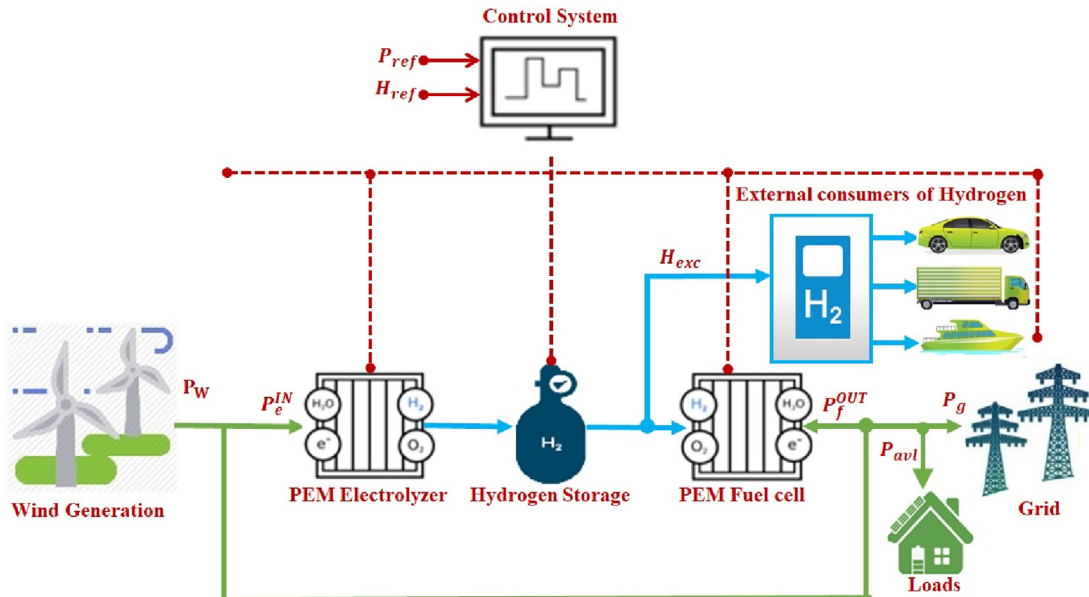


**Fig. 1 – Scenario under investigation.**



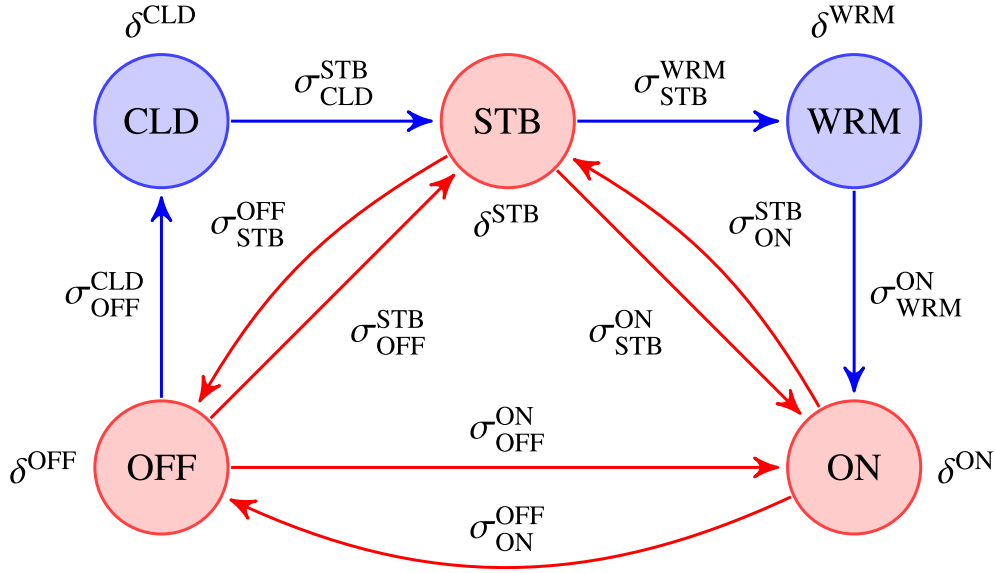


**Fig. 2 – Automata for higher-level and lower-level controls. Each node represents a particular state, while the edges represent the state transition. The red nodes and edges are used for the HLC, while the red nodes and edges with the additional blue ones are used for the LLC. (For interpretation of the references to color in this figure legend, the reader is referred to the Web version of this article.)**

setting  $P^{\text{in}} = P^s(k)\delta^{\text{ON}}(k)$ , it results  $P^s(k) = P^{\text{in}} \in [P^{\text{min}}, P^{\text{max}}]$  whenever  $\delta^{\text{ON}}(k) = 1$ , where  $s = \text{HLC}$  or  $\text{LLC}$ . Similarly, in STB state, the relevant power is  $P^{\text{STB}}$ , and by setting  $P^{\text{STB}} = P^s(k)\delta^{\text{STB}}(k)$  it results  $P^{\text{STB}} = P^s(k)$  whenever  $\delta^{\text{STB}}(k) = 1$ . As for the WRM and CLD states, similar considerations can be deduced. Moreover, since in the OFF state hydrogen production and power consumption do not occur, then  $P^s(k) = 0$ . Formally,

$$P^s(k) = 0 \Leftrightarrow \delta^{\text{OFF}}(k) = 1, \quad (3a)$$

$$P^s(k) = P^{\text{STB}} \Leftrightarrow \delta^{\text{STB}}(k) = 1, \quad (3b)$$

$$P^s(k) \in [P^{\text{min}}, P^{\text{max}}] \Leftrightarrow \delta^{\text{ON}}(k) = 1, \quad (3c)$$

$$P^s(k) = P^{\text{CLD}} \Leftrightarrow \delta^{\text{CLD}}(k) = 1, \quad (3d)$$

$$P^s(k) = P^{\text{WRM}} \Leftrightarrow \delta^{\text{WRM}}(k) = 1, \quad (3e)$$

where (3a)–(3c) pertain to the high-level automata ( $s = \text{HLC}$ ) and (3a)–(3e) pertain to the low-level automata ( $s = \text{LLC}$ ). The logical expressions in (3) are not directly handled by numerical solvers; instead, they require further manipulations to derive equivalent mixed-integer inequalities. As an illustrative example, consider the ON mode. In order to define the condition  $P^s(k) \in [P^{\text{min}}, P^{\text{max}}]$ , two Boolean variables  $z^{\geq P^{\text{min}}}(k)$  and  $z^{\leq P^{\text{max}}}(k)$  need to be defined, as

$$z^{\geq P^{\text{min}}}(k) = \begin{cases} 1 & P^s(k) \geq P^{\text{min}}, \\ 0 & P^s(k) < P^{\text{min}}, \end{cases} \quad (4a)$$

$$z^{\leq P^{\text{max}}}(k) = \begin{cases} 0 & P^s(k) > P^{\text{max}}, \\ 1 & P^s(k) \leq P^{\text{max}}, \end{cases} \quad (4b)$$

which, according to the MLD equivalences reported in Table 1, are equivalent to

$$\begin{aligned} P^s(k) - P^{\text{min}} &\leq (M + \epsilon) z^{\geq P^{\text{min}}}(k) - \epsilon, \\ -P^s(k) + P^{\text{min}} &\leq M (1 - z^{\geq P^{\text{min}}}(k)); \end{aligned} \quad (5a)$$

$$\begin{aligned} -P^s(k) + P^{\text{max}} &\leq (M + \epsilon) z^{\leq P^{\text{max}}}(k) - \epsilon, \\ P^s(k) - P^{\text{max}} &\leq M (1 - z^{\leq P^{\text{max}}}(k)); \end{aligned} \quad (5b)$$

where  $M > 0$  is an upper bound and  $m = -M$  is a lower bound of  $P^s(k)$ . Then, (3c) is rewritten as

$$(1 - \delta^{\text{ON}}(k)) + z^{\geq P^{\text{min}}}(k) \geq 1, \quad (6a)$$

$$(1 - \delta^{\text{ON}}(k)) + z^{\leq P^{\text{max}}}(k) \geq 1. \quad (6b)$$

Similar considerations have to be applied to the remaining equations in (3).

Let us now introduce the matrices

$$V^{\text{LLC}}(k) = \begin{bmatrix} \delta^{\text{OFF}} & z^{\geq 0} & z^{\leq 0} \\ \delta^{\text{STB}} & z^{\geq P^{\text{STB}}} & z^{\leq P^{\text{STB}}} \\ \delta^{\text{ON}} & z^{\geq P^{\text{min}}} & z^{\leq P^{\text{max}}} \\ \delta^{\text{CLD}} & z^{\geq P^{\text{CLD}}} & z^{\leq P^{\text{CLD}}} \\ \delta^{\text{WRM}} & z^{\geq P^{\text{WRM}}} & z^{\leq P^{\text{WRM}}} \end{bmatrix}, \quad \Gamma^{\text{LLC}} = \begin{bmatrix} 0 & 0 \\ P^{\text{STB}} & P^{\text{STB}} \\ P^{\text{min}} & P^{\text{max}} \\ P^{\text{CLD}} & P^{\text{CLD}} \\ P^{\text{WRM}} & P^{\text{WRM}} \end{bmatrix}, \quad (7)$$

for the five states automata, and

$$V^{\text{HLC}}(k) = \begin{bmatrix} \delta^{\text{OFF}} & z^{\geq 0} & z^{\leq 0} \\ \delta^{\text{STB}} & z^{\geq P^{\text{STB}}} & z^{\leq P^{\text{STB}}} \\ \delta^{\text{ON}} & z^{\geq P^{\text{min}}} & z^{\leq P^{\text{max}}} \end{bmatrix}, \quad \Gamma^{\text{HLC}} = \begin{bmatrix} 0 & 0 \\ P^{\text{STB}} & P^{\text{STB}} \\ P^{\text{min}} & P^{\text{max}} \end{bmatrix}, \quad (8)$$

for the three state automata, where  $V^{\text{HLC}} = W V^{\text{LLC}}$ ,  $\Gamma^{\text{HLC}} = W \Gamma^{\text{LLC}}$  with  $W = [I_3 \ 0_{3,2}]$  being a suitable matrix whose extended definition is provided in Appendix A. In what follows, we derive the MLD equations in matrix form. To this aim, we will use the products  $V^s(k)e_\ell$  with  $\ell \in \{1, 2, 3\}$  and  $\Gamma^s e_\ell$  with  $\ell \in \{1, 2\}$  with the column  $e_\ell$  of appropriate dimension. With this notation, e.g.,  $V^s(k)e_2$  and  $V^s(k)e_3$  are the slack

vectors required to determine the logical state vector  $V^s e_1$  with respect to the corresponding relevant powers  $\Gamma^s e_1$  and  $\Gamma^s e_2$ . Specifically, the compact form of the inequalities in (3) is given by

$$[V^s(k)e_1 = \mathbf{1}_N] \Leftrightarrow [P^s(k)\mathbf{1}_N \geq \Gamma^s e_1, P^s(k)\mathbf{1}_N \leq \Gamma^s e_2], \quad (9)$$

with  $N = 3$  for  $s = \text{HLC}$  and  $N = 5$  for  $s = \text{LLC}$ . Similarly, the set of inequalities in (5) and (6) for the ON state and the similar inequalities for the other states can be defined in matrix form as

$$-(M + \varepsilon)V^s(k)e_2 \leq -P^s(k)\mathbf{1}_N + \Gamma^s e_1 - \varepsilon\mathbf{1}_N, \quad (10a)$$

$$MV^s(k)e_2 \leq P^s(k)\mathbf{1}_N - \Gamma^s e_1 + M\mathbf{1}_N,$$

$$-(M + \varepsilon)V^s(k)e_3 \leq P^s(k)\mathbf{1}_N - \Gamma^s e_2 - \varepsilon\mathbf{1}_N, \quad (10b)$$

$$MV^s(k)e_3 \leq -P^s(k)\mathbf{1}_N + \Gamma^s e_2 + M\mathbf{1}_N,$$

and

$$(\mathbf{1}_N - V^s(k)e_1) + V^s(k)e_2 \geq \mathbf{1}_N, \quad (11a)$$

$$(\mathbf{1}_N - V^s(k)e_1) + V^s(k)e_3 \geq \mathbf{1}_N, \quad (11b)$$

respectively. In addition, the mutually exclusive conditions

$$\mathbf{1}_N^\top V^s(k)e_1 = 1 \quad (12)$$

has to be also considered due to the fact that each device may stay in only one state at each time-step  $k$ . The operations of the devices are independent of each other such that the controller can enable non mutually exclusive operations, e.g., with the electrolyzer and the fuel cell being on at the same time. The controller can use this extra degree of freedom to minimize the switching costs that are taken into account by the corresponding cost functions. Thus, it could happen that, e.g., if the electrolyzer is on and the fuel cell is required to switch on from standby, the controller is free to decide not to switch the electrolyzer off or standby, precisely because this would imply too many switchings for the electrolyzer increasing, therefore, the related costs.

#### MLD constraints of the state transitions

For each automaton shown in Fig. 2,  $N \times (N - 1)$  possible state transitions are implied, where  $N$  is the number of modes. So, the HLC model has 6 possible mode transitions ( $N = 3$ ), while the LLC model implies 20 possible mode transitions ( $N = 5$ ). However, not all transitions can be enabled for  $N = 5$ . Indeed, some of them cannot take place on real devices due to their inherent functioning (and they do not appear in Fig. 2).

The transition connecting state  $\alpha$  to  $\beta$  can be defined in terms of  $\delta^s$ , so that when the automata shifts from state  $\alpha$  to state  $\beta$  at the time-step  $k$ , then  $\sigma_\alpha^\beta(k) = 1$ , while  $\sigma_\alpha^\beta(k) = 0$  otherwise. Thus,

$$\sigma_\alpha^\beta(k) = \delta^\alpha(k-1) \wedge \delta^\beta(k), \quad (13)$$

with  $\alpha, \beta \in \mathcal{A}^s$ ,  $\alpha \neq \beta$ , and  $s \in \{\text{HLC}, \text{LLC}\}$ . The definition in (13) can be converted into three inequalities and provided as constraints in the proposed MPC controller, according to MLD equivalences in Table 1. Notice that, although  $\sigma_\alpha^\beta(k)$  plays the role of a logic variable, it is defined in the continuous interval  $[0, 1]$ , rather than in the set  $\{0, 1\}$ . This relaxation, useful for

computational efficiency, is possible since, due to the above formula and Table 1,  $\sigma_\alpha^\beta(k)$  will indeed only assume values at the boundary of the interval  $[0, 1]$ . As an illustrative example, the OFF-ON state transition is equivalently converted into the following inequalities

$$\begin{aligned} -\delta^{\text{OFF}}(k-1) + \sigma_{\text{OFF}}^{\text{ON}}(k) &\leq 0, \\ -\delta^{\text{ON}}(k) + \sigma_{\text{OFF}}^{\text{ON}}(k) &\leq 0, \\ \delta^{\text{OFF}}(k-1) + \delta^{\text{ON}}(k) - \sigma_{\text{OFF}}^{\text{ON}}(k) &\leq 1. \end{aligned} \quad (14)$$

Similarly, the inequalities for the HLC/LLC and corresponding other states can be derived. In order to provide a compact form of the inequality constraints for the state transitions, the vectors

$$\sigma^{\text{LLC}}(k) = \begin{bmatrix} \sigma_{\text{OFF}}^{\text{STB}} & \sigma_{\text{OFF}}^{\text{ON}} & \sigma_{\text{OFF}}^{\text{CLD}} & \sigma_{\text{OFF}}^{\text{WRM}} \\ \sigma_{\text{STB}}^{\text{OFF}} & \sigma_{\text{STB}}^{\text{ON}} & \sigma_{\text{STB}}^{\text{CLD}} & \sigma_{\text{STB}}^{\text{WRM}} \\ \sigma_{\text{ON}}^{\text{OFF}} & \sigma_{\text{ON}}^{\text{STB}} & \sigma_{\text{ON}}^{\text{CLD}} & \sigma_{\text{ON}}^{\text{WRM}} \\ \sigma_{\text{CLD}}^{\text{OFF}} & \sigma_{\text{CLD}}^{\text{STB}} & \sigma_{\text{CLD}}^{\text{ON}} & \sigma_{\text{CLD}}^{\text{WRM}} \\ \sigma_{\text{WRM}}^{\text{OFF}} & \sigma_{\text{WRM}}^{\text{STB}} & \sigma_{\text{WRM}}^{\text{ON}} & \sigma_{\text{WRM}}^{\text{CLD}} \end{bmatrix}^\top \quad (15)$$

for five state automata and

$$\sigma^{\text{HLC}}(k) = [\sigma_{\text{OFF}}^{\text{STB}} \quad \sigma_{\text{OFF}}^{\text{ON}} \quad \sigma_{\text{STB}}^{\text{ON}} \quad \sigma_{\text{STB}}^{\text{OFF}} \quad \sigma_{\text{ON}}^{\text{OFF}} \quad \sigma_{\text{ON}}^{\text{STB}}]^\top \quad (16)$$

for the three state automata are introduced. Then, the set of inequalities in (14) for the OFF-ON state transition and the similar inequalities for the other transitions can be defined in matrix form as

$$\begin{aligned} L\sigma^s(k) &\leq V^s(k-1)e_1 \otimes \mathbf{1}_{N-1}, \\ L\sigma^s(k) &\leq \Lambda^s V^s(k)e_1, \\ L\sigma^s(k) &\geq V^s(k-1)e_1 \otimes \mathbf{1}_{N-1} + \Lambda^s V^s(k)e_1 - \mathbf{1}_{N(N-1)}, \end{aligned} \quad (17)$$

with  $N = 3$  for  $s = \text{HLC}$  and  $N = 5$  for  $s = \text{LLC}$ , and the matrices  $L$  and  $\Lambda^s$  are provided in Appendix A. The matrix  $L$  selects the admissible transitions out of all the theoretically possible from the automata in Fig. 2 and the matrix  $\Lambda^s$  is the circular shift matrix obtained by considering all possible state transitions. Along with (17) also the constraint

$$\bar{L}\sigma^s(k) = 0, \quad (18)$$

has to be considered, where the matrix  $\bar{L}$  (see Appendix A) selects all the not admissible transitions out of all the theoretically possible from the automata in Fig. 2, which have to be forced to zero in the proposed MPC controller. It is worth pointing out that since all six possible transitions are allowed in three states model, the devices cost function for the HLC includes all of them. Thus, (18) does not apply to the three states model. The complete list of the state transitions for both control levels is reported in Refs. [10,57].

#### Temporal constraints

Both devices have inherent restrictions for the switching time between the feasible states, which is reflected in the five state automaton, which includes the additional CLD and WRM states. Such states are transient since the device does not settle indefinitely in either one or the other. Instead, they are active only for a short interval and are relevant for shorter timescales only. For the five state automaton, it is only necessary to include the following timing constraints [9]:

$$[1_{T^c} \otimes e_{CLD}^T][V^{LLC}(k)e_1 - V^{LLC}(k-1)e_1] \leq [I_{T^c} \otimes e_{CLD}^T]v_{CLD}^{LLC}, \quad (19a)$$

$$e_{CLD}^T[V^{LLC}(k)e_1 + \dots + V^{LLC}(k-T^c)e_1] \leq T^c, \quad (19b)$$

$$[1_{T^w} \otimes e_{WRM}^T][V^{LLC}(k)e_1 - V^{LLC}(k-1)e_1] \leq [I_{T^w} \otimes e_{WRM}^T]v_{WRM}^{LLC}, \quad (19c)$$

$$e_{WRM}^T[V^{LLC}(k)e_1 + \dots + V^{LLC}(k-T^w)e_1] \leq T^w, \quad (19d)$$

where  $v_{CLD}^{LLC}$  and  $v_{WRM}^{LLC}$  are the vectors

$$v_{CLD}^{LLC} = [(V^{LLC}(k+1)e_1)^T, \dots, (V^{LLC}(k+T^c)e_1)^T]^T, \quad (20a)$$

$$v_{WRM}^{LLC} = [(V^{LLC}(k+1)e_1)^T, \dots, (V^{LLC}(k+T^w)e_1)^T]^T. \quad (20b)$$

In (20)  $T^c$  ( $T^w$ ) indicates the cold (warm) start time required to switch from OFF (STB) to STB (ON).

### Hydrogen storage dynamics

The dynamics of the hydrogen level in the tank is given by

$$H^s(k+1) = H^s(k) - H_{exc}^s(k) + \eta_e z_e^s(k)T_s - \frac{z_f^s(k)T_s}{\eta_f}, \quad (21)$$

with  $s \in \{HLC, LLC\}$ ,  $z_e^s(k) = P_e^s(k)\delta_e^{ON}(k)$  and  $z_f^s(k) = P_f^s(k)\delta_f^{ON}(k)$  and  $H_{exc}^s(k)$  is a term which models hydrogen export for supplying demand from commercial road vehicles or other possible customers. From (21), it follows that the electrolyzer/fuel cell produces/consumes hydrogen only when they are in the ON state. Notice that the efficiencies  $\eta_e$  and  $\eta_f$  in (21) are constant values and can be possibly updated when a significant deviation with respect to the current adopted values is measured.

### Modeling of the utility grid

The energy selling to the grid is modeled by means of the logical variable  $\delta_{sell}^s(k)$ : the interaction with the main grid determines if  $\delta_{sell}^s(k) = 1$  (activation) or  $\delta_{sell}^s(k) = 0$  (deactivation). Then, the following constraint holds

$$\delta_{sell}^s(k) = \begin{cases} 1, & P_g^s(k) \leq \xi_g \\ 0, & P_g^s(k) > \xi_g, \end{cases} \quad (22)$$

where  $s \in \{HLC, LLC\}$ ,  $P_g^s(k)$  is the grid power that models the possibility to sell energy to the utility grid,  $\xi_g = 0$  for  $s = HLC$ ,  $\xi_g = (P_g^{HLC}(k))^*$  for  $s = LLC$ , with  $(P_g^{HLC}(k))^*$  being the optimal schedule computed by the HLC and fed to the LLC, which has to compensate for the deviations of the actual grid power in real time. The constraint (22) is equivalent to the following MLD formulas:

$$\begin{aligned} -P_g^s(k) + \xi_g &\leq (M_g + \varepsilon)\delta_{sell}^s(k) - \varepsilon, \\ P_g^s(k) - \xi_g &\leq M_g(1 - \delta_{sell}^s(k)), \end{aligned} \quad (23)$$

where  $M_g$  is an upper bound of the function  $P_g^s(k) - \xi_g$ . In order to model the grid connection events, the auxiliary slack variable  $z_{sell}^s(k)$  is defined as

$$z_{sell}^s(k) = -(P_g^s(k) - \xi_g)\delta_{sell}^s(k), \quad (24)$$

with  $s \in \{HLC, LLC\}$ . It is worth noticing that the market participation is addressed even though only energy selling is considered, because the integrated system's main purpose is not to supply a local load nor to generate hydrogen by buying energy from the grid. The slack variables  $z_{sell}^s$  hide a non-linearity in the product of two decision variables which would otherwise make the problem nonlinear and difficult to handle by numerical solvers. The definition (24) can be recast linearly as

$$\begin{aligned} z_{sell}^s(k) &\leq m_g \delta_{sell}^s(k), \\ z_{sell}^s(k) &\geq M_g \delta_{sell}^s(k), \\ z_{sell}^s(k) &\geq (P_g^s(k) - \xi_g) - M_g(1 - \delta_{sell}^s(k)), \\ z_{sell}^s(k) &\leq (P_g^s(k) - \xi_g) + m_g(1 - \delta_{sell}^s(k)). \end{aligned} \quad (25)$$

### Ramp up limits

An instantiation of the constraint

$$|[P^s(k) - P^s(k-1)]e_{ON}^T V^s(k)e_1| \leq R \quad (26)$$

for each device limits the slew rate of the input and output powers of the electrolyzer and the fuel cell, respectively, to reduce the probability of damage of the devices. In (26)  $R$  is the ramp limit of a device in [kW/h]; the mixed product can be equivalently defined through the set of inequalities as reported in Table 1. For the problem at hand, the value of  $R$  will be higher than each allowable power variation when commuting among different discrete states in the automaton in Fig. 2.

### Grid-side power balance constraint

The following power balance equation

$$P_w^s(k) - z_e^s(k) + z_f^s(k) - P_{avl}^s(k) = P_g^s(k) \quad (27)$$

must be taken into account at each time instant  $k$  to guarantee the controller feasibility. From (27), the power balance equality constraint highlights that the available system power  $P_{avl}^s(k)$  depends on the power  $P_w^s(k)$  achieved through wind generation and the balancing action of the hydrogen storage system.

### Feasibility and physical constraints

The electrolyzer and the fuel cell have operating range limits that will be taken into account by the controller via corresponding instances of

$$p^{\min} \leq P^s(k) \leq p^{\max}. \quad (28)$$

Also, the stored hydrogen  $H^s$  in the tank has to be kept within the minimum and the maximum limits according to the operating ranges of the tank, i.e.,

$$H^{\min} \leq H^s(k) \leq H^{\max}. \quad (29)$$

### Optimization problem

In this section the electrolyzer and the fuel cell cost functions, the grid cost functions, the local load tracking cost functions, and the hydrogen tracking cost function are given. Such cost functions will be later combined to design the multi-level MPC. In what follows, for the HLC and LLC, the corresponding time-steps, sample times and horizons are indicated with

the same letters  $k$ ,  $T_s$  and  $T$  for notational convenience and readability. This choice is also adopted for all the variables involved and enables a lighter notation without impairing the understanding, and the context will solve the ambiguity.

#### Grid cost functions

This section introduces the interconnection with the utility grid for the sale of energy according to the timescales of the energy markets. For instance, for intraday market participation, the grid formulations have been developed within the sampling time of 1 h by considering the hourly energy price profiles, whereas, the LLC corresponds to the real-time energy market with sampling time of 10 min. Note that in the Norwegian market the prices are given only on an hourly basis, and then they are sampled to be adapted to the sampling time of the LLC.

**Cost function for intraday market participation.** In order to explain the intraday market cost function, the vectors  $\mathbf{z}_{\text{sell}}^{\text{HLC}}$  and  $\boldsymbol{\pi}_{\text{sell}}^{\text{HLC}}$ , which collect the electric power to be exchanged with the grid and the corresponding energy prices, respectively, at time instant  $k$  and across the horizon  $T$  ahead in time, are introduced. Thus, the selling energy revenues are modeled by the following cost function

$$J_{\text{grid}}^{\text{HLC}}(k) = -[\boldsymbol{\pi}_{\text{sell}}^{\text{HLC}}]^T \mathbf{z}_{\text{sell}}^{\text{HLC}} T_s, \quad (30)$$

where

$$\begin{aligned} \boldsymbol{\pi}_{\text{sell}}^{\text{HLC}} &= [\pi_{\text{sell}}^{\text{HLC}}(k), \dots, \pi_{\text{sell}}^{\text{HLC}}(k+T)]^T, \\ \mathbf{z}_{\text{sell}}^{\text{HLC}} &= [z_{\text{sell}}^{\text{HLC}}(k), \dots, z_{\text{sell}}^{\text{HLC}}(k+T)]^T. \end{aligned} \quad (31)$$

Notice that the signal related to the selling of energy is negative. This is done with the aim of maximizing the benefits of the revenue of selling energy. For further mathematical details and modeling, we refer to Ref. [9].

**Cost function for real-time market participation.** The cost function derived for the real-time market participation takes into account the fact that any deviation from the contract signed by the parties results in heavy penalties that are imposed by the system operator. The real-time electrical market participation is given analogously to the HLC case as

$$J_{\text{grid}}^{\text{LLC}}(k) = -[\boldsymbol{\pi}_{\text{sell}}^{\text{LLC}}]^T \mathbf{z}_{\text{sell}}^{\text{LLC}} T_s, \quad (32)$$

where the real-time market profiles  $\boldsymbol{\pi}_{\text{sell}}^{\text{LLC}}$  and the auxiliary variables  $\mathbf{z}_{\text{sell}}^{\text{LLC}}$ , at time instant  $k$  and across the control horizon  $T$ , are respectively given by

$$\begin{aligned} \boldsymbol{\pi}_{\text{sell}}^{\text{LLC}} &= [\pi_{\text{sell}}^{\text{LLC}}(k), \dots, \pi_{\text{sell}}^{\text{LLC}}(k+T)]^T, \\ \mathbf{z}_{\text{sell}}^{\text{LLC}} &= [z_{\text{sell}}^{\text{LLC}}(k), \dots, z_{\text{sell}}^{\text{LLC}}(k+T)]^T. \end{aligned} \quad (33)$$

#### Operating cost functions

The device operations imply costs deriving by the energy spent during standby or cold and warm starts depend on the particular level considered, the number of state switchings and the amount of working hours that affect many aspects. These costs can be accounted for by means of appropriate cost

functions that will be introduced in this section. Since the costs pertain both the electrolyzer and the fuel cell, for each of them an instantiation of the reported cost functions will be considered in the controller and therefore, according to the notational style of the paper and as stated in Section [System dynamic modeling](#), the subscript denoting the specific device decision variables and parameters is dropped.

**HLC operating cost functions.** At the HLC, that is for the three state model, the cost functions for the operating costs of the electrolyzer and the fuel cell are a corresponding instantiation of

$$\begin{aligned} J^{\text{HLC}}(k) &= \left( \frac{c^{\text{rep}}}{\text{NH}} + c^{\text{OM}} \right) [\mathbf{1}_T \otimes \mathbf{e}_{\text{ON}}]^T \mathbf{v}_1^{\text{HLC}} \\ &\quad + [\mathbf{1}_T \otimes \mathbf{c}_{\sigma}^{\text{HLC}}]^T \boldsymbol{\sigma}_k^{\text{HLC}} \\ &\quad + \mathbf{P}^{\text{STB}} [\boldsymbol{\pi}^{\text{sc}}]^T [\mathbf{I}_T \otimes \mathbf{e}_{\text{STB}}^T] \mathbf{v}_1^{\text{HLC}}, \end{aligned} \quad (34)$$

where  $\mathbf{v}_1^{\text{HLC}} = [(\mathbf{V}^{\text{HLC}}(k)\mathbf{e}_1)^T, \dots, (\mathbf{V}^{\text{HLC}}(k+T)\mathbf{e}_1)^T]^T$  is the vector of logical variable,  $c^{\text{rep}}$  is the stack replacement cost, NH is the cycles lifespan,  $c^{\text{OM}}$  is the operating and maintenance cost, the vector  $\boldsymbol{\sigma}_k^{\text{HLC}}$  is given by

$$\boldsymbol{\sigma}_k^{\text{HLC}} = [\boldsymbol{\sigma}_k^{\text{HLC}}(k), \dots, \boldsymbol{\sigma}_k^{\text{HLC}}(k+T)]^T. \quad (35)$$

$\mathbf{c}_{\sigma}^{\text{HLC}} = [c_{\text{OFF}}^{\text{STB}}, c_{\text{OFF}}^{\text{ON}}, c_{\text{STB}}^{\text{ON}}, c_{\text{STB}}^{\text{OFF}}, c_{\text{ON}}^{\text{OFF}}, c_{\text{ON}}^{\text{STB}}]^T$  is the vector of the startup, shutdown and standby costs and  $\boldsymbol{\pi}^{\text{sc}} = [\pi^{\text{sc}}(k), \dots, \pi^{\text{sc}}(k+T)]^T$  is the column vector of power spot prices. For further mathematical details of the HLC cost functions, we refer the reader to Ref. [58].

**LLC operating cost functions.** At the LLC, the cost functions for the account of the operating costs differ from those at the HLC in that they include the scheduled references of energy and power provided by the economical dispatch achieved by the HLC by means of the forecasts, and they target the enabled mode transitions of the five states automata. Clearly, the references scheduled by the HLC are constant within the time intervals spanned by the LLC at each corresponding iteration. In practice, for both devices a corresponding instantiation of

$$\begin{aligned} J^{\text{LLC}}(k) &= \left( \frac{c^{\text{rep}}}{\text{NH}} + c^{\text{OM}} \right) [\mathbf{1}_T \otimes \mathbf{e}_{\text{ON}}]^T \mathbf{v}_1^{\text{LLC}} \\ &\quad + [\mathbf{1}_T \otimes \mathbf{c}_{\sigma}^{\text{LLC}}]^T L_{\sigma^{\text{LLC}}} \boldsymbol{\sigma}_k^{\text{LLC}} \\ &\quad + \mathbf{P}^{\text{STB}} [\boldsymbol{\pi}^{\text{sc}}]^T [\mathbf{I}_T \otimes \mathbf{e}_{\text{STB}}^T] \mathbf{v}_1^{\text{LLC}} \\ &\quad + \mathbf{P}^{\text{CLD}} [\boldsymbol{\pi}_k^{\text{sc}, T}]^T [\mathbf{I}_T \otimes \mathbf{e}_{\text{CLD}}^T] \mathbf{v}_1^{\text{LLC}} \\ &\quad + \mathbf{P}^{\text{WRM}} [\boldsymbol{\pi}^{\text{sc}}]^T [\mathbf{I}_T \otimes \mathbf{e}_{\text{WRM}}^T] \mathbf{v}_1^{\text{LLC}} \\ &\quad + \omega^H \|\mathbf{h}^{\text{LLC}} - \mathbf{H}^{\text{HLC}} \mathbf{1}_T\|^2 + \omega^P \|\mathbf{z}^{\text{LLC}} - \mathbf{z}^{\text{HLC}} \mathbf{1}_T\|^2, \end{aligned} \quad (36)$$

where  $\mathbf{v}_1^{\text{LLC}} = [(\mathbf{V}^{\text{LLC}}(k)\mathbf{e}_1)^T, \dots, (\mathbf{V}^{\text{LLC}}(k+T)\mathbf{e}_1)^T]^T$  is the vector of the logical variables in the first columns of  $\mathbf{V}^{\text{LLC}}(k)\mathbf{e}_1, \dots, \mathbf{V}^{\text{LLC}}(k+T)\mathbf{e}_1$ ,  $c^{\text{rep}}$ ,  $c^{\text{OM}}$  and NH have same meaning of the similar terms in (34),  $\mathbf{c}_{\sigma}^{\text{LLC}} = [c_{\text{STB}}^{\text{OFF}}, c_{\text{ON}}^{\text{OFF}}, c_{\text{CLD}}^{\text{STB}}]^T$  is the vector of the device cycle costs,  $L_{\sigma^{\text{LLC}}}$  is a suitable matrix reported in Appendix A, which selects the transitions states ( $\sigma_{\text{ON}}^{\text{OFF}}, \sigma_{\text{CLD}}^{\text{STB}}, \sigma_{\text{STB}}^{\text{OFF}}$ ) from the defined vector  $\boldsymbol{\sigma}^{\text{LLC}}$ . For further mathematical details of the LLC device operating cost functions we refer the reader to Ref. [10].



A substantial difference between (34) and (36) is that, in the latter case, two additional terms are considered, which represent the hydrogen and power reference tracking, with such reference provided by the HLC (the latter with sampling rates which are subsampling of the LLC one). Specifically, we define  $\mathbf{z}^{\text{LLC}} = [z^{\text{LLC}}(k), \dots, z^{\text{LLC}}(k+T)]^\top$ . The term  $\omega^H \|\mathbf{h}^{\text{LLC}} - H^{\text{HLC}} \mathbf{1}_T\|^2$ , according to the weight  $\omega^H$ , accounts for the deviation of the real-time hydrogen level  $\mathbf{h}^{\text{LLC}}$  in the tank at time-step  $k$  and across the horizon  $T$  from the level  $H^{\text{HLC}}$  scheduled by the HLC for the referenced time interval. The term  $\omega^P \|\mathbf{z}^{\text{LLC}} - z^{\text{HLC}} \mathbf{1}_T\|^2$ , according to the weight  $\omega^P$ , accounts for the deviation of the real-time available power  $\mathbf{z}^{\text{LLC}}$  at time-step  $k$  and across the horizon  $T$  from the level  $z^{\text{HLC}}$  scheduled by the HLC for the referenced time interval.

#### Cost function for load tracking

Similarly to the other costs, the load demand is also tracked in both control layers.

*Cost function for HLC load tracking.* The load tracking cost is computed as the mismatch between  $\mathbf{p}_{\text{avl}}^{\text{HLC}}(k)$  and  $\mathbf{p}_{\text{ref}}^{\text{HLC}}(k)$ , i.e.,

$$J_d^{\text{HLC}}(k) = \|\mathbf{p}_{\text{avl}}^{\text{HLC}} - \mathbf{p}_{\text{ref}}^{\text{HLC}}\|^2, \quad (37)$$

where  $\mathbf{p}_{\text{avl}}^{\text{HLC}} = [p_{\text{avl}}^{\text{HLC}}(k), \dots, p_{\text{avl}}^{\text{HLC}}(k+T)]^\top$  is the available power vector and  $\mathbf{p}_{\text{ref}}^{\text{HLC}} = [p_{\text{ref}}^{\text{HLC}}(k), \dots, p_{\text{ref}}^{\text{HLC}}(k+T)]^\top$  is the vector of the load demand forecasts at time instant  $k$  and across the control horizon  $T$ .

*Cost function for LLC load tracking.* For real-time operations, the load tracking is achieved through the minimization of

$$J_d^{\text{LLC}}(k) = \mathbf{p}_{\text{avl}}^{\text{LLC}} - \mathbf{p}_{\text{avl}}^{\text{HLC}} \mathbf{1}_T^2, \quad (38)$$

where  $\mathbf{p}_{\text{avl}}^{\text{LLC}}$  is the available system power and  $\mathbf{p}_{\text{avl}}^{\text{HLC}}$  is the scheduled available power that is needed to be tracked by the LLC.

#### Cost function for hydrogen tracking

One main task of the HLC is to track the hydrogen reference demand  $H_{\text{ref}}^{\text{HLC}}$ . To this aim, the cumulative squared error

$$J_H^{\text{HLC}}(k) = \mathbf{h}_{\text{exc}}^{\text{HLC}} - \mathbf{h}_{\text{ref}}^{\text{HLC}2} \quad (39)$$

between the hydrogen reference  $\mathbf{h}_{\text{ref}}^{\text{HLC}} = [H_{\text{ref}}^{\text{HLC}}(k), \dots, H_{\text{ref}}^{\text{HLC}}(k+T)]^\top$  and the corresponding decisions  $\mathbf{h}_{\text{exc}}^{\text{LLC}} = [H_{\text{exc}}^{\text{LLC}}(k), \dots, H_{\text{exc}}^{\text{LLC}}(k+T)]^\top$  is considered. For the reader's convenience, a comparison between the HLC and the LLC policies is reported in Table 3, where, for clarity, the less compact form of the cost functions presented in Refs. [9,58] is used.

#### Controller design

The block scheme of the proposed multi-level controller is shown in Fig. 3. The LLC executes every 10 min with a scheduled

horizon of 1 h, while the HLC executes every 1 h with a scheduled horizon of 24 h. In this way, the HLC optimization can be performed on longer timescales with low resolution, while for the real-time dynamics considered in the LLC, higher resolution is achieved. As it can be noticed, at the HLC the scheme features a sequential approach where firstly the hydrogen demand tracking is addressed. Then, the achieved optimal hydrogen level  $(J_H^{\text{HLC}})^*$  in the tank is used as a constraint in the following optimization stage where the load tracking demand and the participation to the electricity market are addressed. In this way, the hydrogen production for FCEVs is obtained with the unconditional highest priority against the remaining objectives. The other constraints are those discussed in the paper in previous sections, indeed. The proposed cascaded MPC for the HESS can provide an input control sequence which both satisfies the system constraints and minimizes the devices operating costs according to the considered control layer.

The following two subsections introduce the formulation of the HLC and the LLC, respectively.

#### HLC design

The mathematical models for the operations of the devices over the largest timescales, i.e., those addressed by the HLC, consist of the corresponding three states automata, including ON, OFF and STB states. The purpose of the HLC is to provide a strategy based on forecasts that are assumed unaffected by any kind of uncertainty in this paper. The controller handles hydrogen production for FCEVs, the local load tracking and the energy market participation. At the HLC,  $k$  indicates the discrete-time with resolution of 1 h.

*Sequential MPC scheme.* In order to formulate the MPC problem for HLC, the set

$$\mathcal{C}_k^{\text{HLC}} = \{ \mathbf{z}_e^{\text{HLC}}, \mathbf{z}_f^{\text{HLC}}, \mathbf{p}_e^{\text{HLC}}, \mathbf{p}_f^{\text{HLC}}, \mathbf{p}_{\text{avl}}^{\text{HLC}}, \mathbf{p}_g^{\text{HLC}}, \mathbf{v}_1^{\text{HLC}}, \sigma_k^{\text{HLC}}, \gamma_1^{\text{HLC}}, \gamma_2^{\text{HLC}} \}, \quad (40)$$

of the decision variable vectors at time-step  $k$  is defined, where  $\mathbf{p}_g^{\text{HLC}} = [P_g(k), \dots, P_g(k+T)]^\top$  is the decision vector of the grid power, and all the other vectors are defined in a similar way (not reported here for the sake of brevity). Therefore, the sequential optimization problem can be recast as

$$\begin{aligned} (J_H^{\text{HLC}})^* &= \min_{\mathcal{C}_{k|T}^{\text{HLC}}} J_H^{\text{HLC}}(k) \\ \text{s.t.} & \\ &\text{Discrete logical states (10) – (12),} \\ &\text{Mode transitions (16) – (17),} \\ &\text{Hydrogen dynamics (21),} \\ &\text{Grid constraints (23) – (25),} \\ &\text{Ramp up constraints (26),} \\ &\text{Power balancing equation (27),} \\ &\text{Physical constraints (28) – (29),} \\ &\mathbf{v}_1^{\text{HLC}} \in [0, 1]^3, \sigma_k^{\text{HLC}} \in [0, 1]^6, \\ &\gamma_1^{\text{HLC}}, \gamma_2^{\text{HLC}} \in \{0, 1\}^3, \\ &\delta_g^{\text{HLC}} \in \{0, 1\}, \end{aligned} \quad (41)$$

where  $\mathcal{C}_{k|T}^{\text{HLC}} = \mathcal{C}_k^{\text{HLC}}, \dots, \mathcal{C}_{k+T}^{\text{HLC}}$ , and then

**Table 3 – Optimization problem: comparison between the HLC and the LLC policies.**

	Optimization problem	
	High level control	Low level control
System modeling	3 states automata {OFF, STB, ON}	5 states automata{OFF, STB, ON, CLD, WRM}
Timescales	Larger timescales (24 h/1 h)	Shorter timescales (1 h/10 min)
Objectives	Hydrogen and load tracking + intraday market + operating	Load tracking + real-market + operating
Grid cost functions	$J_{grid}^{HLC}(k+j) = [-\pi_{sell}^{HLC}(k+j) z_{sell}^{HLC}(k+j)]T_s$	$J_{grid}^{LLC}(k+j) = [-\pi_{sell}^{LLC}(k+j) z_{sell}^{LLC}(k+j)]T_s$
Operating cost functions	$J^{HLC}(k+j) = \left( \frac{C^{rep}}{NH} + C^{OM} \right) \delta^{ON}(k+j)$ $+ C_{OFF}^{ON} \sigma_{OFF,i}^{ON}(k+j)$ $+ C_{ON}^{OFF} \sigma_{ON}^{OFF}(k+j)$ $+ C_{ON}^{STB} \sigma_{ON}^{STB}(k+j)$ $+ C_{STB}^{ON} \sigma_{STB}^{ON}(k+j)$ $+ C_{STB}^{OFF} \sigma_{STB}^{OFF}(k+j)$ $+ C_{OFF}^{STB} \sigma_{OFF}^{STB}(k+j)$ $+ [\pi^{sc}(k+j) p^{STB} \delta^{STB}(k+j)]T_s$	$J^{LLC}(k+j) = \left( \frac{C^{rep}}{NH} + C^{OM} \right) \delta^{ON}(k+j)$ $+ C_{ON}^{OFF} \sigma_{ON}^{OFF}(k+j)$ $+ C_{CLD}^{STB} \sigma_{CLD}^{STB}(k+j)$ $+ C_{STB}^{OFF} \sigma_{STB}^{OFF}(k+j)$ $+ [\pi^{sc}(k+j) p^{STB} \delta^{STB}(k+j)$ $+ \pi^{sc}(k+j) p^{CLD} \delta^{CLD}(k+j)$ $+ \pi^{sc}(k+j) p^{WRM} \delta^{WRM}(k+j)]T_s$ $+ \omega^P (z^{LLC}(k+j) - z^{HLC}(k))^2$ $+ \omega^H (H^{LLC}(k+j) - H^{HLC}(k))^2$
Load tracking cost functions	$J_d^{HLC}(k+j) = (p_{avl}^{HLC}(k+j) - p_{ref}^{HLC}(k+j))^2$	$J_d^{LLC}(k+j) = (p_{avl}^{LLC}(k+j) - p_{avl}^{HLC}(k+j))^2$
Hydrogen tracking cost functions	$J_H^{HLC}(k+j) = (H_{exc}^{HLC}(k+j) - H_{ref}^{HLC}(k+j))^2$	—

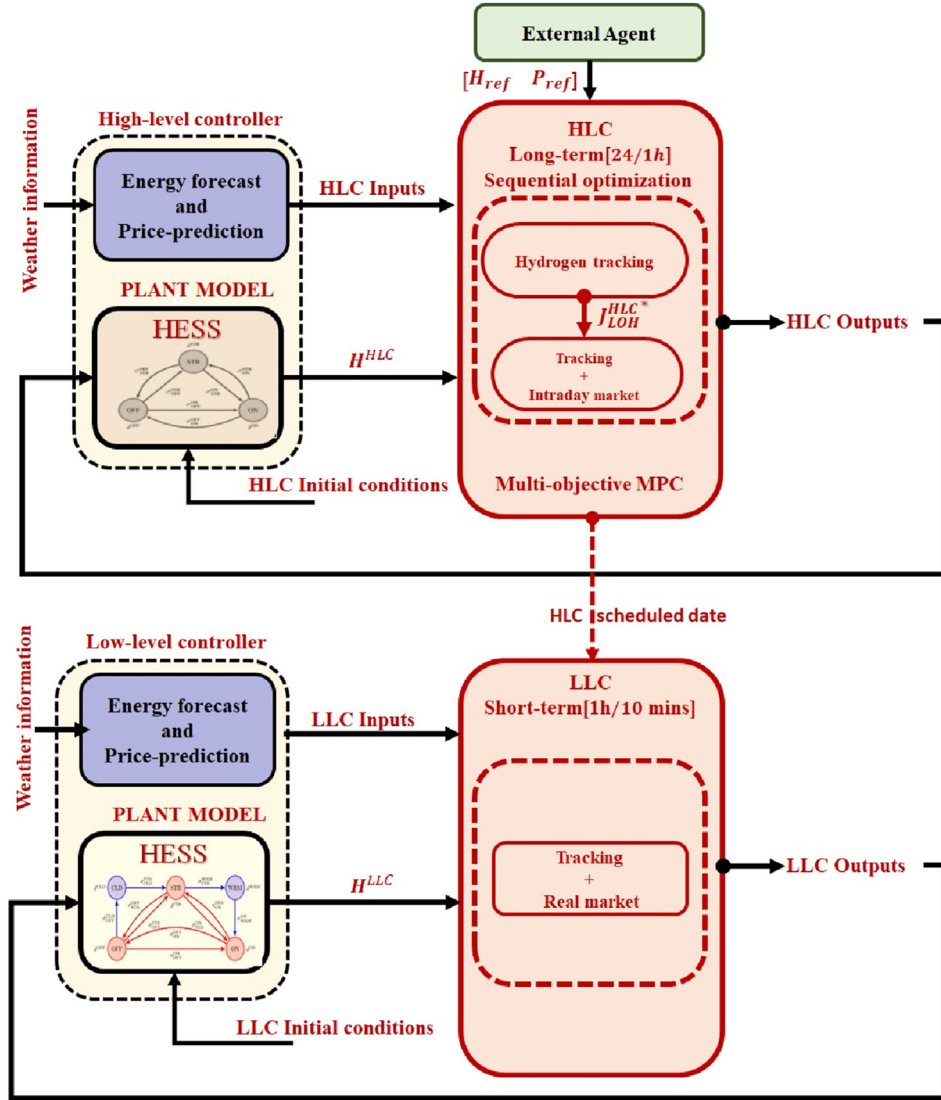


Fig. 3 – Multi-level cascaded MPC control block diagram.

$$\begin{aligned}
 (J_{FP}^{HLC})^* &= \min_{k/T} J_{FP}^{HLC}(k) \\
 \text{s.t.} \quad &\text{Similar to (41),} \\
 &J_H^{HLC}(k) \leq (J_H^{HLC})^*,
 \end{aligned} \tag{42}$$

where the cost function in (42) for the HLC is

$$J_{FP}^{HLC}(k) = \rho_l J_l^{HLC}(k) + \rho_g J_g^{HLC}(k) + \rho_e J_e^{HLC}(k) + \rho_f J_f^{HLC}(k) \tag{43}$$

with  $J_e^{HLC}(k)$  and  $J_f^{HLC}(k)$  two different instantiations of (34) for the electrolyzer and the fuel cell, respectively,  $\rho_l$ ,  $\rho_g$ ,  $\rho_e$  and  $\rho_f$  the weights of the load tracking, grid participation, electrolyzer and fuel cell operating cost functions, respectively, that can be tuned so as to achieve a desired prioritization among them. Such mixed-integer constraints can, indeed, be incorporated in an optimization problem handled by

general purpose solvers. For the reader's convenience, the references  $z_e^{HLC}$ ,  $z_f^{HLC}$ ,  $\delta^{HLC}$ ,  $p_e^{HLC}$ ,  $p_f^{HLC}$  and  $p_g^{HLC}$  scheduled by the HLC have the same meaning of the terms in (40), respectively.

#### LLC design

The LLC receives and tracks the references scheduled by the HLC, i.e.,  $z_e^{HLC}$ ,  $\delta^{HLC}$ ,  $p_e^{HLC}$ , and  $p_g^{HLC}$  in order to implement the HLC policy in real-time.

**MPC scheme for LLC.** This subsection introduces the LLC formulation for the participation of the electricity market to maximize the revenue generations and load tracking. In order to achieve the minimization problem in an MPC framework, the following set at time-step  $k$  is introduced

$$C_k^{LLC} = \{z_e^{LLC}, z_f^{LLC}, p_f^{LLC}, p_f^{LLC}, p_{avl}^{LLC}, p_g^{LLC}, v_1^{LLC}, \sigma_k^{LLC}, \gamma_1^{LLC}, \gamma_2^{LLC}\},$$

where the included elements are defined similarly to (40) with different values of  $k$  and  $T$ . Then, the MPC problem for the LLC is

$$\begin{aligned} (J_{FP}^{LLC})^* = \min_{C_{k|T}^{LLC}} & J_{FP}^{LLC}(k) \\ \text{s.t.} & \text{Discrete logical states (10) – (12),} \\ & \text{Mode transitions (16) – (17),} \\ & \text{Operation constraints (19),} \\ & \text{Hydrogen dynamics (21),} \\ & \text{Grid constraints (23) – (25),} \\ & \text{Ramp up constraints (26),} \\ & \text{Power balancing equation (27),} \\ & \text{Physical constraints (28) – (29),} \\ & v_1^{LLC} \in [0, 1]^5, \sigma_k^{LLC} \in [0, 1]^{20}, \\ & \gamma_1^{LLC}, \gamma_2^{LLC} \in \{0, 1\}^5, \end{aligned} \quad (44)$$

where  $C_{k|T}^{LLC} = C_k^{LLC}, \dots, C_{k+T}^{LLC}$ , and the cost function

$$J_{FP}^{LLC}(k) = \rho_g J_g^{LLC}(k) + \rho_l J_l^{LLC}(k) + \rho_e J_e^{LLC}(k) + \rho_f J_f^{LLC}(k) \quad (45)$$

gathers the operating costs  $J_i^{LLC}$ ,  $i \in \{e, f\}$ , of the devices, and the tracking cost  $J_g^{LLC}$  of the power injected into the grid against the grid operator reference, and  $\rho_g$ ,  $\rho_l$ ,  $\rho_e$ , and  $\rho_f$  are weights tuned to achieve an appropriate blending of the corresponding cost functions.

### Integrated multi-level MPC algorithm

The multi-objective MPC control of the system under investigation according to the fuel production use case is reported in Algorithm 1, for the sake of completeness. As explained in

the previous section, the two optimization problems (41) and (42) are solved at the HLC and the optimization problem (44) is solved at the LLC. In Algorithm 1,  $N^h$  and  $N^m$  refer to the two simulation horizons for the HLC and the LLC, respectively. Moreover, the problems are defined w.r.t. different sampling times and, therefore, different discrete time-steps;  $h$  and  $m$  indicate the time-steps used for the HLC and the LLC, respectively. In order to improve the readability, the optimal control input sequence for the first optimization problem is given by  $C_{h|T}^* = \{C_h^*, C_{h+1}^*, \dots, C_{h+T}^*\}$ , where  $C_{h+j}^*$  is the optimal value of  $C_{k|T}^{HLC}$  at the generic time-step  $h+j$ . Then, only the first optimal control input is applied to the system. The optimal control input sequence used by the LLC is, instead, collected in the set  $C_{m|T}^*$  which is defined similarly to  $C_{h|T}^*$ .

#### Algorithm 1: MPC algorithm for the fuel production.

**Input** : State  $H^s$  at time instant  $k$  and  $H_0^s$  initial condition for the state

**Output**: Receding horizon control input  $u(k)$

**begin**

Load parameters;

$N^h \leftarrow$  simulation horizon for the HLC;

$N^m \leftarrow$  simulation horizon for the LLC;

$h \leftarrow 1$ ;

$m \leftarrow 1$ ;

$H^{HLC}(h) \leftarrow H_0^{HLC}$ ;

$H^{LLC}(m) \leftarrow H_0^{LLC}$ ;

**for**  $h \leftarrow 1$  **to**  $N^h$  **do**

$C_{h|T}^* \leftarrow$  solve problem (41);

$C_h^* \leftarrow C_{h|T}^*$ ;  $\triangleright$  Apply the first element

$\mathcal{H}_{h|T}^* \leftarrow$  solve problem (42);

$\mathcal{H}_h^* \leftarrow \mathcal{H}_{h|T}^*$ ;  $\triangleright$  Apply the first element

$H^{HLC}(h+1) \leftarrow$  **update** (21);

**for**  $m \leftarrow 1$  **to**  $N^m$  **do**

$C_{m|T}^* \leftarrow$  solve problem (44);

$C_m^* \leftarrow C_{m|T}^*$ ;  $\triangleright$  Apply the first element

$H^{LLC}(m+1) \leftarrow$  **update** (21);

$m \leftarrow m+1$ ;

$h \leftarrow h+1$ ;

**Table 4 – Devices parameters.**

Electrolyzer parameters	
$C_e^{STB} = 0.0042 \text{ €}$	$NH_e = 40,000 \text{ h}$
$C_e^{ON} = 0.123 \text{ €}$	$C_e^{OFF} = 0.0062 \text{ €}$
$\eta_e = 0.019 \text{ kg/kWh}$	$C_e^{OM} = 0.002 \text{ €/h}$
$Capex_e = 1300 \text{ €/kW}$	$p_e^{max} = 3000 \text{ kW}$
$p_e^{min} = 300 \text{ kW}$	$p_e^{STB} = 1 \text{ kW}$
$NY_e = 8000 \text{ h}$	$p_e^{CLD} = 1 \text{ kW}$
$p_e^{WRM} = 1 \text{ kW}$	$N_e^{max} = 5000 \text{ cycles}$
Fuel cell parameters	
$C_f^{STB} = 0.003 \text{ €}$	$NH_f = 40,000 \text{ h}$
$C_f^{ON} = 0.01 \text{ €}$	$C_f^{OFF} = 0.005 \text{ €}$
$\eta_f = 17 \text{ kWh/kg}$	$C_f^{OM} = 0.01/\text{h}$
$Capex_f = 1500 \text{ €/kW}$	$p_f^{max} = 120 \text{ kW}$
$p_f^{min} = 12 \text{ kW}$	$p_f^{STB} = 1 \text{ kW}$
$NY_f = 8000 \text{ h}$	$p_f^{CLD} = 1 \text{ kW}$
$p_f^{WRM} = 1 \text{ kW}$	$N_f^{max} = 5000 \text{ cycles}$
Tank parameters	
Volume = 10 kg	Pressure = 30 bar

### Computation details of the integrated algorithm

The analysis and the experimental validation have been performed through simulations over a  $T = 24 \text{ h}$  and  $T = 1 \text{ h}$  scheduled horizon with  $T_s = 1 \text{ h}$  and  $T_s = 10 \text{ min}$  sample times according to the considered control layer.

Table 4 reports the devices parameters involved in the integrated algorithm. In the STB state degradation of the devices is mitigated since they are kept warm. Consequently, the cost of switching from STB to ON is lower among the other transitions, such as OFF to ON and from ON to OFF. However, when the devices are in STB, a constant  $p^{STB}$  power is consumed. Moreover, the stack replacement costs, denoted as  $C^{rep}$ , are set as

$$C^{rep} = 0.27 \times Capex, \quad (46)$$

corresponding to  $\frac{2}{3}$  of the 40% of Capex.



The integrated algorithm is briefly represented in Fig. 3. The implementation and simulation of the proposed controller have been performed using MATLAB/YALMIP/GUROBI on a PC with an Intel Core (TM) i7-7700HQ 2.8 GHz and a RAM capacity of 16 GB. The time required for solving the optimization problem on such a PC is equal to 60 s. In order to properly weigh the different terms in the cost functions suitable weights have been chosen through a series of simulations. These tests will be repeated once the construction of the plant will be completed.

## Results analysis and discussion

Numerical simulations are provided to validate the proposed strategy in this section. Although the simulations are preliminary to the integration of the proposed controller in the system under investigation, the data of the HAEOLUS plant have been used where possible. Since several scenarios can occur, the simulations include many power production and consumption profiles. The results show that the controller reaches the control goal and, at the same time, allows the satisfaction of the constraints. We wish to emphasize here that the proposed dynamic models and control strategy can also be generalized for other case studies, i.e., it is not specific to the HAEOLUS plant only. Indeed, the model and control based on the multi-level MPC scheme can be used for the general case of hydrogen storage plants.

Via hydrogen storage utilization, the renewable wind availability, and a possible connection to the utility grid, the solver satisfies the hydrogen demand from the external consumers with the highest priority, and simultaneously with second priority satisfies the electric reference  $P_{ref}(k)$  with the system available power  $P_{avl}(k)$ .

The control algorithm has been analyzed via a series of simulations to capture the effects of the terms included in the cost functions by their activation and deactivation. In particular, when the switching costs and the degradation costs are accounted in the optimization, our algorithm shows to reduce the operating costs by 5% with respect to the case when they are neglected (this is the case of the revised literature). For similar wind and load profiles, this results in more than 300 commutations saving per year. Further benefits of our strategy in conveniently exploiting the stand-by, cold and warm states can be observed for the case of fast power imbalances or grid islanded mode. This fast response feature is not currently present in the literature.

Simulations under a stressing plant scenario over a 24 h horizon have been performed to present the efficacy of the integrated algorithm for fuel production use cases. It is important to highlight here that the contribution of the implemented algorithm is to control the HESS so as to enable the wind farm to operate conforming to the fuel production use cases [7] as per the project goals [59].

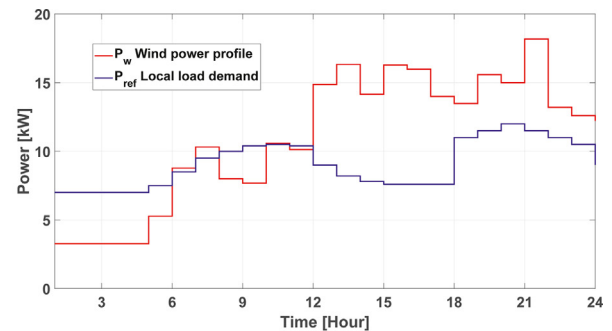
In order to validate the efficacy of the multi-layer MPC implemented in this research study, two scenarios have been achieved. In the first scenario, equal weight choices for tracking the local load demand and participation in the energy market have been assigned. In the second scenario, the weights are changed: one sets greater than the other, and vice

versa. In both scenarios, the fulfillment of the hydrogen demand has the highest priority.

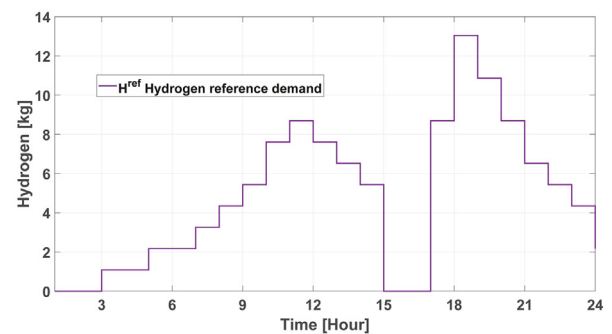
### Hydrogen demand satisfaction

Fig. 4 shows several profiles considered in the numerical analysis of the multi-level MPC. In particular, Fig. 4a reports the power generated by the wind farm and the electric load requested by users, respectively. Fig. 4b reports the hydrogen reference demand as provided by the HLC, while Fig. 4c shows the energy market price profile considered in the control implementation. In turn, the energy equality constraint (27) will be enforced.

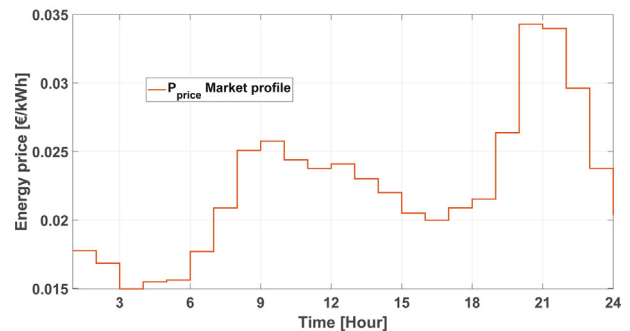
Fig. 5 explains the working of the HLC. In particular, as shown in Fig. 5a, the final exchange of hydrogen exactly matches what was requested by hydrogen consumers in all 24 h of the day and also the system available power exactly matches the requested load, as shown in Fig. 5b. Moreover, the hydrogen level is within the upper and lower bounds of the HESS unit as shown in Fig. 5c.



(a) Wind and local load power profiles.



(b) Hydrogen reference profile.



(c) Market price profile.

Fig. 4 – Data profiles.

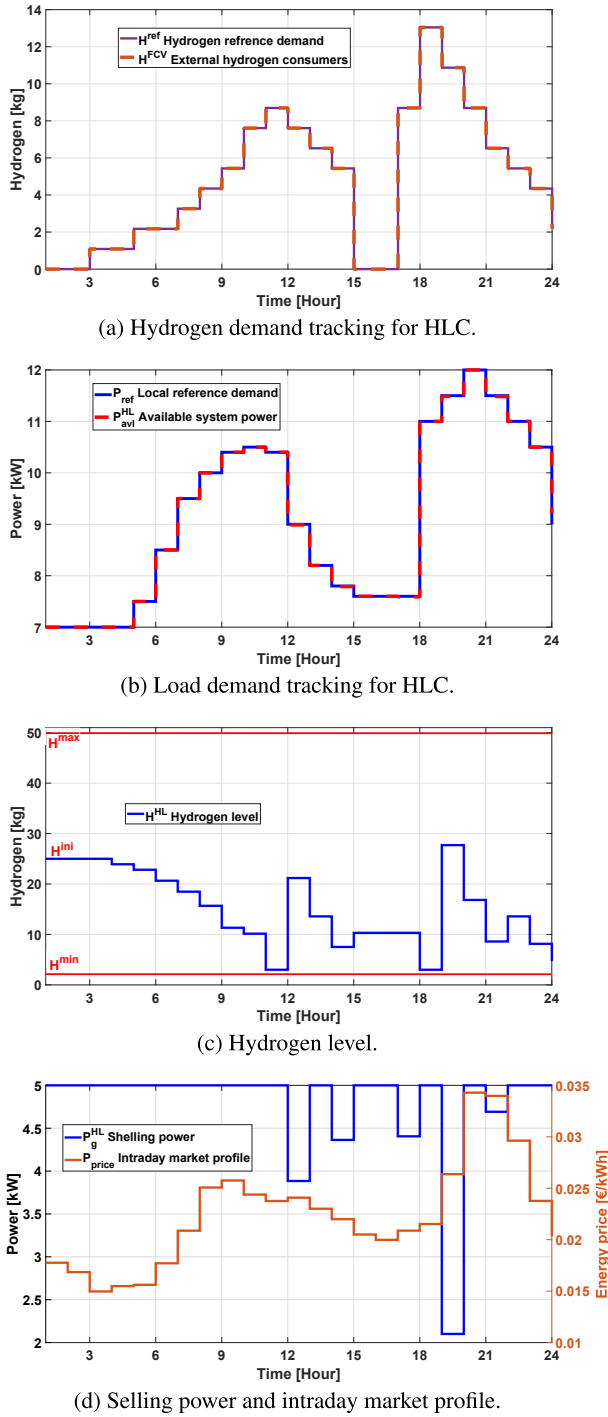


Fig. 5 – HLC controller.

Regarding the energy market participation, based on a day long-term control horizon, at each time-step  $k$ , the controller is designed to take decisions of the energy selling with the proper modeling and switching of the logical variable  $\delta^d(k)$  from 0 to 1, as Fig. 5d shows. Interestingly, from 19 to 20 h, the controller decides not to sell electricity to the market even though the prices are increasing. However, thanks to this decision, the load demand is satisfied, and the hydrogen level

in the tank is also able to increase so as to comply with future operations. This is compatible with equal weight choices for tracking the local load demand and participation in the energy market and also shows the kind of nontrivial decisions that the developed algorithm can address. Note that the controller not only tracks successfully the user requested load, but the contractual loads have also been supplied.

Fig. 6 shows the working of the LLC policy, i.e., that which is implemented by the real-time algorithm. The reason for introducing a double reference gives a degree of freedom in the controller, which allows correcting the deficit scenario with an exceeding scenario compared to the forecast carried out at the HLC. The use of multi-level MPC allows one to manage from the long-term control horizon given at the HLC linked to the real-time operational scenario of this study. The purpose of the LLC is to track the references set by the HLC to match generation and load demands. The LLC executes every 10 min with a scheduled horizon of 1 h discretized in periods of 60 min.

Specifically, Fig. 6a shows that the available power exactly matches with what was requested in terms of user load

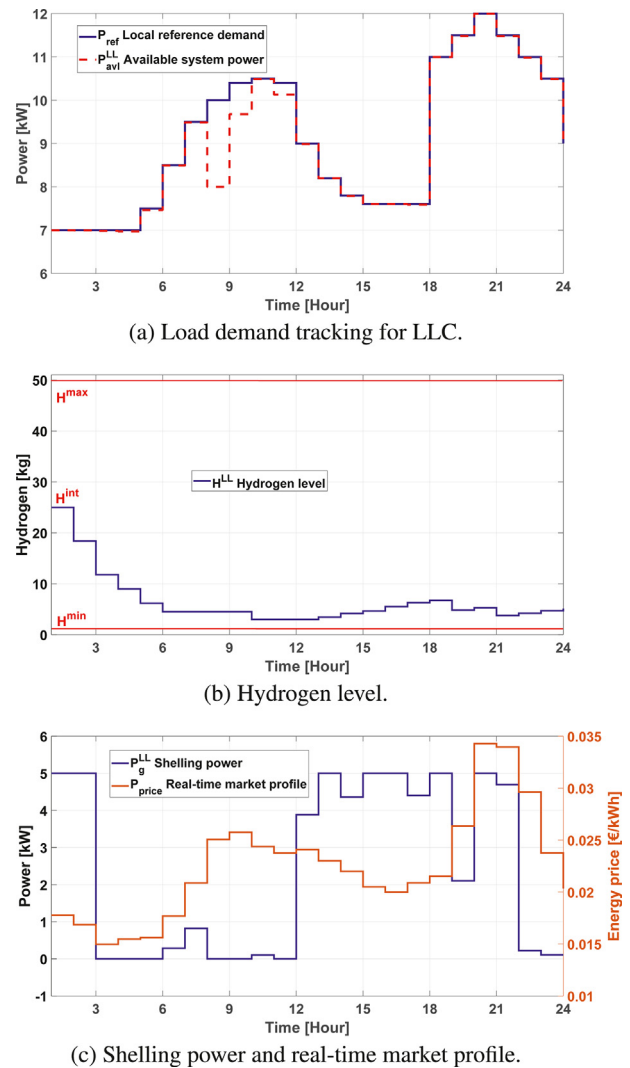
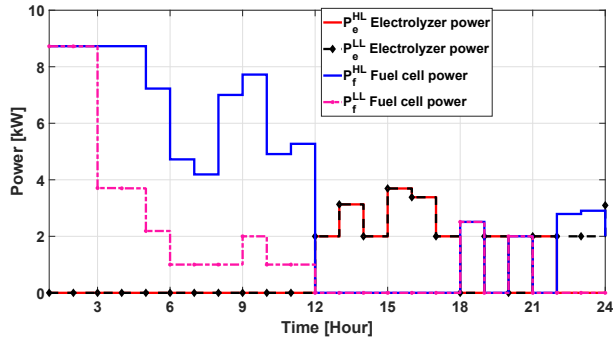
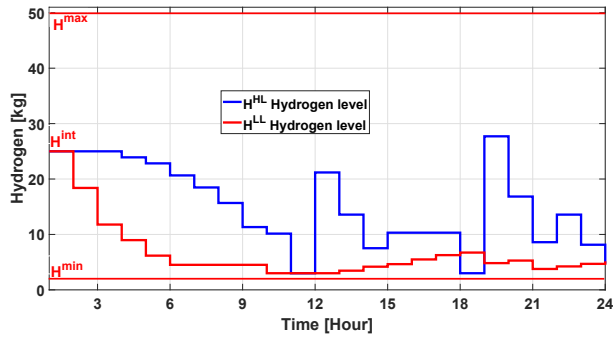
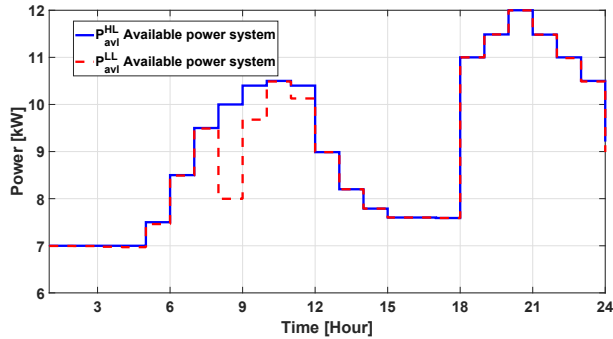


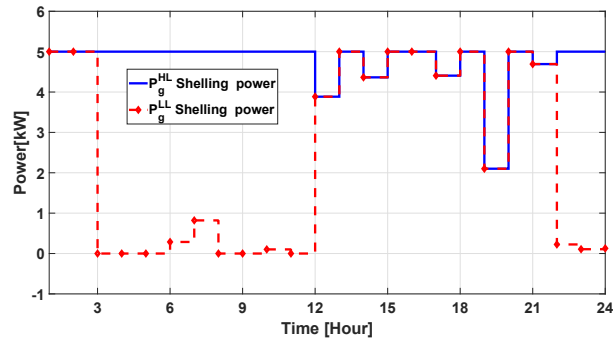
Fig. 6 – LLC controller.



(a) Control response of the devices.

(b) Control response of hydrogen storage  $H$ .

(c) Local Load demand tracking.



(d) Control response of utility grid.

**Fig. 7 – Control response of the system for multi-layer.**

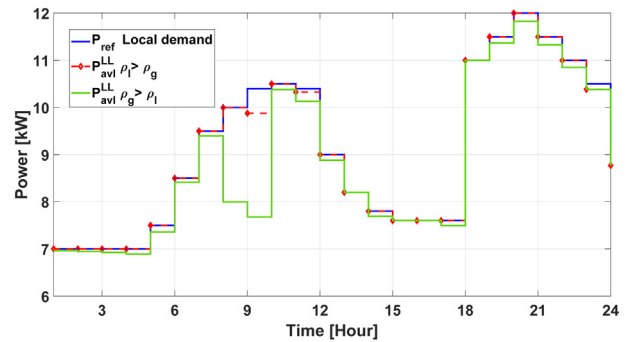
demand achieved by the HLC. Fig. 6b shows the evolution of the hydrogen level in the tank. In particular, this level also takes into account the hydrogen provided to the electric vehicles, the load demand tracking and the energy market participation. The implemented strategy is such that, sometimes, the load

demand is not met, and the controller decides not to sell electricity to the market, as shown in Fig. 6c. However, this is in compliance with the objective of the fuel production use case where other additional objectives than the provision of hydrogen to FCEVs can be considered as optional features and not strict requirements. Moreover, even if the same wind generation, load demand and market price profiles for the HLC and the LLC have been assumed, the two policies are very different, especially in the market participation. This difference can be explained by the fact that the operating cost functions of the HLC and the LLC are different since, e.g., at the HLC three states automata are used while at the LLC five states automata are used in order to consider also cold and warm starts, and not all the transitions are enabled for five states automata.

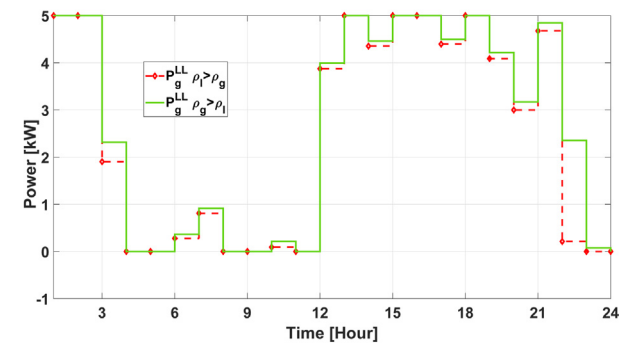
A comparison between the HLC and the LLC policies and evaluations of the relevant parameters are provided in Fig. 7. Fig. 7a shows the power of the electrolyzer and the fuel cell for both the HLC and the LLC, respectively. It can be seen that the LLC successfully tracks the references set by the HL-MPC. Similarly, the hydrogen level in the tank and the available system power for both the HLC and the LLC are detailed in Fig. 7b and c, respectively. Finally, the power selling to the grid as one of the objectives of the control strategy for both levels is shown in Fig. 7d. The LLC successfully participates in the energy market as per the timescale.

#### Controller behavior for different weights

This section provides a sensitive analysis of how the weight factors  $\rho_g$  and  $\rho_l$  affect system operation. The same data scenario, in terms of local demand, wind power and market profiles, is used to give an accurate comparison.



(a) Load demand tracking.



(b) Control response of utility grid.

**Fig. 8 – Controller behavior for different weights.**

For both scenarios  $\rho_l > \rho_g$  and  $\rho_g > \rho_l$ ,<sup>1</sup> the load demand tracking and the interaction with the utility grid are shown in Fig. 8a and Fig. 8b, respectively. Based on the weight factors, the numerical solver prioritizes either to participate in the energy market to maximize revenues (if  $\rho_g > \rho_l$ ) or to meet the load demand with respect to selling energy to the grid (if  $\rho_l > \rho_g$ ). In the proposed scenario, for  $\rho_g > \rho_l$ , during the hours 8–10 the available power  $P_{avl}(k)$  decreases, thus resulting in non-compliance with the local load demand. Conversely, for  $\rho_l > \rho_g$ , during the hours 8–10 the available power  $P_{avl}(k)$  increases by successfully tracking the load profile, and then selling the remaining energy to the grid.

## Conclusions

In this research study, models used in a controller based on the MPC framework for HESS integrated with a wind farm have been proposed. The dynamic models of both the electrolyzer and the fuel cell map their operating modes with corresponding discrete logical states, together with the continuous dynamics concerning the hydrogen production/consumption.

The novel contribution of the proposed MPC control lies within the consideration of the expensive hydrogen production/consumption devices degradations that occur at each time-step  $k$  due to the switching states between the different operating modes. This switching, if not optimized, would decrease the life cycles and efficiencies of the devices. Furthermore, the system operational and maintenance costs have also been accounted for. MLD models have been adopted to capture the correct behavior of the plant. In particular, the proposed MPC is a multi-layer scheme, in which at the first layer the hydrogen demand for the FCEVs is satisfied, and at the second layer the surpluses of the hydrogen available in the tank are re-electrified through the fuel cell for meeting local and contractual loads. Moreover, the correct working of the devices and their operating modes have been verified numerically.

The MPC proposed in this paper will be deployed in the under construction HAEOLUS plant. Indeed, this research work has been designed as part of the EU2020 funded project HAEOLUS, where the HESS will be coupled with the wind farm in North Norway.

Summarizing, the proposed study contributes to the literature with:

1. The implementation of a novel wind-hydrogen model for a multi-level controller based on the MLD framework that takes into account the different degradation issues of the HESS;
2. The implementation of a two-stage MPCs which takes into account the external hydrogen consumer profiles at first stage, and handles the frequently varying electric loads at second stage;

<sup>1</sup>  $\rho_l$  and  $\rho_g$  are typically the weight factors of the load tracking and grid participation cost functions imposed to the proposed controller, which in our case are equal to  $\rho_l = 12e^4$  and  $\rho_g = 4e^2$ , respectively.

3. The comprehensive addressing of many practical aspects that can prevent the penetration of wind farms into the main grid due to a lack of profitability of the initiative in case they are not properly managed.

Future works will investigate hydrogen production for commercialization purposes (see the IEA-HIA Task 24 final report).

## Declaration of competing interest

The authors declare that they have no known competing financial interests or personal relationships that could have appeared to influence the work reported in this paper.

## Appendix A. Supplementary data

Supplementary data to this article can be found online at <https://doi.org/10.1016/j.ijhydene.2022.07.136>.

## REFERENCES

- [1] Sharma S, Ghoshal SK. Hydrogen the future transportation fuel: from production to applications. *Renew Sustain Energy Rev* 2015;43:1151–8.
- [2] Hosseini SE. The US hydrogen fuel industry today and future. *Future Energy Mar.* 2022;1(1).
- [3] D.-G. for Maritime Affairs, D.-G. f. M. Fisheries (European Commission), J. R. C. E. C. Transport (European Commission). *State of the art on alternative fuels transport systems in the European Union.* 2015.
- [4] Sulaiman N, Hannan M, Mohamed A, Ker PJ, Majlan E, Daud WW. Optimization of energy management system for fuel-cell hybrid electric vehicles: issues and recommendations. *Appl Energy* 2018;228:2061–79.
- [5] Li Y, Taghizadeh-Hesary F. The economic feasibility of green hydrogen and fuel cell electric vehicles for road transport in China. *Energy Policy* 2022;160(C).
- [6] Piraino F, Fragiaco P. A multi-method control strategy for numerically testing a fuel cell-battery-supercapacitor tramway. *Energy Convers Manag* 2020;225:113481.
- [7] Hoskin A, Pedersen AS, et al. IEA-HIA Task 24 wind energy & hydrogen integration. <http://ieahydrogen.org/PUBLICATIONS-REPORTS-PRESENTATIONS/Final-Reports-V2.aspx>; 2007–2011.
- [8] Bemporad A, Morari M. Control of systems integrating logic, dynamics, and constraints. *Automatica* 1999;35(3):407–27.
- [9] Abdelghany MB, Shehzad MF, Liuzza D, Mariani V, Glielmo L. Optimal operations for hydrogen-based energy storage systems in wind farms via model predictive control. *Int J Hydrogen Energy* 2021;46(57):29297–313. <http://dx.doi.org/10.1016/j.ijhydene.2021.01.064>.
- [10] Abdelghany MB, Faisal Shehzad M, Liuzza D, Mariani V, Glielmo L. Modeling and optimal control of a hydrogen storage system for wind farm output power smoothing. In: 2020 59th IEEE conference on decision and control (CDC); 2020. p. 49–54.
- [11] Kakoulaki G, Kougias I, Taylor N, Dolci F, Moya J, Jäger-Waldau A. Green hydrogen in Europe—a regional assessment: substituting existing production with electrolysis powered by renewables. *Energy Convers Manag* 2021;228:113649.






- [12] García-Olivares A, Solé J, Osychenko O. Transportation in a 100% renewable energy system. *Energy Convers Manag* 2018;158:266–85.
- [13] Eberle U, Müller B, Von Helmolt R. Fuel cell electric vehicles and hydrogen infrastructure: status 2012. *Energy Environ Sci* 2012;5(10):8780–98.
- [14] Mohsin M, Rasheed A, Saidur R. Economic viability and production capacity of wind generated renewable hydrogen. *Int J Hydrogen Energy* 2018;43(5):2621–30.
- [15] Sinigaglia T, Lewiski F, Martins MES, Siluk JCM. Production, storage, fuel stations of hydrogen and its utilization in automotive applications-a review. *Int J Hydrogen Energy* 2017;42(39):24597–611.
- [16] Garcia-Torres F, Vilaplana DG, Bordons C, Roncero-Sanchez P, Ridao MA. Optimal management of microgrids with external agents including battery/fuel cell electric vehicles. *IEEE Trans Smart Grid* 2018;10(4):4299–308.
- [17] Correa G, Muñoz P, Falaguerra T, Rodriguez C. Performance comparison of conventional, hybrid, hydrogen and electric urban buses using well to wheel analysis. *Energy* 2017;141:537–49.
- [18] Lozanovski A, Whitehouse N, Ko N, Whitehouse S. Sustainability assessment of fuel cell buses in public transport. *Sustainability* 2018;10(5):1480.
- [19] New bus refuelling for European hydrogen bus depots. <http://newbusfuel.eu/>; January 2021.
- [20] Valverde L, Bordons C, Rosa F. Power management using model predictive control in a hydrogen-based microgrid. In: *IECON 38th conference on industrial electronics society*. IEEE; 2012. p. 5669–76.
- [21] Petrollese M, Valverde L, Cocco D, Cau G, Guerra J. Real-time integration of optimal generation scheduling with MPC for the energy management of a renewable hydrogen-based microgrid. *Appl Energy* 2016;166:96–106.
- [22] Hosseini SE, Wahid MA. Hydrogen production from renewable and sustainable energy resources: promising green energy carrier for clean development. *Renew Sustain Energy Rev* 2016;57:850–66.
- [23] Trifkovic M, Sheikhzadeh M, Nigim K, Daoutidis P. Hierarchical control of a renewable hybrid energy system. In: *IEEE 51st conference on decision and control (CDC)*. IEEE; 2012. p. 6376–81.
- [24] Serna Á, Yahyaoui I, Normey-Rico JE, de Prada C, Tadeo F. Predictive control for hydrogen production by electrolysis in an offshore platform using renewable energies. *Int J Hydrogen Energy* 2017;42(17):12865–76.
- [25] De Angelis F, Boaro M, Fuselli D, Squartini S, Piazza F, Wei Q. Optimal home energy management under dynamic electrical and thermal constraints. *IEEE Trans Ind Inf* 2013;9(3):1518–27.
- [26] Yang P, Nehorai A. Joint optimization of hybrid energy storage and generation capacity with renewable energy. *IEEE Trans Smart Grid* 2014;5(4):1566–74.
- [27] Malysz P, Sirouspour S, Emadi A. An optimal energy storage control strategy for grid-connected microgrids. *IEEE Trans Smart Grid* 2014;5(4):1785–96.
- [28] Pivetta D, Dall'Armi C, Taccani R. Multi-objective optimization of hybrid PEMFC/li-ion battery propulsion systems for small and medium size ferries. *Int J Hydrogen Energy* 2021;46(72):35949–60.
- [29] Greenwell W, Vahidi A. Predictive control of voltage and current in a fuel cell-ultracapacitor hybrid. *IEEE Trans Ind Electron* 2009;57(6):1954–63.
- [30] Torreglosa JP, García P, Fernández LM, Jurado F. Energy dispatching based on predictive controller of an off-grid wind turbine/photovoltaic/hydrogen/battery hybrid system. *Renew Energy* 2015;74:326–36.
- [31] Maghami MR, Hassani R, Gomes C, Hizam H, Othman ML, Behmanesh M. Hybrid energy management with respect to a hydrogen energy system and demand response. *Int J Hydrogen Energy* 2020;45(3):1499–509.
- [32] Wang G, Huang F, Yu Y, Wen S, Tu Z. Degradation behavior of a proton exchange membrane fuel cell stack under dynamic cycles between idling and rated condition. *Int J Hydrogen Energy* 2018;43(9):4471–81.
- [33] Garcia-Torres F, Bordons C, Tobajas J, Marquez JJ, Garrido-Zafra J, Moreno-Munoz A. Optimal schedule for networked microgrids under deregulated power market environment using model predictive control. *IEEE Trans Smart Grid* 2020.
- [34] Garcia-Torres F, Valverde L, Bordons C. Optimal load sharing of hydrogen-based microgrids with hybrid storage using model-predictive control. *IEEE Trans Ind Electron* 2016;63(8):4919–28.
- [35] Cecilia A, Carroquino J, Roda V, Costa-Castelló R, Barreras F. Optimal energy management in a standalone microgrid, with photovoltaic generation, short-term storage, and hydrogen production. *Energies* 2020;13(6):1454.
- [36] Kumar K, Alam M, Dutta V. Energy management strategy for integration of fuel cell-electrolyzer technologies in microgrid. *Int J Hydrogen Energy* 2021;46(68):33738–55.
- [37] Hu X, Jiang J, Egardt B, Cao D. Advanced power-source integration in hybrid electric vehicles: multicriteria optimization approach. *IEEE Trans Ind Electron* 2015;62(12):7847–58.
- [38] Hu X, Murgovski N, Johannesson LM, Egardt B. Optimal dimensioning and power management of a fuel cell/battery hybrid bus via convex programming. *IEEE/ASME Trans Mechatron* 2014;20(1):457–68.
- [39] Valverde L, Bordons C, Rosa F. Integration of fuel cell technologies in renewable-energy-based microgrids optimizing operational costs and durability. *IEEE Trans Ind Electron* 2015;63(1):167–77.
- [40] González-Rivera E, Sarrias-Mena R, García-Triviño P, Fernández-Ramírez LM. Predictive energy management for a wind turbine with hybrid energy storage system. *Int J Energy Res* 2020;44(3):2316–31.
- [41] Sellali M, Ravey A, Betka A, Kouzou A, Benbouzid M, Djerdir A, Kennel R, Abdelrahman M. Multi-objective optimization-based health-conscious predictive energy management strategy for fuel cell hybrid electric vehicles. *Energies* 2022;15(4):1318.
- [42] Zhang Y, Meng F, Wang R, Kazemtabrizi B, Shi J. Uncertainty-resistant stochastic MPC approach for optimal operation of CHP microgrid. *Energy* 2019;179:1265–78.
- [43] Pippia T, Sijs J, De Schutter B. A single-level rule-based model predictive control approach for energy management of grid-connected microgrids. *IEEE Trans Control Syst Technol* 2020;28(6):2364–76.
- [44] Bonthu RK, Aguilera RP, Pham H, Phung MD, Ha QP. In: *Energy cost optimization in microgrids using model predictive control and mixed integer linear programming*. ICIT; 2019. p. 1113–8.
- [45] Jiang Q, Xue M, Geng G. Energy management of microgrid in grid-connected and stand-alone modes. *IEEE Trans Power Syst* 2013;28(3):3380–9.
- [46] Ruiming F. Multi-objective optimized operation of integrated energy system with hydrogen storage. *Int J Hydrogen Energy* 2019;44(56):29409–17.
- [47] Martinez JS, Mulot J, Harel F, Hissel D, Pera M-C, John RI, Amiet M. Experimental validation of a type-2 fuzzy logic controller for energy management in hybrid electrical vehicles. *Eng Appl Artif Intell* 2013;26(7):1772–9.
- [48] Hemi H, Ghouili J, Cheriti A. A real time fuzzy logic power management strategy for a fuel cell vehicle. *Energy Convers Manag* 2014;80:63–70.

- [49] Enang W, Bannister C. Modelling and control of hybrid electric vehicles (a comprehensive review). *Renew Sustain Energy Rev* 2017;74:1210–39.
- [50] Erdinc O, Vural B, Uzunoglu M. A wavelet-fuzzy logic based energy management strategy for a fuel cell/battery/ultra-capacitor hybrid vehicular power system. *J Power Sources* 2009;194(1):369–80.
- [51] Geng C, Jin X, Zhang X. Simulation research on a novel control strategy for fuel cell extended-range vehicles. *Int J Hydrogen Energy* 2019;44(1):408–20.
- [52] Merabet A, Al-Durra A, El-Saadany EF. Energy management system for optimal cost and storage utilization of renewable hybrid energy microgrid. *Energy Convers Manag* 2022;252:115116.
- [53] Xu C, Ke Y, Li Y, Chu H, Wu Y. Data-driven configuration optimization of an off-grid wind/PV/hydrogen system based on modified NSGA-II and CRITIC-TOPSIS. *Energy Convers Manag* 2020;215:112892.
- [54] AlYahya S, Irfan MA. The techno-economic potential of Saudi Arabia's solar industry. *Renew Sustain Energy Rev* 2016;55:697–702.
- [55] Gökçek M, Kale C. Techno-economical evaluation of a hydrogen refuelling station powered by wind-PV hybrid power system: a case study for İzmir-Çeşme. *Int J Hydrogen Energy* 2018;43(23):10615–25. the 2nd International Hydrogen Technologies Congress (IHTEC-2017).
- [56] Coppitters D, De Paepe W, Contino F. Robust design optimization and stochastic performance analysis of a grid-connected photovoltaic system with battery storage and hydrogen storage. *Energy* 2020;213:118798.
- [57] Shehzad MF, Abdelghany MB, Liuzza D, Glielmo L. Modeling of a hydrogen storage wind plant for model predictive control management strategies. In: 2019 18th European control conference (ECC); 2019. p. 1896–901.
- [58] Shehzad MF, Abdelghany MB, Liuzza D, Mariani V, Glielmo L. Mixed logic dynamic models for MPC control of wind farm hydrogen-based storage systems. *Inventions* 2019;4(4):57.
- [59] Hydrogen-aeolic energy with optimized electrolyzers upstream of substation project. <http://www.haeolus.eu/>; May 2022.



## Article

# Operating Hydrogen-Based Energy Storage Systems in Wind Farms for Smooth Power Injection: A Penalty Fees Aware Model Predictive Control

Valerio Mariani <sup>1,\*</sup> , Federico Zenith <sup>2</sup>  and Luigi Glielmo <sup>1</sup> <sup>1</sup> DING—Dipartimento di Ingegneria, Università del Sannio, Piazza Roma 21, 82100 Benevento, Italy<sup>2</sup> SINTEF Mathematics and Cybernetics, Klæbuveien 153, 7031 Trondheim, Norway

\* Correspondence: vmariani@unisannio.it

**Abstract:** Smooth power injection is one of the possible services that modern wind farms could provide in the not-so-far future, for which energy storage is required. Indeed, this is one among the three possible operations identified by the International Energy Agency (IEA)-Hydrogen Implementing Agreement (HIA) within the Task 24 final report, that may promote their integration into the main grid, in particular when paired to hydrogen-based energy storages. In general, energy storage can mitigate the inherent unpredictability of wind generation, providing that they are deployed with appropriate control algorithms. On the contrary, in the case of no storage, wind farm operations would be strongly affected, as well as their economic performances since the penalty fees wind farm owners/operators incur in case of mismatches between the contracted power and that actually delivered. This paper proposes a Model Predictive Control (MPC) algorithm that operates a Hydrogen-based Energy Storage System (HESS), consisting of one electrolyzer, one fuel cell and one tank, paired to a wind farm committed to smooth power injection into the grid. The MPC relies on Mixed-Logic Dynamic (MLD) models of the electrolyzer and the fuel cell in order to leverage their advanced features and handles appropriate cost functions in order to account for the operating costs, the potential value of hydrogen as a fuel and the penalty fee mechanism that may negatively affect the expected profits generated by the injection of smooth power. Numerical simulations are conducted by considering wind generation profiles from a real wind farm in the center-south of Italy and spot prices according to the corresponding market zone. The results show the impact of each cost term on the performances of the controller and how they can be effectively combined in order to achieve some reasonable trade-off. In particular, it is highlighted that a static choice of the corresponding weights can lead to not very effective handling of the effects given by the combination of the system conditions with the various exogenous, while a dynamic choice may suit the purpose instead. Moreover, the simulations show that the developed models and the set-up mathematical program can be fruitfully leveraged for inferring indications on the devices' sizing.

**Keywords:** hydrogen-based energy storage systems; wind farms; power smoothing; optimal operations; model predictive control; mixed-logic dynamic modeling



**Citation:** Mariani, V.; Zenith, F.; Glielmo, L. Operating Hydrogen-Based Energy Storage Systems in Wind Farms for Smooth Power Injection: A Penalty Fees Aware Model Predictive Control. *Energies* **2022**, *15*, 6307. <https://doi.org/10.3390/en15176307>

Academic Editors: Pierluigi Siano and Mahmoud A. Mossa

Received: 21 July 2022

Accepted: 24 August 2022

Published: 29 August 2022

**Publisher's Note:** MDPI stays neutral with regard to jurisdictional claims in published maps and institutional affiliations.



**Copyright:** © 2022 by the authors. Licensee MDPI, Basel, Switzerland. This article is an open access article distributed under the terms and conditions of the Creative Commons Attribution (CC BY) license (<https://creativecommons.org/licenses/by/4.0/>).

## 1. Introduction

In 2013, the IEA released the final report of Task 24 operating under the HIA and carried out between spring 2007 and autumn 2011 [1]. The purpose was “to provide an overview for technologies which have a direct influence on development and implementation of systems integrating wind energy with hydrogen production [...]”, or, in other words, wind-hydrogen systems. The report categorizes wind-hydrogen systems (i.e., wind farms paired to HESSs) with respect to their main purpose and in terms of relevant sizes, identifying three categories. Systems under the “Electricity-storage” category target power smoothing against fluctuations in wind power by “[...] producing hydrogen at times of surplus power production and re-electrifying it during periods of underproduction. Such devices could facilitate wind

*power integration on a large scale, independent of support from fossil-fuel power stations.”* Thus, multiple balancing services can be provided to the grid addressing different timescales: from the shorter, where power balancing for voltage and frequency stability is addressed, to the mid-range, where energy balancing is addressed, to the larger, where the grid is supported in order to mitigate temporary bottlenecks.

This is also reflected in the scientific literature on power smoothing in wind farms, where even larger timescale ranges are addressed. For instance, in Zhao et al. [2] the authors investigate how the inertial energy of the turbines can be optimized in order to provide power smoothing across timescales of seconds, while timescales of the order of tens of seconds are, instead, addressed by Lyu et al. [3] where two strategies are developed and presented: firstly, power smoothing is targeted by simultaneous operations of the dc-link voltage control, the rotor speed control and the pitch angle control; then, a hierarchical arrangement is also proposed, which suitably and dynamically combines the three individual control schemes during the operations across timescales of the order of hundreds of seconds. Moving forward to timescales of the order of minutes, for example Lyu et al. [4] develops an automatic generation control for power smoothing which is set in response to the actual grid needs. At this point, the literature jumps to timescales of the order of hours, targeting, e.g., market participation/demand response programs [5–7] but without power smoothing, which instead is investigated in Abdelghany et al. [8], where an MPC-based strategy is developed featuring a two-step sequential optimization: firstly, a function of the previous output power variations, such that the new decided value does not lie too far from previous ones, is minimized; secondly, other costs are minimized, such as, e.g., a reference tracking cost, and, among the others, a similar function used in the first step is constrained so as not to exceed the previously optimal computed value. In this paper, we investigate a scenario similar to [8], which shares some of the authors of this paper; however, later, the differences will be highlighted in order to identify the major advancements and novelties beyond the state of the art.

Many other aspects concerning power smoothing in wind farms are also addressed by the literature. For instance, in Koiwa et al. [9] a control approach for power smoothing is proposed such that the required rated power of the used energy storage system can be reduced against what would be a typical design. In Yang et al. [10], the power smoothing that can be inherently achieved by clusters of wind turbines at the point of common coupling, is investigated against many parameters, such as different timescales and sampling intervals, wind speed, number of wind turbines, etc. In general, power smoothing in renewable energy plants is a very wide topic. The interested reader can refer to Barra et al. [11], where wind farms are specifically addressed, to Lamsal et al. [12], which also addresses photovoltaic generation and the references therein for comprehensive reviews.

Another interesting aspect relates to the used energy storage system. As an example, in Zhai et al. [13] the authors investigate the effectiveness of superconducting magnetic energy storage for power smoothing, while in Yang and Jin [14] the authors target output power smoothing with superconducting energy storage along with the additional aspects of low voltage ride-through capacity and power oscillations under asymmetrical faults; in Wang et al. [15], a dual battery energy storage system is considered in order to reduce the number of charging/discharging per battery, thus improving each battery's lifetime and the energy storage system economy in general. A good review of the literature targeting different kinds of energy storage systems (e.g., battery-, supercap-, flywheel-based, etc.), can be found always in Barra et al. [11], while aspects related to the performances of battery-based energy storage systems, with the aim of power smoothing in wind farms, are investigated in Sattar et al. [16]. Finally, hybrid configurations are also addressed [17,18]. Of course, the adopted energy storage systems interplay also with the possible timescales where they can be effectively operated, as show by [13,14] where timescales of the order of fractions of seconds and seconds are targeted, respectively.

Unfortunately, the above-mentioned papers do not address the case of HESSs. In this direction, some papers can be found roughly dating back to the first decade of 2000 [19–22].

Then, the topic shows a lesser relevance in the second decade while gaining a slightly increasing momentum in the current one, for instance, addressing hybrid storage systems hydrogen- and battery-based [23], hydrogen- and superconducting magnet-based [24], or coordinating a kinetic energy and a virtual discharge control [25].

In general, except for Abdelghany et al. [8], to the best of the authors' knowledge, the literature seems to not address exactly the use-case *energy-storage* as identified by the IEA-HIA in the final report of Task 24. In particular, this paper shares some similarities with Abdelghany et al. [8]:

- The scenario, i.e., a wind-hydrogen system targeting the use-case *energy-storage* as per the IEA-HIA Task 24 final report;
- The MLD modeling for including devices' dynamics depending on logical conditions;
- The MPC-based approach;
- The minimization of the devices' operating costs.

However, many differences exist and additional aspects are considered:

- Accounting for the power smoothing based on tracking a smooth profile contracted with the Transmission System Operator (TSO);
- Accounting for the participation to the spot market, which is competing with the aim of providing smooth power to the grid, since, for instance, the controller is also pushed not to electrolyze in case of both wind production and spot market prices peak;
- Accounting for the penalties that the wind farm owner/operator incurs in case the delivered power is below a threshold against what contracted;
- Accounting for the inherent hydrogen value, which is competing with the aim of providing smooth power to the grid, yet it is appealing for the wind farm owner/operator for leveraging hydrogen production for other purposes aside from the main one (i.e., power smoothing);
- Simpler devices' models based on practical considerations about their functioning and cost impacts on the optimal operations;
- Simpler control architecture with no sequential optimization;
- Simulations with real data from a wind farm in the center-south of Italy and real spot prices.

Finally, also fee-aware mechanisms seem not addressed by the literature, at least in the case of wind farms connected to the grid, to the best of the authors' knowledge.

The rest of the paper is organized as follows: In Section 2 the used mathematical frameworks and the development of the algorithms are presented, while Section 3 reports the simulation scenarios and corresponding results. Further, there we also provide an impact analysis of each cost term considered and possible choices of the corresponding weights. Section 4 concludes the paper.

## 2. Materials and Methods

The core tools used for the proposed investigation are the MLD framework for modeling and the MPC scheme for control.

### 2.1. MLD Framework

Systems governed by physical laws, logic rules and constraints are known as MLD systems and can be modeled as dynamic equations subject to linear inequalities where real and integer/Boolean variables appear [26], which establishes the so-called MLD framework. The power of the framework is that, for instance, qualitative facts can also be rephrased into logic rules and thus accounted for via inequalities in, e.g., a possible mathematical program implemented and solved via an MPC scheme for control purposes, as happens in this paper.

The underlying machinery can be easily understood with a few examples, while for a thorough presentation the reader is referred to Bemporad and Morari [26] and the references therein. An important ingredient is the link that can be established between

a function, say  $f$ , and an *indicator* variable, say  $\delta$ , such that, e.g.,  $f > 0$  implies  $\delta = 1$ . The indicator variable can be a logic variable when systems with dynamics depending also on logic conditions are targeted. In other terms, an important ingredient is how logical statements can be translated into mathematical inequalities. For instance, we consider the statement  $[f > 0] \rightarrow [\delta = 1]$ , where the brackets indicate the sentence resulting by the articulation of the mathematical condition they enclose, i.e.,  $[f > 0]$  stands for “the function  $f$  is positive” and  $[f > 0] \rightarrow [\delta = 1]$  indicates the *compound* statement “the function  $f$  is positive implies the indicator variable  $\delta$  is 1”. Thus, it is easy to check that [27]

$$[f > 0] \rightarrow [\delta = 1] \text{ is equivalent to } f \leq (\max f) \delta. \quad (1)$$

Indeed, if  $f > 0$ , the only way for the mathematical inequality on the right of (1) to be true is that  $\delta = 1$ , while, if  $f \leq 0$ , the statement on the left of (1) does not enable any conclusion about  $\delta$  and the same holds for the inequality on the right. We stress that, in (1),  $\max f$  is necessary since the inequality must hold for any value  $f$  can take, but any other number greater than  $\max f$  is sufficient. Indeed, sometimes it is easier to find an overestimate of  $\max f$ , though this may imply higher computational burdens for an optimizer, e.g., in case the models are used in a mathematical program that is subsequently solved numerically.

Now, in the paper we will also often use  $[f \leq 0] \rightarrow [\delta = 1]$  which can be easily worked out by rephrasing it similarly to (1). Firstly, we notice that  $[f \leq 0] \rightarrow [\delta = 1]$  can be rephrased as  $[f < \epsilon] \rightarrow [\delta = 1]$ , where  $\epsilon > 0$  is a tolerance such that zero is accounted for and inequality is assumed satisfied. This comes also in handy when the equations are implemented on a digital computer such that the tolerance can be set to the machine’s precision. Then, by another small rephrasing, we obtain  $[f - \epsilon < 0] \rightarrow [\delta = 1]$ , following  $[-f + \epsilon > 0] \rightarrow [\delta = 1]$ . Thus, by comparison with (1), we achieve

$$[f \leq 0] \rightarrow [\delta = 1] \text{ is equivalent to } f \geq \epsilon + (\min f - \epsilon) \delta, \quad (2)$$

since  $\max -f = -\min f$ .

## 2.2. MPC Schemes

MPC schemes are widely adopted control schemes where, in a typical and simple implementation, a control problem is cast at discrete-time  $k$ , such that, at each time step, optimal commands  $u_k^*$  are provided to the target plant via the optimization of a cost function subject to some constraints, see Figure 1. The optimization is carried out across a (prediction) horizon of duration  $N$  ahead in the future, with a set of constraints including also the plant dynamics, and resulting in  $N$  optimal commands, say  $u_k^*, \dots, u_{k+N-1}^*$ . However, only the first one is applied while the others are discarded, because the optimization is re-triggered at  $k + 1$ , such that the new state of the plant, determined by the implementation of  $u_k^*$ , is considered and updated exogenous conditions are handled as well.

Of course, as already said, what is explained refers to one of the many possible implementations of MPC that can be found in the literature. Yet, this suffices for the exposition of the results that are presented in this paper.

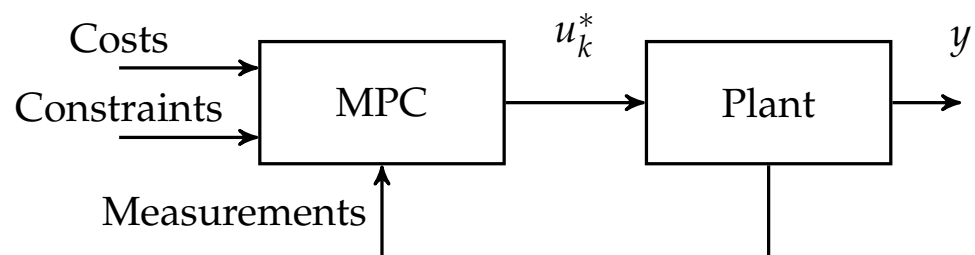


Figure 1. A simple MPC scheme.

### 2.3. Assumptions and Notation

Throughout the paper, the following assumptions and notations will be used:  $\alpha, \beta \in \{\text{STB}, \text{ON}\}$  are two generic indices, where STB, ON are the admissible logic states for a device's corresponding automaton; sometimes  $\alpha$  and  $\beta$  are used in conjunction and in this case we agree that  $\alpha \neq \beta$ ; logic variables are  $\delta^\alpha, \sigma_\beta^\alpha, \zeta_\leq^\alpha, \zeta_\geq^\alpha \in \{0, 1\}$  and mixed-logic variables are  $y$ s with some superscript, e.g.,  $y^\alpha$  given by the product of  $p\delta^\alpha$ , with  $p \in \mathbb{R}^+$ ; small slanted fonts are used to indicate time-varying quantities at current discrete-time  $k$ ;  $T_s$  and  $N$  are the sampling time and the control horizon, respectively, and the notation  $(\ )^+$  is used to indicate a time-varying variable at the next time step; sometimes the subscripts  $e$  and  $f$  will be used to highlight that a quantity refers to the "e"lectrolyzer or to the "f"uel cell, respectively. Finally,  $\mathbf{1}$  and  $\mathbf{0}$  indicate column vectors of suitable dimensions with unitary and null entries, respectively, and bold letters indicate vectors that, in this paper, gather samples of the corresponding scalar time-varying quantity, increasingly from the current time, across the horizon  $N$ , e.g.,  $\delta^\alpha = [\delta^\alpha(k) \dots \delta^\alpha(k+N-1)]$  and  $(\delta^\alpha)^+ = [\delta^\alpha(k+1) \dots \delta^\alpha(k+N)]$ .

For the reader's convenience, in Table 1 the list of symbols used throughout the paper is also reported. There, we followed the rule that, for each reported symbol class, Greek letters go first.

**Table 1.** List of symbols.

Variables	
$\delta^\alpha$	Logic variable of a generic state $\alpha$
$\delta^{\text{fee}}$	Logic variable indicating the activation of a penalty fee
$\sigma_\beta^\alpha$	Logic variable of two generic states $\alpha$ and $\beta$
$y^\alpha$	Mixed variable of a generic state $\alpha$
$y^{\text{fee}}$	Mixed variable involved in the activation of a penalty fee
$\zeta_\leq^\alpha, \zeta_\geq^\alpha$	Logic (slack) variables of a generic state $\alpha$
$loh$	Level of hydrogen in the tank
$e$	Price profile contracted by the wind farm operator/owner with the Transmission System Operator (TSO)
$p$	A generic device's power
$p_{\text{grid}}$	Power delivered to the grid
$p_{\text{ref}}$	Reference power profile to track
$p_w$	Power profile by wind generation
$s$	Energy prices in the spot market
Cost terms	
$c_N$	Total costs across a horizon $N$
$c^\sigma (c_N^\sigma)$	Cost term related to state switchings of a generic device (across a horizon $N$ )
$c^{loh} (c_N^{loh})$	Cost term related to the level of hydrogen in the tank (across a horizon $N$ )
$c^{\text{OP}} (c_N^{\text{OP}})$	Cost term related to the operations of a generic device (across a horizon $N$ )
$c^{p_{\text{grid}}} (c_N^{p_{\text{grid}}})$	Cost term related to the tracking error of a power reference (across a horizon $N$ )
$c^{\text{fee}} (c_N^{\text{fee}})$	Cost term related to the activation of a penalty fee (across a horizon $N$ )
$d_N$	Total costs across a horizon $N$ of a generic device

Table 1. Cont.

Labels	
STB, ON	Names of logic states of a generic device's automaton
<b>Parameters</b>	
$\epsilon^{\text{fee}}$	Small tolerance
$\Pi_e$	Productivity of the electrolyzer
$\Pi_f$	Productivity of the fuel cell
$C_H$	Cost of hydrogen
$C_{\text{STB}}^{\text{ON}}$	Cost for a generic device to switch from STB to ON
$C_{\text{ON}}^{\text{STB}}$	Cost for a generic device to switch from ON to STB
$C^s$	Part of earnings paid by the wind farm operator/owner to a third party company
$\mathcal{D}_N$	Set of a generic device's decision variables across a horizon N
$H^{\text{max}}$	Maximum rated amount of hydrogen in the tank
$\text{LOH}^{\text{max}}$	Maximum level of hydrogen in the tank
$\text{LOH}^{\text{min}}$	Minimum level of hydrogen in the tank
$M^{\alpha, \text{max}}$	Upper-bound estimate of $p - p^{\alpha, \text{max}}$
$M^{\alpha, \text{min}}$	Upper-bound estimate of $p - p^{\alpha, \text{min}}$
$m^{\text{fee}}$	Upper-bound estimate of $p_{\text{grid}} - p_{\text{ref}} + \Delta P^{\text{fee}}$
$m^{\text{fee}}$	Lower-bound estimate of $p_{\text{grid}} - p_{\text{ref}} + \Delta P^{\text{fee}}$
$M^{y^{\alpha}}$	Upper-bound estimate of $y^{\alpha}$
$m^{y^{\alpha}}$	Lower-bound estimate of $y^{\alpha}$
N	Horizon
$p^{\alpha, \text{max}}$	A generic device's maximum power when in state $\alpha$
$p^{\alpha, \text{min}}$	A generic device's minimum power when in state $\alpha$
$p_e^{\text{STB}}$	Rated power of the electrolyzer in stand-by
$p_f^{\text{STB}}$	Rated power of the fuel cell in stand-by
$p_e^{\text{max}}$	Maximum rated power of the electrolyzer in on
$p_e^{\text{min}}$	Minimum rated power of the electrolyzer in on
$p_f^{\text{max}}$	Maximum rated power of the fuel cell in on
$p_f^{\text{min}}$	Minimum rated power of the fuel in on
$T_s$	Sampling time
$W^{\sigma}$	Weight related to the cost term $c^{\sigma}$ ( $c_N^{\sigma}$ )
$W^{\text{loh}}$	Weight related to the cost term $c^{\text{loh}}$ ( $c_N^{\text{loh}}$ )
$W^{\text{fee}}$	Weight related to the cost term $c^{\text{fee}}$ ( $c_N^{\text{fee}}$ )
$W^{\text{OP}}$	Weight related to the cost term $c^{\text{OP}}$ ( $c_N^{\text{OP}}$ )
$W^{p_{\text{grid}}}$	Weight related to the cost term $c^p$ ( $c_N^p$ )

#### 2.4. Description of the Scenario

Figure 2 depicts the scenario addressed, which is similar to that of [8], however with significant differences about the technological assumptions on the electrolyzer and the fuel cell, among the others.

##### Technology Driven Assumptions

1. Stand-by requires very low power, both for the electrolyzer and the fuel cell, that would otherwise need a very long off-duty period in order to be economically convenient to opt for off operations. Therefore, in our mathematical modeling, we do not consider a device can be switched off; in turn, this also implies that cold starts are subsequently not accounted for.
2. The sampling time addressed by the controller (order of tens of minutes) is much greater than the timescale across which warm starts take place (order of seconds), which, therefore, are not accounted for.
3. The devices have good time-response performance so that some typical limitations such as, e.g., ramp limits, are ineffective at the considered sampling times.

These assumptions and corresponding consequences are beneficial because they enable the formulation of simpler Mixed-Integer Linear (MIL) programs equipped with a reduced number of constraints to be fulfilled, e.g., with respect to [8].



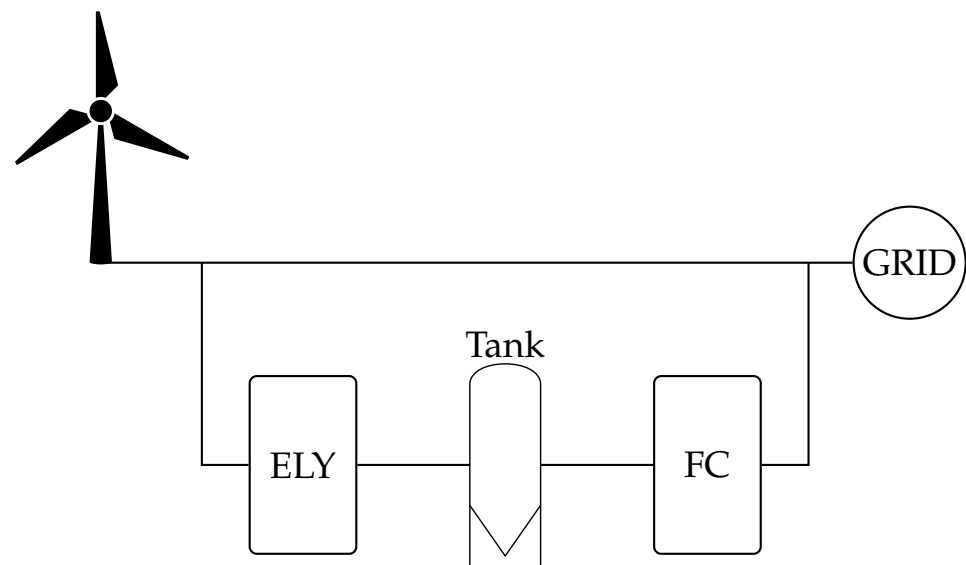


**Figure 2.** Simplified sketch of the addressed scenario. ELY stands for “electrolyzer” and FC stands for “fuel cell”.

### 2.5. Devices’ Logic Models

A device functioning is described by the conditions

$$p - P^{\alpha, \min} \geq 0, \quad p - P^{\alpha, \max} \leq 0 \quad \Longleftrightarrow \quad \delta^{\alpha} = 1, \quad (3)$$

where  $\delta^{\alpha}$ , which is 1 if state  $\alpha$  is TRUE, 0 otherwise, is a logic function of the state  $\alpha$ , and  $[P^{\alpha, \min}, P^{\alpha, \max}]$  identifies a power range which is relevant for that particular state  $\alpha$ . Figure 3 depicts a generic automaton such that the logic behavior of each device will be modeled via one corresponding instance. The picture also reports the transitions  $\sigma$ s among the states, that will be defined later and used to introduce corresponding switching costs.

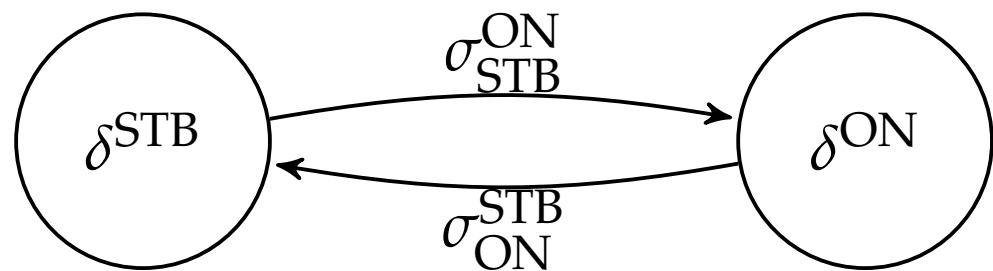


**Figure 3.** Two-state automaton for a generic device. The electrolyzer and the fuel cell operations are modeled according to two corresponding different instances.

#### 2.5.1. MLD Modeling

Equation (3) has to be recast so that it can be easily handled by numerical optimizers. Indeed, by applying the MLD modeling [26] directly to (3), the achieved inequalities would force  $p$  to take values within not compatible ranges when  $\delta^{\alpha} = 0$ , thus resulting in an unfeasible inequality set for the optimizer. Instead, a feasible inequality set can be achieved via the adoption of suitable (*auxiliary/slack*) logical variables  $z$ s that encode only the right-to-left implication in (3). In addition, for each inequality  $p - P^{\alpha, \min} \geq 0$ ,  $p - P^{\alpha, \max} \leq 0$ , a corresponding set of logical variables has to be used, i.e.,  $\zeta_{\geq}^{\alpha}$  and  $\zeta_{\leq}^{\alpha}$ , respectively.

Thus,

$$[\zeta_{\geq}^{\alpha} = 1] \rightarrow [p - P^{\alpha, \min} \geq 0] \quad \wedge \quad [\zeta_{\leq}^{\alpha} = 0] \rightarrow [p - P^{\alpha, \min} < 0], \quad (4)$$

are recast as

$$-(p - P^{\alpha, \min}) \leq M^{\alpha, \min} (1 - \zeta_{\geq}^{\alpha}), \quad (5a)$$

$$p - P^{\alpha, \min} \leq M^{\alpha, \min} \zeta_{\geq}^{\alpha}, \quad (5b)$$

respectively, and

$$[\zeta_{\leq}^{\alpha} = 1] \rightarrow [p - P^{\alpha, \max} \leq 0] \quad \wedge \quad [\zeta_{\leq}^{\alpha} = 0] \rightarrow [p - P^{\alpha, \max} > 0], \quad (6)$$

are recast as

$$p - P^{\alpha, \max} \leq M^{\alpha, \max} (1 - \zeta_{\leq}^{\alpha}), \quad (7a)$$

$$-(p - P^{\alpha, \max}) \leq M^{\alpha, \max} \zeta_{\leq}^{\alpha}, \quad (7b)$$

respectively, where  $M^{\alpha, \min} \geq \max(p - P^{\alpha, \min})$  and  $M^{\alpha, \max} \geq \max(p - P^{\alpha, \max})$ .

Then, it is necessary to establish a link among  $\delta^{\alpha}$ s and  $\zeta_{\geq}^{\alpha}$ s,  $\zeta_{\leq}^{\alpha}$ s, such that when  $\delta^{\alpha} = 1$ , then  $p \in [P^{\alpha, \min}, P^{\alpha, \max}]$  follows from (5) and (7). To this aim, we identify the logical statements

$$[\delta^{\alpha} = 1] \rightarrow [\zeta_{\geq}^{\alpha} = 1] \quad \wedge \quad [\delta^{\alpha} = 1] \rightarrow [\zeta_{\leq}^{\alpha} = 1], \quad (8)$$

which lead to

$$\delta^{\alpha} - \zeta_{\geq}^{\alpha} \leq 0, \quad (9a)$$

$$\delta^{\alpha} - \zeta_{\leq}^{\alpha} \leq 0, \quad (9b)$$

and

$$\sum_{\alpha} \delta^{\alpha} = 1, \quad (10)$$

because each automaton can be only in one state at a time. The compound statement (8) could be “rephrased” differently, i.e., as  $[\delta^{\alpha} = 1] \rightarrow [\zeta_{\geq}^{\alpha} = 1] \wedge [\zeta_{\leq}^{\alpha} = 1]$ , leading to a set of different, yet equivalent, inequalities from (9). However, the set would include a larger number of inequalities thus requiring a higher computational effort for a solver.

### 2.5.2. Transitions among the Logic States

The transitions among the logic states must be encoded through inequalities such that switching costs can be accounted for. To this aim, we consider logic functions  $\sigma_{\beta}^{\alpha}$ s of the initial and final states  $\beta$  and  $\alpha$ , respectively. They can be defined in terms of the corresponding logic functions  $\delta^{\beta}$  and  $\delta^{\alpha}$  of the involved states. In general,

$$[(\sigma_{\beta}^{\alpha})^{+} = 1] \leftrightarrow [(\delta^{\alpha})^{+} = 1] \quad \wedge \quad [\delta^{\beta} = 1] \quad (11)$$

holds, which corresponds to

$$-(\delta^{\alpha})^{+} + (\sigma_{\beta}^{\alpha})^{+} \leq 0, \quad (12a)$$

$$-\delta^{\beta} + (\sigma_{\beta}^{\alpha})^{+} \leq 0, \quad (12b)$$

$$(\delta^{\alpha})^{+} + \delta^{\beta} - (\sigma_{\beta}^{\alpha})^{+} \leq 1. \quad (12c)$$

### 2.6. Physical Dynamics, Balances and Operating Ranges

In this section, the physical dynamics, balances and operating ranges required for the achievement of a proper MPC scheme are presented.

### 2.6.1. Auxiliary Variables for Mixed Products

Many equations that are needed for the development of the proposed controller involve the mixed product between continuous variables and logic functions of the states. These non-linearities can be easily hidden through the introduction of auxiliary variables and handled via suitable constraints by an optimizer. That is

$$y^\alpha = p \delta^\alpha \quad (13)$$

are set, and

$$y^\alpha \leq M^{y^\alpha} \delta^\alpha, \quad (14a)$$

$$y^\alpha \geq m^{y^\alpha} \delta^\alpha, \quad (14b)$$

$$y^\alpha \leq p - m^{y^\alpha} (1 - \delta^\alpha), \quad (14c)$$

$$y^\alpha \geq p - M^{y^\alpha} (1 - \delta^\alpha), \quad (14d)$$

are included, where  $M^{y^\alpha} \geq \max y^\alpha$  and  $m^{y^\alpha} \leq \min y^\alpha$ .

### 2.6.2. Hydrogen Level Dynamics

The Level of Hydrogen (LoH) dynamics are affected by both the electrolyzer and the fuel cell operations, and are modeled by discretization of a continuous-time model with sampling time  $T_s$ , resulting in

$$(loh)^+ = loh + \Pi_e \frac{y_e^{ON}}{H^{\max}} T_s - \frac{1}{\Pi_f} \frac{y_f^{ON}}{H^{\max}} T_s, \quad (15)$$

where  $(loh)^+$  and  $loh$  are the LoH at the next and the current time step, respectively, and are given in terms of fractions of  $H^{\max}$ ;  $\Pi_e$  ( $[\Pi_e] = \text{kg/kWh}$ ) and  $\Pi_f$  ( $[\Pi_f] = \text{kWh/kg}$ ) are the productivities of the electrolyzer and the fuel cell, respectively, and  $y_e^{ON}$ ,  $y_f^{ON}$  are two instances of (13) for the electrolyzer and the fuel cell, respectively (correspondingly, in the MPC controller two instances of (14), one for the electrolyzer and one for the fuel cell, will be also included, as well as two instances of all the equations/variables that so far have been cast/introduced without relating them to a particular device and for which this, instead, concerns). We remark that  $y_e^{ON}$ ,  $y_f^{ON}$  can be both positive at the same time, i.e., the electrolyzer and the fuel cell are not forced to work in mutual exclusivity. This is useful in order to provide an additional degree of freedom that the controller can leverage in order to minimize the switching costs.

### 2.6.3. Power Balance

According to the scenario depicted in Figure 2, the node downstream of the wind farm forces the power balance constraint

$$p_w - y_e^{ON} + y_f^{ON} - p_{\text{grid}} = 0, \quad (16)$$

that will be included in the controller to produce physically meaningful commands, clearly along with

$$p_{\text{grid}} \geq 0, \quad (17)$$

since in the case under investigation, the power cannot be drawn from the grid.

### 2.6.4. Operating Ranges

The electrolyzer and the fuel cell power ratings

$$p_{e, \text{ON}, \text{min}} = p_{e, \text{min}}, \quad (18a)$$

$$p_{e, \text{ON}, \text{max}} = p_{e, \text{max}}, \quad (18b)$$

$$p_{e, \text{STB}, \text{min}} = p_{e, \text{STB}, \text{max}} = p_{e, \text{STB}}, \quad (18c)$$

$$p_{f, \text{ON}, \text{min}} = p_{f, \text{min}}, \quad (18d)$$

$$p_{f, \text{ON}, \text{max}} = p_{f, \text{max}}, \quad (18e)$$

$$p_{f, \text{STB}, \text{min}} = p_{f, \text{STB}, \text{max}} = p_{f, \text{STB}}, \quad (18f)$$

and the tank operating ranges in terms of LoH ratings

$$\text{LOH}^{\text{min}} \leq \text{loh} \leq \text{LOH}^{\text{max}}, \quad (19)$$

are also included.

Equations (4)–(14) have to be instantiated for each device (i.e., roughly speaking one copy indexed with  $e$  and one copy indexed with  $f$  have to be considered) and combined either with (18a)–(18c) in case of the electrolyzer or with (18d)–(18f) in case of the fuel cell, such that a corresponding “concrete” model is achieved.

## 2.7. Scenario Objectives and Requirements

In the addressed scenario, the integrated system is operated in order to inject smooth power into the grid. Aside from this main purpose, the costs due to the operations should also be minimized, as well as some profit opportunities should be taken (i.e., maximized). This determines the number of related terms that are included in the controller’s objective function and that are developed in what follows. The terms will be also weighted such that prioritization is enabled.

### 2.7.1. Smooth Power Injection

In the case under investigation, smooth power injection into the main grid is pursued via the tracking of a reference profile  $p_{\text{ref}}$ —which is considered smooth by contracts between the wind farm operator/owner and the electricity market operator—modeled as the relative quadratic deviation

$$c^{p_{\text{grid}}} = (p_{\text{grid}} - p_{\text{ref}})^2, \quad (20)$$

and included as a cost in the controller.

### 2.7.2. Profits/Fees for Contracted Power Delivery

The reference profile  $p_{\text{ref}}$  in (20) can be a contracted power that the wind farm operator/owner agrees with the TSO the day before the dispatchment day, and may reflect the trade-off regarding the expected profits generated via selling smooth power and the likelihood that such amount of electricity can be actually delivered, based on forecasts of the wind generation. The forecasts are usually provided by third-party companies, that assume the responsibility of paying the penalty fees in case of mismatches between the contracted power and that actually delivered, in exchange for a fixed income paid by the wind farm operator/owner in the percentage of the achieved profits. This mechanism is accounted for by including an additional logical variable  $\delta^{\text{fee}}$  which is activated upon  $p_{\text{grid}} - p_{\text{ref}}$  being less than the threshold  $-\Delta P^{\text{fee}}$ , where  $\Delta P^{\text{fee}} > 0$ . Indeed, the critical condition for the integrated system is that the power scheduled at the next time step is less than what is required. Especially in combination with too low LoH, this can lead to unrecoverable conditions where the wind generation and the hydrogen stored in the tank are not sufficient to fulfill the commitment with the TSO.

If  $p_{\text{grid}} - p_{\text{ref}}$  is less than the threshold  $-\Delta P^{\text{fee}}$ , the profit

$$(1 - C^s) e p_{\text{grid}} T_s, \quad (21)$$

which otherwise would be realized, is subsequently deactivated, where  $C^s$  is the part of the earnings achieved by selling the contracted power to the TSO paid by the wind farm operator/owner to the third party company, and  $e$  is a (possibly time-varying) price agreed upon the day before the dispatchment day by the wind farm operator/owner and the TSO.

In summary, the link between  $\delta^{fee}$  and  $\Delta P^{fee}$  is established via

$$[p_{grid} - p_{ref} + \Delta P^{fee} \leq 0] \leftrightarrow [\delta^{fee} = 1], \quad (22)$$

and the resulting constraints

$$p_{grid} - p_{ref} + \Delta P^{fee} \leq M^{fee}(1 - \delta^{fee}), \quad (23a)$$

$$p_{grid} - p_{ref} + \Delta P^{fee} \geq \epsilon^{fee} + (m^{fee} - \epsilon^{fee})\delta^{fee}, \quad (23b)$$

that have to be included in the controller, where  $\epsilon^{fee} > 0$  is a small positive constant required in order for the equivalence between the left-to-right implication in (22), encoding as (23b), to hold on the boundary of  $p_{grid} - p_{ref} + \Delta P^{fee} \leq 0$ ,  $M^{fee} \geq \max(p_{grid} - p_{ref} + \Delta P^{fee})$  and  $m^{fee} \leq \min(p_{grid} - p_{ref} + \Delta P^{fee})$ . Then, the cost term

$$-(1 - \delta^{fee})(1 - C^s)e p_{grid} T_s \quad (24)$$

is identified. However, (24) clearly implies the mixed product  $\delta^{fee} p_{grid}$ , such that also the mixed variable

$$y^{fee} = \delta^{fee} p_{grid}, \quad (25)$$

is introduced, and the constraints

$$y^{fee} \leq M^{fee} \delta^{fee}, \quad (26a)$$

$$y^{fee} \geq m^{fee} \delta^{fee}, \quad (26b)$$

$$y^{fee} \leq p_{grid} - m^{fee}(1 - \delta^{fee}), \quad (26c)$$

$$y^{fee} \geq p_{grid} - M^{fee}(1 - \delta^{fee}), \quad (26d)$$

are considered too. Therefore, a cost that the controller will aim at minimizing is

$$c^{fee} = -(p_{grid} - y^{fee})(1 - C^s)e T_s. \quad (27)$$

In (27), the coefficient  $1 - C^s$  can be absorbed into the weight associated with  $c^{fee}$  when combined with other cost terms in the optimization set up in Section 2.8.4. However, it will be explicitly kept in order to highlight the fee awareness.

In conclusion, the controller has the freedom to output a schedule that, in principle, may not fulfill the commitment with the TSO (for example because the reference profile was defined upon erroneous wind generation forecasts), however at the price of deactivating the profits that otherwise would be implied. In case of negative mismatches exceeding the threshold  $-\Delta P^{fee}$ , the deriving fee is paid by the third party company. In turn, this could impact the price of future service renewals, thus resulting in a future cost increase; however, this is not accounted for by the developed controller, but can be the topic for future investigations.

### 2.7.3. Costs During Operations

In general, the costs inherent to the devices' operations are multiple. In the case under investigation they are also similarly defined as being related either to the electrolyzer or the fuel cell. According to the addressed timescales, the relevant costs are those due to the

electrolyzer and the fuel cell power consumptions during STB and ON operations—and therefore accounted for via a corresponding instance of

$$c^{OP} = s (y^{STB} + y^{ON}) T_s, \quad (28)$$

where  $s$  is the energy price in the spot market—and to the switchings between the operating modes, accounted for via a corresponding instance of

$$c^\sigma = C_{STB}^{ON} \sigma_{STB}^{ON} + C_{ON}^{STB} \sigma_{ON}^{STB}, \quad (29)$$

where  $C_{STB}^{ON}$  and  $C_{ON}^{STB}$  are the switching costs per cycle when a device switches from STB to ON and vice-versa, respectively.

#### 2.7.4. Costs/Opportunities

In general, hydrogen has a potential value that the wind farm operator/owner wants to consider even though the integrated system is operated in agreement with the energy-storage use case. The potential value of the produced hydrogen is the possible profit that the wind farm operator/owner would realize in case that amount of hydrogen was sold as fuel instead of being re-electrified. Thus, the controller will also aim at maximizing

$$c^{loh} = C_H loh H^{\max}, \quad (30)$$

where  $C_H$  is the cost of hydrogen per kilogram. However, this should not significantly conflict with the provision of contracted smooth power injection and, therefore, the corresponding weight that will be used when  $c^{loh}$  is combined with the other costs has to be carefully chosen.

#### 2.8. Controller Implementation

MPC controller is implemented at discrete-time  $k$ , with sampling time  $T_s$  (such that the continuous time correspondence can be recovered as  $t = k T_s$ ) and prediction horizon  $N$ . A constrained optimization is carried out at each  $k$  till  $k + N - 1$ , thus resulting in  $N$  future optimal values for each decision variable against which the optimization is carried out. However, only the values at  $k$  are input while the others are discarded. Then, at  $k + 1$  the relevant state of the plant is measured/computed such that it is used as the initial condition for the incoming MPC iteration.

In agreement with the notation defined in Section 2.3, the constraints and the costs previously developed are now rewritten in vector form.

##### 2.8.1. Vectorized Logic and Mixed Variable Constraints

Equations (5), (7), (9) and (10), which encode the links among powers, logic states and slack variables, are written as

$$-(p - P^{\alpha, \min}) \leq M^{\alpha, \min} (1 - \zeta_{\geq}^{\alpha}), \quad (31a)$$

$$p - P^{\alpha, \min} \leq M^{\alpha, \min} \zeta_{\geq}^{\alpha}, \quad (31b)$$

and

$$p - P^{\alpha, \max} \leq M^{\alpha, \max} (1 - \zeta_{\leq}^{\alpha}), \quad (32a)$$

$$-(p - P^{\alpha, \max}) \leq M^{\alpha, \max} \zeta_{\leq}^{\alpha}, \quad (32b)$$

and

$$\delta^{\alpha} - \zeta_{\geq}^{\alpha} \leq 0, \quad (33a)$$

$$\delta^{\alpha} - \zeta_{\leq}^{\alpha} \leq 0, \quad (33b)$$



and

$$\sum_{\alpha} \delta^{\alpha} = \mathbf{1}, \quad (34)$$

respectively, where the (in)equalities are meant element-wise.

Similarly, (12) is written as

$$-(\delta^{\alpha})^{+} + (\sigma_{\beta}^{\alpha})^{+} \leq \mathbf{0}, \quad (35a)$$

$$-\delta^{\beta} + (\sigma_{\beta}^{\alpha})^{+} \leq \mathbf{0}, \quad (35b)$$

$$(\delta^{\alpha})^{+} + \delta^{\beta} - (\sigma_{\beta}^{\alpha})^{+} \leq \mathbf{1}, \quad (35c)$$

and (14) as

$$\mathbf{y}^{\alpha} \leq \mathbf{M}^{\mathbf{y}^{\alpha}} \delta^{\alpha}, \quad (36a)$$

$$\mathbf{y}^{\alpha} \geq \mathbf{m}^{\mathbf{y}^{\alpha}} \delta^{\alpha}, \quad (36b)$$

$$\mathbf{y}^{\alpha} \leq p \mathbf{1} - \mathbf{m}^{\mathbf{y}^{\alpha}} (\mathbf{1} - \delta^{\alpha}), \quad (36c)$$

$$\mathbf{y}^{\alpha} \geq p \mathbf{1} - \mathbf{M}^{\mathbf{y}^{\alpha}} (\mathbf{1} - \delta^{\alpha}). \quad (36d)$$

### 2.8.2. Vectorized Physical Dynamics, Balances and Operating Ranges

Moreover, the involved physical dynamics, balances and operating ranges (15)–(19) can be easily vectorized, resulting, respectively, in

$$(\mathbf{loh})^{+} = \mathbf{loh} + \Pi_{\mathrm{e}} \frac{\mathbf{y}_{\mathrm{e}}^{\mathrm{ON}}}{\mathbf{H}^{\max}} \mathbf{T}_{\mathrm{s}} - \frac{1}{\Pi_{\mathrm{f}}} \frac{\mathbf{y}_{\mathrm{f}}^{\mathrm{ON}}}{\mathbf{H}^{\max}} \mathbf{T}_{\mathrm{s}}, \quad (37)$$

and

$$p_{\mathrm{w}} - \mathbf{y}_{\mathrm{e}}^{\mathrm{ON}} + \mathbf{y}_{\mathrm{f}}^{\mathrm{ON}} - p_{\mathrm{grid}} = \mathbf{0}, \quad (38a)$$

$$p_{\mathrm{w}} \geq \mathbf{0}, \quad (38b)$$

and

$$\mathbf{p}_{\mathrm{e}}^{\mathrm{ON},\min} = \mathbf{p}_{\mathrm{e}}^{\min} \mathbf{1}, \quad (39a)$$

$$\mathbf{p}_{\mathrm{e}}^{\mathrm{ON},\max} = \mathbf{p}_{\mathrm{e}}^{\max} \mathbf{1}, \quad (39b)$$

$$\mathbf{p}_{\mathrm{e}}^{\mathrm{STB},\min} = \mathbf{p}_{\mathrm{e}}^{\mathrm{STB},\max} = \mathbf{p}_{\mathrm{e}}^{\mathrm{STB}} \mathbf{1}, \quad (39c)$$

$$\mathbf{p}_{\mathrm{f}}^{\mathrm{ON},\min} = \mathbf{p}_{\mathrm{f}}^{\min} \mathbf{1}, \quad (39d)$$

$$\mathbf{p}_{\mathrm{f}}^{\mathrm{ON},\max} = \mathbf{p}_{\mathrm{f}}^{\max} \mathbf{1}, \quad (39e)$$

$$\mathbf{p}_{\mathrm{f}}^{\mathrm{STB},\min} = \mathbf{p}_{\mathrm{f}}^{\mathrm{STB},\max} = \mathbf{p}_{\mathrm{f}}^{\mathrm{STB}} \mathbf{1}, \quad (39f)$$

and

$$\mathrm{LOH}^{\min} \mathbf{1} \leq \mathbf{loh} \leq \mathrm{LOH}^{\max} \mathbf{1}. \quad (40)$$

Similarly to what happens for the scalar versions of the devices' MLD models, in this case (39) have to be plugged into (31), (32) such that a “concrete” version is achieved.

### 2.8.3. Vectorized Objectives and Requirements

The vectorized version of constraints (23) are

$$p_{\mathrm{grid}} - p_{\mathrm{ref}} + \Delta P^{\mathrm{fee}} \mathbf{1} \leq \mathbf{M}^{\mathrm{fee}} (\mathbf{1} - \delta^{\mathrm{fee}}), \quad (41a)$$

$$p_{\mathrm{grid}} - p_{\mathrm{ref}} + \Delta P^{\mathrm{fee}} \mathbf{1} \geq \epsilon^{\mathrm{fee}} \mathbf{1} + (\mathbf{m}^{\mathrm{fee}} - \epsilon^{\mathrm{fee}}) \delta^{\mathrm{fee}}, \quad (41b)$$

the vectorized version of constraints (26) are

$$\mathbf{y}^{\text{fee}} \leq \mathbf{M}^{\text{fee}} \delta^{\text{fee}}, \quad (42a)$$

$$\mathbf{y}^{\text{fee}} \geq \mathbf{m}^{\text{fee}} \delta^{\text{fee}}, \quad (42b)$$

$$\mathbf{y}^{\text{fee}} \leq \mathbf{p}_{\text{grid}} - \mathbf{m}^{\text{fee}} (1 - \delta^{\text{fee}}), \quad (42c)$$

$$\mathbf{y}^{\text{fee}} \geq \mathbf{p}_{\text{grid}} - \mathbf{M}^{\text{fee}} (1 - \delta^{\text{fee}}), \quad (42d)$$

and the vectorized versions of costs (20) and (27)–(30) are

$$c_{\text{N}}^{\text{p}_{\text{grid}}} = (\mathbf{p}_{\text{grid}} - \mathbf{p}_{\text{ref}})^{\top} (\mathbf{p}_{\text{grid}} - \mathbf{p}_{\text{ref}}), \quad (43a)$$

$$c_{\text{N}}^{\text{fee}} = -(\mathbf{p}_{\text{grid}} - \mathbf{y}^{\text{fee}})^{\top} (1 - \mathbf{C}^{\text{s}}) \mathbf{e} \mathbf{T}_{\text{s}}, \quad (43b)$$

$$c_{\text{N}}^{\text{OP}} = \mathbf{s}^{\top} (\mathbf{y}^{\text{STB}} + \mathbf{y}^{\text{ON}}) \mathbf{T}_{\text{s}}, \quad (43c)$$

$$c_{\text{N}}^{\sigma} = \mathbf{C}_{\text{STB}}^{\text{ON}} \mathbf{1}^{\top} \sigma_{\text{STB}}^{\text{ON}} + \mathbf{C}_{\text{ON}}^{\text{STB}} \mathbf{1}^{\top} \sigma_{\text{ON}}^{\text{STB}}, \quad (43d)$$

$$c_{\text{N}}^{\text{loh}} = \mathbf{C}_{\text{H}} \mathbf{1}^{\top} \text{loh} \mathbf{H}^{\text{max}}, \quad (43e)$$

respectively.

#### 2.8.4. MPC Algorithm

Now, for a generic device, let us define the set of decision variables

$$\mathcal{D}_{\text{N}} = \{\mathbf{p}\} \bigcup_{\alpha} \{\delta^{\alpha}, \zeta_{\geq}^{\alpha}, \zeta_{\leq}^{\alpha}\}, \quad (44)$$

and the costs

$$c_{\text{N}} = W^{\text{p}_{\text{grid}}} c_{\text{N}}^{\text{p}_{\text{grid}}} + W^{\text{fee}} c_{\text{N}}^{\text{fee}} - W^{\text{loh}} c_{\text{N}}^{\text{loh}}, \quad (45a)$$

$$d_{\text{N}} = W^{\text{OP}} c_{\text{N}}^{\text{OP}} + W^{\sigma} c_{\text{N}}^{\sigma}, \quad (45b)$$

where  $W^{\text{p}_{\text{grid}}}$ ,  $W^{\text{fee}}$ ,  $W^{\text{loh}}$ ,  $W^{\text{OP}}$  and  $W^{\sigma}$  are suitable weights.

Then, the controller will

$$\underset{\mathcal{D}_{\text{e,N}}, \mathcal{D}_{\text{f,N}}}{\text{minimize}} \quad c_{\text{N}} + d_{\text{e,N}} + d_{\text{f,N}} \quad (46a)$$

subject to

An instance of (31)–(36)

$$\text{for the electrolyzer } (\alpha = \text{STB, ON}), \quad (46b)$$

An instance of (31)–(36)

$$\text{for the fuel cell } (\alpha = \text{STB, ON}), \quad (46c)$$

Physical dynamics, balances

$$\text{and operating ranges (37), (38) and (40)–(42), \quad (46d)$$

Domain constraints for the

logical variables,

where  $c_{\text{N}}$  is given in (45a) and where  $\mathcal{D}_{\text{e,N}}$ ,  $d_{\text{e,N}}$ , and  $\mathcal{D}_{\text{f,N}}$ ,  $d_{\text{f,N}}$  are instances of the set (44) of decision variables and of the cost (45b) for the electrolyzer and the fuel cell, respectively.

#### 2.9. Relaxation

In problem (46), the domain constraints for  $\sigma$ s can be relaxed from  $\{0, 1\}$  to  $[0, 1]$  since they will be forced to Boolean values by virtue of (35).

### 3. Results

The controller algorithm is implemented in Python 3.10 with Pyomo 6.4.0 [28–30] and FICO XPress [31] optimizer (an industrial-grade numerical solver using Branch-and-Bound Tree Search) with community license. The wind generation profiles refer to a real wind farm placed in the center-south of Italy (CSUD market zone), provided by Friendly Power s.r.l., San Martino Sannita, Benevento, Italy [32]; due to a change of ownership, only data for the first ten months of 2017 are available. Market prices are provided by Gestore dei Mercati Energetici (GME), i.e., the Italian energy market operator [33]. The reference profiles used by the controller are achieved by smoothing the generation profiles via a Savitzky-Golay polynomial filter of suitable size and order [34].

The numerical simulations are carried out under different scenarios in order to highlight the MPC controller performances; the sampling time is set as  $T_s = 0.167$  h (i.e., 10 min), and the equipment's parameters are reported in Table 2 for reference, while the scenarios addressed are summarized in Table 3. Further, the following key assumptions are understood:

- The wind generation and the energy price forecasts are the same of the actual wind generation and energy price profiles, respectively, i.e., the simulations are conducted under the assumption of perfect forecasts;
- There are no model mismatches, which, in combination with the previous bullet, results in the power injected to the grid and the LoH to be exactly what predicted by the controller (see (37) and (38));
- The price  $e$  agreed upon the day before the dispatchment day by the wind farm operator/owner and the TSO and the energy prices  $s$  in the spot market (forecasts) are the same, i.e.,  $e = s$ ;
- In all the considered scenarios, the initial conditions of the devices is STB and the initial LoH is 0.9 with exceptions where otherwise remarked.

The first three scenarios aim at highlighting the impact of each cost component in  $c_N$  (see (45a)) under the same operating conditions, i.e., the same generation and reference profiles, and equipment's parameters. The fourth scenario includes all the costs combined via an appropriate choice of the corresponding weights, achieved by carrying out a number of simulations. The fifth scenario replicates the fourth with the sole difference of the target period and the sixth scenario replicates the fifth however with the exception of a larger prediction horizon in order to highlight the impact on the optimal strategy computed by the MPC algorithm.

**Table 2.** Equipment's relevant parameters.

Parameter	Description	Value
$p_e^{\max}$	Max. on-power of the electrolyzer	2500 kW
$p_e^{\min}$	Min. on-power of the electrolyzer	300 kW
$p_e^{\text{STB}}$	Stand-by-power of the electrolyzer	1 kW
$(\Pi_e)^{-1}$	(Productivity of the electrolyzer) <sup>-1</sup>	52 kWh/kg
$p_f^{\max}$	Max. on-power of the fuel cell	2500 kW
$p_f^{\min}$	Min. on-power of the fuel cell	300 kW
$p_f^{\text{STB}}$	Stand-by-power of the fuel cell	1 kW
$\Pi_f$	Productivity of the fuel cell	17 kWh/kg
$H^{\max}$	Tank capacity	150 kg
$\text{LOH}^{\min}$	Min. LoH in the tank	1
$\text{LOH}^{\max}$	Max. LoH in the tank	0

**Table 3.** Summary of the addressed scenarios.

Scenario	Description	Reference Period	Parameter	Value
1	Isolate and highlight the impact of $c_N^{p_{grid}}$ on wind-hydrogen system operations	From 14:40 of 18 February 2017 to 14:40 of 20 February 2017	N $W_e^{OP}, W_e^{\sigma}$ $W_f^{OP}, W_f^{\sigma}$ $W^{fee}, W^{loh}$	18 samples (i.e., 3 h) 0 0 0
2	Isolate and highlight the impact of $c_N^{fee}$ on wind-hydrogen system operations	"	N $\Delta p^{fee}$ $W_e^{OP}, W_e^{\sigma}$ $W_f^{OP}, W_f^{\sigma}$ $W^{p_{grid}}, W^{loh}$	18 samples (i.e., 3 h) 2000 kW 0 0 0
3	Isolate and highlight the impact of $c_N^{loh}$ on wind-hydrogen system operations	"	N $W_e^{OP}, W_e^{\sigma}$ $W_f^{OP}, W_f^{\sigma}$ $W^{fee}, W^{p_{grid}}$	18 samples (i.e., 3 h) 0 0 0
4	Full-feature operations	"	N $\Delta p^{fee}$ $C_H$ $C^S$ $W_e^{OP}, W_e^{\sigma}$ $W_f^{OP}, W_f^{\sigma}$ $W^{p_{grid}}, W^{loh}$ $W^{fee}$	18 samples (i.e., 3 h) 2000 kW 3 €/kg 0.03 1, 10 1, 10 $0.015 \times 10^{-3}, 0.07$ 0.2
5	Full-feature operations	From 09:00 of 27 May 2017 to 09:00 of 29 May 2017	N $\Delta p^{fee}$ $C_H$ $C^S$ $W_e^{OP}, W_e^{\sigma}$ $W_f^{OP}, W_f^{\sigma}$ $W^{p_{grid}}, W^{loh}$ $W^{fee}$	18 samples (i.e., 3 h) 2000 kW 3 €/kg 0.03 1, 10 1, 10 $0.015 \times 10^{-3}, 0.03$ 0.2
6	Full-feature operations	From 09:00 of 29 May 2017 to 09:00 of 31 May 2017	N $\Delta p^{fee}$ $C_H$ $C^S$ $W_e^{OP}, W_e^{\sigma}$ $W_f^{OP}, W_f^{\sigma}$ $W^{p_{grid}}, W^{loh}$ $W^{fee}$	60 samples (i.e., 10 h) 2000 kW 3 €/kg 0.03 0.9, 8.6 1, 11 $0.015 \times 10^{-3}, 0.013$ 0.2

### 3.1. Scenario 1: Impact of Reference-Tracking Cost $c_N^{p_{grid}}$

The impact of  $c_N^{p_{grid}}$  is highlighted by simulations carried out with conditions as per Table 3. Figure 4 reports relevant profiles across the first day. The first graph shows the wind generation profile (blue line), the power reference that has to be delivered to the grid (black line) and the actual power delivered (dashed red line), the second graph shows the electrolyzer and the fuel cell powers, and the fourth graph shows the LoH. The control objective is to minimize  $c_N^{p_{grid}}$ . As it is possible to see, the controller tries to track the power reference  $p_{ref}$ , however with some mismatches  $p_{grid} - p_{ref}$ . For instance, in between 2 h–4 h,  $p_{ref} \approx 11,899$  kW and  $p_{grid} \approx 10,756$  kW resulting in a negative mismatch of approximately 1143 kW. This could imply a fee depending on the agreed  $\Delta p^{fee}$ . The mismatch is due to the combined effect of a drop in the actual wind generation and the LoH in the tank. Moreover, this is confirmed by the fuel cell power  $p_f$  which is decreased by the controller after being operated at maximum power for short time, exactly because the LoH is approaching zero. Finally, the fuel cell is switched to stand-by. Following, with a small time overlap,

the electrolyzer is switched on because of a peak in the actual wind generation. However the peak is not completely smoothed because of the limitations of the electrolyzer which, in spite being operated at maximum power, does not manage to electrify a sufficient amount of energy (here,  $\Pi_e$  is the penalizing factor). Anyway, the LoH increases as an obvious consequence. We remark that in this case, the term in the cost function that accounts for the fees is deactivated. Similar considerations can be performed for the (negative) mismatch between 16 h–18 h.

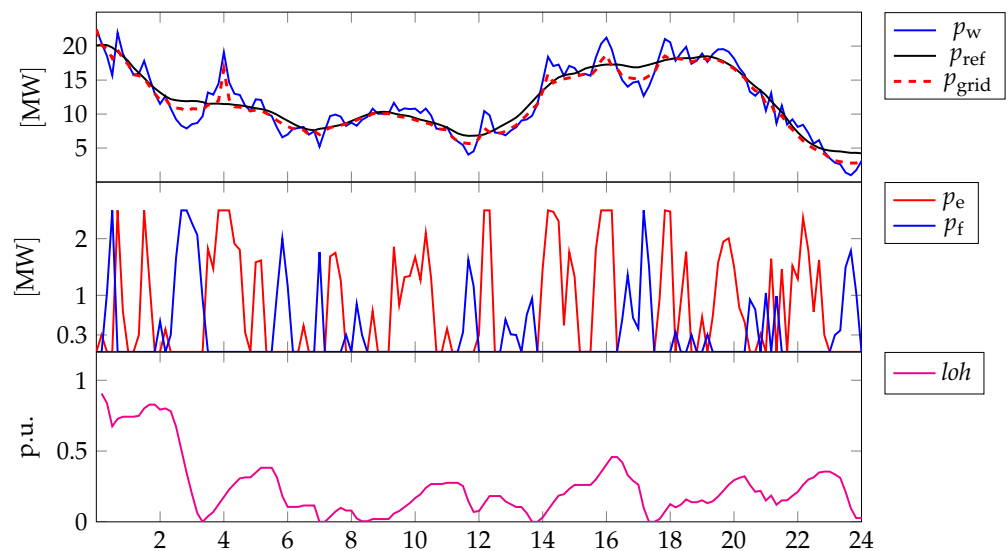


**Figure 4.** Different profiles related to the reference period from 14:40 of 18 February 2017 to the same hour of 19 February 2017, for highlighting the impact of  $c_N^{p_{\text{grid}}}$ . First graph: power by wind generation (blue line), power reference that has to be delivered to the grid (black line) and actual power delivered (dashed red line); Second graph: power of the electrolyzer (red line) and power of the fuel cell (blue line); Third graph: LoH.

Figure 5 reports graphs similar to those in Figure 4 but related to the subsequent reference period, i.e., from 14:40 of 19 February 2017 to the same hour of 20 February 2017: the wind generation is very low and this contributes in keeping the LoH low as well. However, at the beginning of the time window, i.e., in between 24 h–26 h, the local peak is used by the controller to produce some hydrogen since the contracted power to be delivered to the grid is smaller. As for the previous reference period, the peak is not totally smoothed because of the limitations of the electrolyzer. Subsequently, the wind generation and the contracted power are practically the same, with very small and scattered around fluctuations of the former in comparison with the latter, such that the controller has no degrees of freedom left in order to boost the LoH. However, what is important to highlight is that the considered peak is barely enough in order to follow the contracted power reference in the immediately following period, even though the negative mismatch between the wind generation and the contracted power therein is small in comparison to the positive similar mismatch in the previous period. This is due to the efficiency of the conversion process determined by the chain electrolyzer-fuel cell, which amounts to roughly 30%.

Finally, an interesting consideration regarding the devices' switchings can be performed: just before 38 h both the electrolyzer and the fuel cell are on and operated about at their minimum power. This may look counterintuitive and counterproductive. However, as remarked in the theoretical development of the devices' MLD models, mutually exclusive operations are not forced in order to give the controller an extra degree of freedom for the minimization of the switching costs. Anyway, in this case there is no switching cost minimization since the corresponding terms for each device are neglected. Neither this

could be justified on the contrary because none of the devices are in on before that time instant. Rather, the mismatch between the wind generation ( $p_w \approx 11$  kW) and the contracted power ( $p_{ref} \approx 141$  kW) cannot be minimized with the sole operations of either the electrolyzer or the fuel cell (depending on the sign of the mismatch) due to their minimum on-power being too high with respect to the hydrogen production/electrification capability required to the purpose. Thus, the controller operates the devices at the same time but with slightly different on-powers ( $y_e^{ON} \approx 300$  kW and  $y_f^{ON} \approx 390$  kW) so as to achieve a net effect that would require a device with lower minimum on-power (this outcome can be also leveraged in order to improve the devices' sizing). Nevertheless,  $p_{grid} \approx 104$  kW  $<$   $p_{ref}$  because of the impact of a very low LoH ( $loh \approx 0.04$ ).

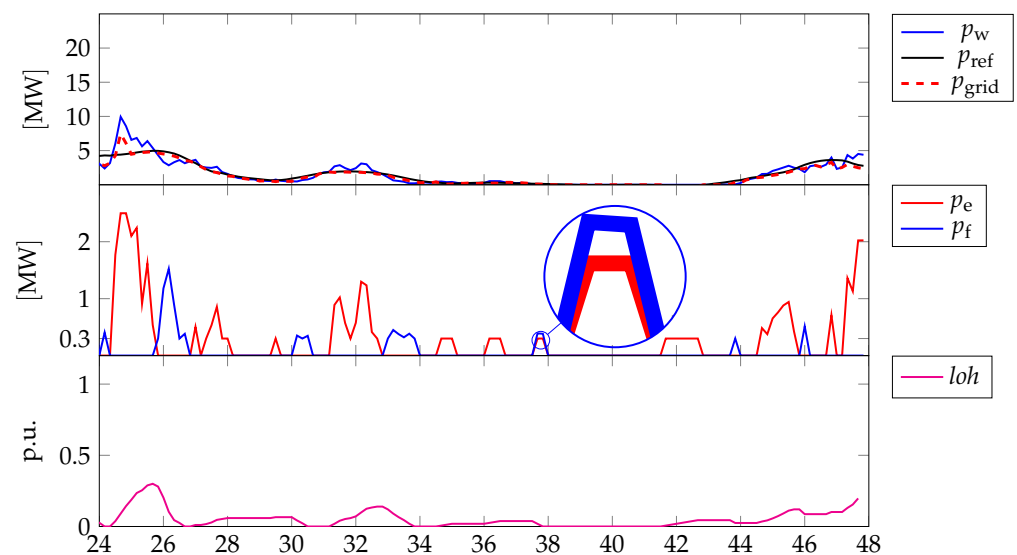


**Figure 5.** Different profiles related to the reference period 14:40 of 19 February 2017 to the same hour of 20 February 2017, for highlighting the impact of  $c_N^{p_{grid}}$ . First graph: power by wind generation (blue line), power reference that has to be delivered to the grid (black line) and actual power delivered (dashed red line); Second graph: power of the electrolyzer (red line) and power of the fuel cell (blue line); Third graph: LoH.

### 3.2. Scenario 2: Impact of Penalty Fees Cost $c_N^{fee}$

The impact of  $c_N^{fee}$  is highlighted by simulations carried out with data from the same reference period of Scenario 1 (Section 3.1), such that a comparison is also straightforward. For the other relevant conditions, as before, we refer to Table 3. Moreover, Figures 6 and 7 report the same quantities, with the only addition of the market price profile as second graph, since its relevance in  $c_N^{fee}$ . In this case, the control objective is to maximize  $c_N^{fee}$ .

In the first 24 h the controller operates the electrolyzer and, particularly, the fuel cell such that the negative mismatches between the reference and the power delivered to the grid are within the admissible deviation that does not activate the penalty fees. For instance, in between 2 h and 4 h the fuel cell is operated at about 80% (i.e., approximately 2000 kW), resulting in  $p_{grid} \approx 9934$  kW against  $p_{ref} \approx 11,899$  kW, and thus in a negative mismatch of approximately 1965 kW. This choice depends on the spot prices that do not promote the activation of the electrolyzer, and, indeed, the wind generation peak at 4 h is not leveraged to produce hydrogen by this means. As a result, the LoH drops dramatically. However, by chance, this has a very negligible impact on the performance of the wind-hydrogen system since the reference profile is tracked without incurring the fees in the following hours. In particular, this is also achieved via the activation of the electrolyzer in between 14 h and 16 h which realizes an increase in the LoH such that the subsequent drop in the wind generation can be mitigated appropriately. Anyway, just a few minutes before 24 h,



the negative mismatch between the reference profile and the wind generation cannot be prevented because barely any hydrogen is in the tank.

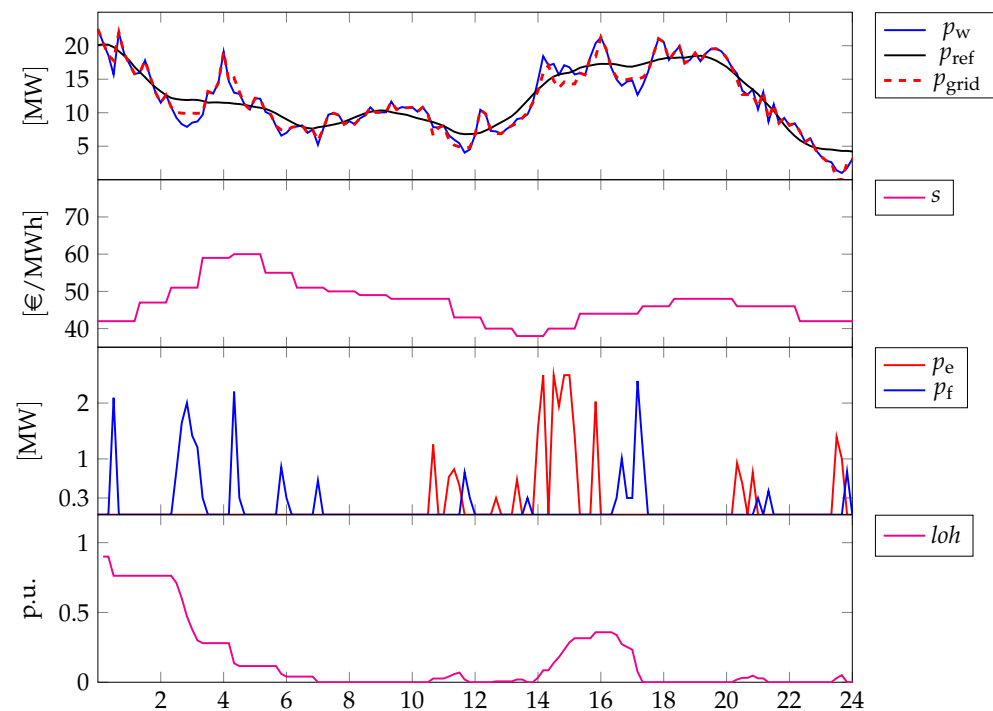


**Figure 6.** Different profiles related to the reference period from 14:40 of 18 February 2017 to the same hour of 19 February 2017, for highlighting the impact of  $c_N^{fee}$ . First graph: power by wind generation (blue line), power reference that has to be delivered to the grid (black line) and actual power delivered (dashed red line); Second graph: spot market prices  $s$  (source: “Gestore dei Mercati Energetici s.p.a.—[www.mercatoelettrico.org](http://www.mercatoelettrico.org) (accessed on 1 July 2022)”; Third graph: power of the electrolyzer (red line) and power of the fuel cell (blue line); Fourth graph: LoH.

Just by comparing the first 24 h of Scenario 2 and Scenario 1, the different implications of minimizing the sole  $c_N^{fee}$  vs. minimizing the sole  $c_N^{p_{grid}}$  (see Figures 4 and 6, respectively) are apparent. In particular, in Scenario 2 the controller is not committed to tracking a profile, rather it is in charge of not activating the fees and optimizing the revenues by selling energy to the grid. In compliance with this target, e.g., in between 2 h and 4 h, the controller produces the minimum effort in order not to activate the fees. This strategy does not promote the activation of the electrolyzer, such that, in terms of the resulting LoH in the tank, this is pretty much more likely to be very low or even zero. The differences between Scenario 2 and 1 are even more obvious by comparing the profiles of the subsequent 24 h, i.e., from 14:40 of 19 February 2017 to the same hour of 20 February 2017 (see Figure 5 and 7, respectively). In the case of Scenario 2, i.e., Figure 7, the LoH is zero across all the relevant periods, the electrolyzer and the fuel cell are never activated, such that the entire wind generation is delivered to the grid *as is*, and no penalties are paid as well. While, in the case of Scenario 1, i.e., Figure 5, the reference profile is better tracked, the electrolyzer and the fuel cell are activated for this purpose and the deriving LoH is less likely to be zero.

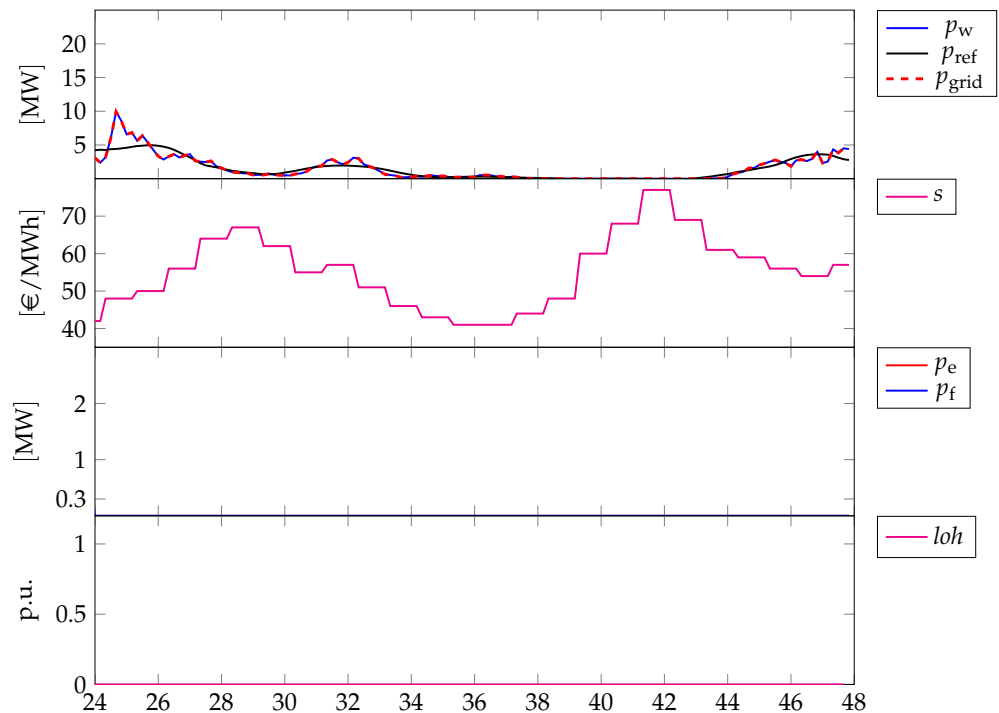


**Figure 7.** Different profiles related to the reference period 14:40 of 19 February 2017 to the same hour of 20 February 2017, for highlighting the impact of  $c_N^{fee}$ . First graph: power by wind generation (blue line), power reference that has to be delivered to the grid (black line) and actual power delivered (dashed red line); Second graph: spot market prices  $s$  (source: “Gestore dei Mercati Energetici s.p.a.—[www.mercatoelettrico.org](http://www.mercatoelettrico.org) (accessed on 1 July 2022)"); Third graph: power of the electrolyzer (red line) and power of the fuel cell (blue line); Fourth graph: LoH.

### 3.3. Scenario 3: Impact of Hydrogen Value Cost $c_N^{loh}$

In Scenario 3 the impact of the optimization of the sole  $c_N^{loh}$  is presented (see Table 3 for reference). The chosen relevant period for the numerical simulations is the same as the previous scenarios. Moreover, the relevant quantities are arranged differently, with the reference profile being not shown: the first graph reports the wind generation (blue line) and the power delivered to the grid (dashed red line); the second graph reports the electrolyzer (red line) and the fuel cell (blue line) powers; the third graph reports the LoH. In this case, the control objective is to maximize  $c_N^{loh}$ . In this sense, in order to set an adverse initial condition, LoH is set to 0.1, while in the previous scenarios was 0.9.

As Figure 8 shows, the controller operates the devices consistently with the objective. The electrolyzer is switched on at maximum power such that the LoH increases to the maximum. Subsequently, the electrolyzer is switched to stand-by, and the power delivered to the grid matches exactly that of wind generation.

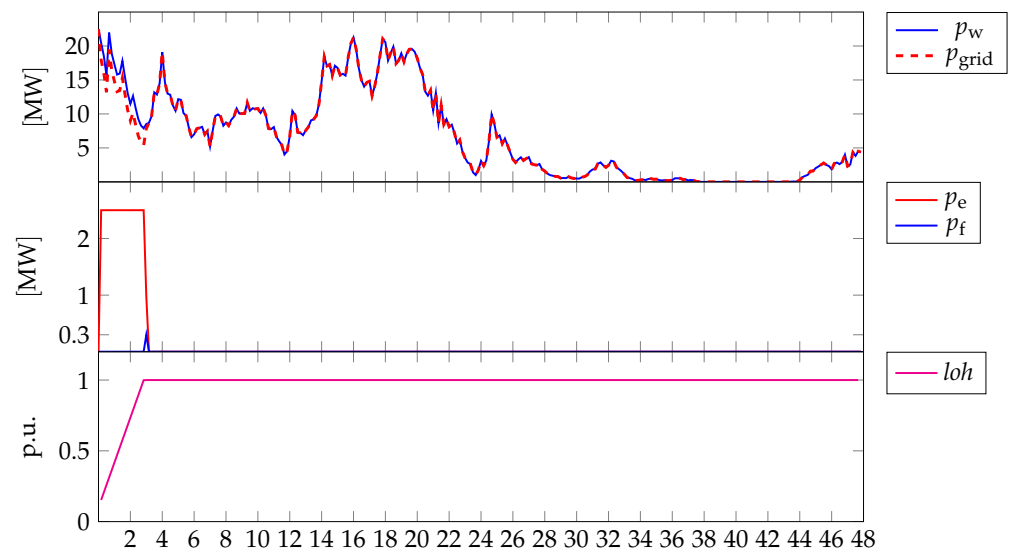


**Figure 8.** Different profiles related to the reference period from 14:40 of 18 February 2017 to the same hour of 20 February 2017, for highlighting the impact of  $c_N^{loh}$ . First graph: power by wind generation (blue line) and power delivered to the grid (dashed red line); Second graph: power of the electrolyzer (red line) and power of the fuel cell (blue line); Fourth graph: Level of Hydrogen (LoH).

### 3.4. Scenario 4: Full-Feature Operations with $N = 18$

In this scenario, all the cost terms developed in the article are included in the controller. The cost weights are chosen as per Table 3, following a number of simulations in order to find a good balance among all the (conflicting) objectives.

The relevant period for the assessment of the performances is the same as of the previous scenarios, as Figures 9 and 10 show. Across the whole time interval, fees are never activated, as the controller manages to mitigate the lack of renewable generation. For instance, this is highlighted in Figure 9, in between 2 h–4 h: the controller operates the fuel cell at full power with a subsequent steep drop of the LoH. However, as the renewable generation increases rapidly till a local peak, the fuel cell is switched to stand-by and the electrolyzer is operated at full power. In this case, the competing terms in the optimizer are  $c_N^{fee}$  and  $c_N^{loh}$ , with a lesser dominance of the former with respect to the latter. Thus, in spite of increasing spot prices, the positive peak in the generation is mitigated and used for hydrogen production. This helps the controller to oppose the future drops in the renewable generation via an appropriate re-electrification of the hydrogen. Anyway, as a tendency, the LoH is mostly likely to stay below 0.5 (with the initial condition set to 0.9), which suggests that the priority to the hydrogen production is appropriate (also because no fees are paid, as already noted) for the first timespan. Instead, in the subsequent 24 h, as Figure 10 shows, wind variability is minor and LoH increases notwithstanding some peaks in the spot prices which instead could be leveraged by the controller. However, selecting different values of the weights would not produce any improvement because the lesser the tendency to keep the hydrogen stored in the tank the higher the possibility that the controller uses this “degree of freedom” during the first 24 h, with the implication that in the second 24 h the LoH would be so low to prevent to re-electrify it anyway. In practice, setting dynamically the weights could be a possible solution.

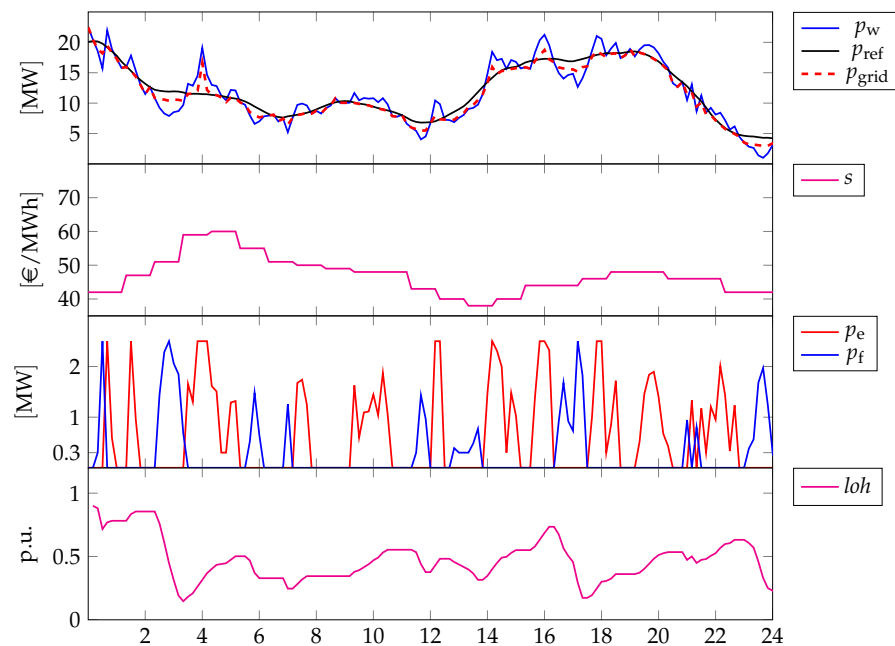


**Figure 9.** Different profiles related to the reference period from 14:40 of 18 February 2017 to the same hour of 19 February 2017, with full-feature operations. First graph: power by wind generation (blue line), power reference that has to be delivered to the grid (black line) and actual power delivered (dashed red line); Second graph: spot market prices  $s$  (source: “Gestore dei Mercati Energetici s.p.a.—[www.mercatoelettrico.org](http://www.mercatoelettrico.org) (accessed on 1 July 2022)”; Third graph: power of the electrolyzer (red line) and power of the fuel cell (blue line); Fourth graph: LoH.

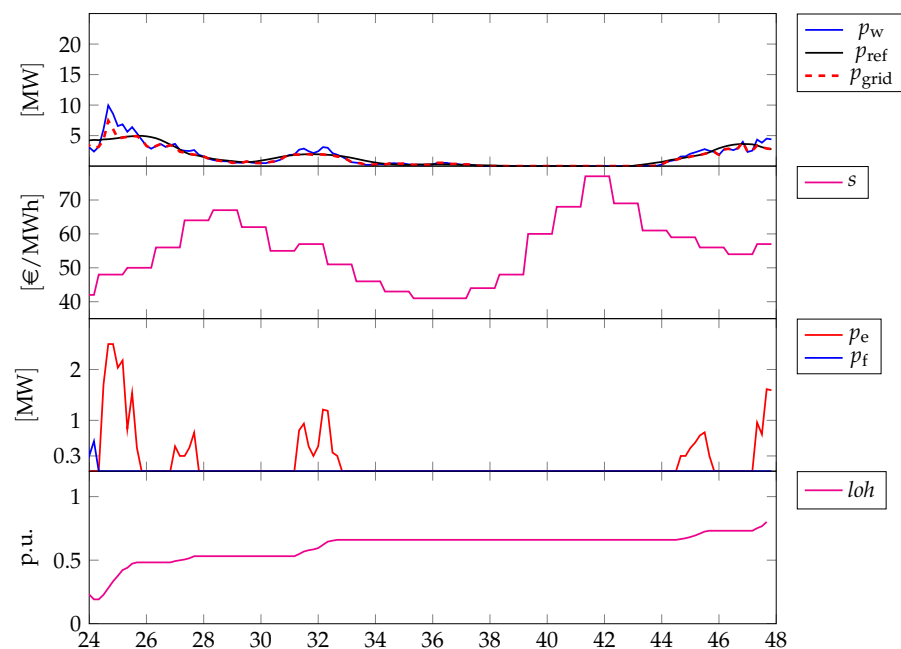


**Figure 10.** Different profiles related to the reference period from 14:40 of 19 February 2017 to the same hour of 20 February 2017, with full-feature operations. First graph: power by wind generation (blue line), power reference that has to be delivered to the grid (black line) and actual power delivered (dashed red line); Second graph: spot market prices  $s$  (source: “Gestore dei Mercati Energetici s.p.a.—[www.mercatoelettrico.org](http://www.mercatoelettrico.org) (accessed on 1 July 2022)”; Third graph: power of the electrolyzer (red line) and power of the fuel cell (blue line); Fourth graph: LoH.

### 3.5. Full-Feature Operations in Spring/Summer with $N = 18$ vs. $N = 60$

In this section, the effects of different prediction horizons in the same target period, i.e., Scenario 5 vs. Scenario 6, are highlighted, and the corresponding strategies are compared. In order to mitigate the bias of the single cost terms resulting naturally from the increase in the prediction horizon, their weights for  $N = 60$  are standardized against the horizon such that their averages across the whole simulation time amount to the same as the averages of the terms in case of  $N = 18$ .

Figures 11 and 12 show the different strategies provided by the controller within the first and the second 24 h, respectively, of 29 May 2017, with initial time set to 09:00 and initial condition for LoH set to 0.1. There, similar quantities as those in the previous discussions are presented, with the difference that dashed lines are used to indicate the evolutions of relevant quantities when pertaining to the strategy for  $N = 60$ .

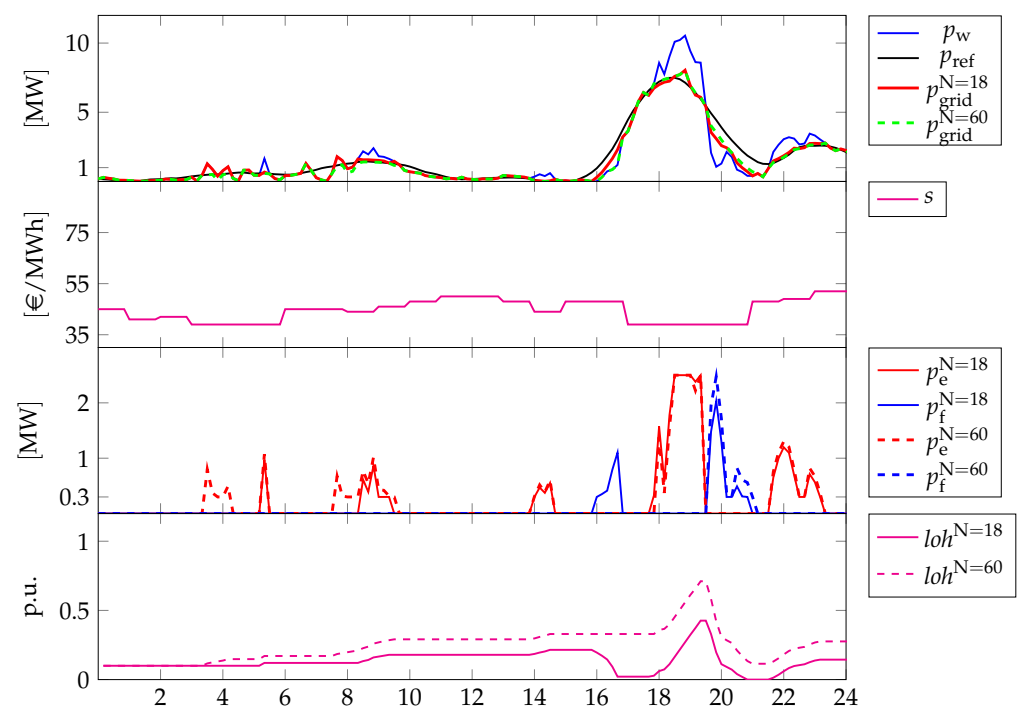


**Figure 11.** Different profiles related to the reference period from 09:00 of 29 May 2017 to the same hour of 30 May 2017, with full-feature operations:  $N = 18$  vs.  $N = 60$ . First graph: power by wind generation (blue solid line), power reference that has to be delivered to the grid (black solid line), actual power delivered when  $N = 18$  (red solid line) and actual power delivered when  $N = 60$  (green dashed line); Second graph: spot market prices  $s$  (source: “Gestore dei Mercati Energetici s.p.a.—[www.mercatoelettrico.org](http://www.mercatoelettrico.org) (accessed on 1 July 2022)”); Third graph: power of the electrolyzer when  $N = 18$  (red solid line), power of the fuel cell when  $N = 18$  (blue solid line), power of the electrolyzer when  $N = 60$  (red dashed line) and power of the fuel cell when  $N = 60$  (blue dashed line); Fourth graph: LoH when  $N = 18$  (magenta solid line) and LoH when  $N = 60$  (magenta dashed line).

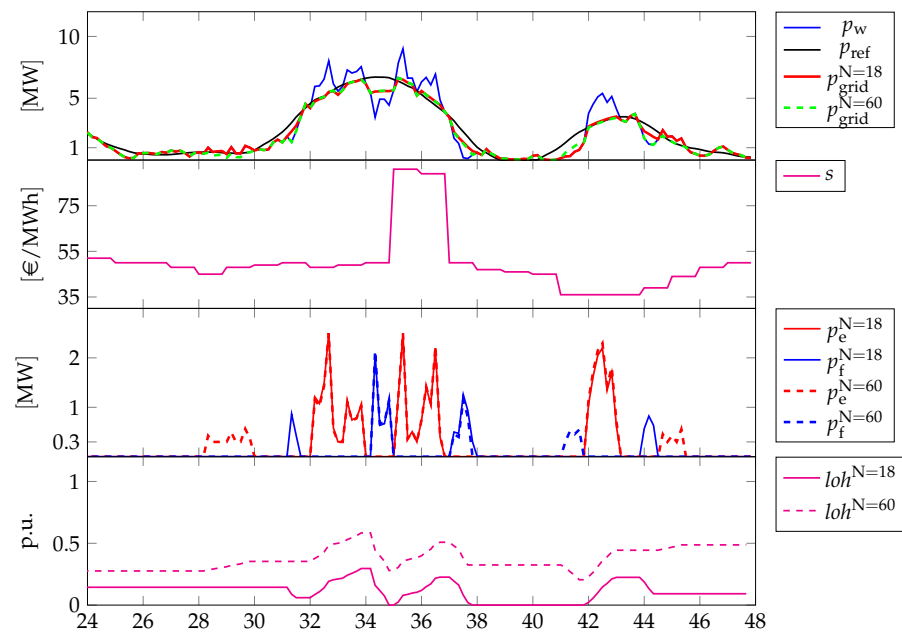


**Figure 12.** Different profiles related to the reference period from 09:00 of 30 May 2017 to the same hour of 31 May 2017, with full-feature operations:  $N = 18$  vs.  $N = 60$ . First graph: power by wind generation (blue solid line), power reference that has to be delivered to the grid (black solid line), actual power delivered when  $N = 18$  (red solid line) and actual power delivered when  $N = 60$  (green dashed line); Second graph: spot market prices  $s$  (source: “Gestore dei Mercati Energetici s.p.a.—[www.mercatoelettrico.org](http://www.mercatoelettrico.org) (accessed on 1 July 2022)”); Third graph: power of the electrolyzer when  $N = 18$  (red solid line), power of the fuel cell when  $N = 18$  (blue solid line), power of the electrolyzer when  $N = 60$  (red dashed line) and power of the fuel cell when  $N = 60$  (blue dashed line); Fourth graph: LoH when  $N = 18$  (magenta solid line) and LoH when  $N = 60$  (magenta dashed line).

As it is possible to notice, even though at first look the strategies might seem rather similar, they imply remarkable differences in the time evolution of the LoHs. In case of  $N = 18$ , the achieved LoH keeps generally low across the two days. While, in the case of  $N = 60$ , the controller manages to achieve an increasing evolution till  $loh = 0.5$  at the end of the second day. The differences in terms of  $p_{grid}$  are subtle, however, they are remarked by the different activation of the electrolyzer and the fuel cell. In case of  $N = 60$ , the controller tends to produce hydrogen more than in the case of  $N = 18$ , which is highlighted, for instance, by the activation of the electrolyzer about 4 h and in between 8 h and 10 h, roughly, or by the non activation of the fuel cell just about 16 h and the subsequent minutes. This more conservative strategy is achieved without incurring any fee, as  $\delta^{fee}$  keeps null across the entire simulation window (clearly the same happens when  $N = 18$  is considered). The differences in the strategy are highlighted also in the plots related to the second day, especially looking at those reporting the devices’ powers. In both cases, however, the peak in the spot prices is not leveraged for minimizing the costs accounted for by the term  $c_N^{fee}$ . Actually, this can be achieved by a different choice of the corresponding weight, i.e., increasing it such that, e.g.,  $c_N^{fee}$  becomes higher than  $c_N^{p_{grid}}$ . However, we remark that the choice is nontrivial in general, as also highlighted in Figure 13. In this figure, the strategies for two different choices of  $c_N^{fee}$  are reported, where solid lines denote the strategies achieved when the parameters, in general, and  $c_N^{fee}$  in particular, are as per Table 3, while dashed lines denote the strategies achieved when  $c_N^{fee}$  is increased to 3. Further, the whole two-days relevant period is addressed such that it is easy to check that fixed weights can be ineffective in some circumstances. The two strategies derive also from two different choices for the initial conditions of LoH, where, in the case of  $c_N^{fee} = 0.013$  (benchmark), the initial condition is set to 0.1 while, in the case of  $c_N^{fee} = 3$ , the initial



condition is set to 0.9, such that being the second strategy less conservative, this aspect can be better highlighted. The differences can be noted just within the first 24 h, where, in case of the benchmark value of  $c_N^{\text{fee}}$ , the evolution of the LoH is increasing due to the various activations of the electrolyzer. This results in small yet impactful differences in  $p_{\text{grid}}$  that lead to a general LoH decrease when  $c_N^{\text{fee}}$  is higher. Clearly, the higher priority given to the earnings from selling energy to the grid increases the tendency of not keeping too much hydrogen in the tank and/or not to produce hydrogen in case of (local) renewable peaks.

This tendency is confirmed in the subsequent 24 h, where in case of the increased  $c_N^{\text{fee}}$  the LoH is decreasing. In particular, in between 35 h–40 h, even though the LoH is very low, the controller leverages the local peak in the spot market to inject power into the grid at current prices, notwithstanding this implies zero LoH in the immediate forthcoming time period, while this choice is not adopted in the case of the benchmark  $c_N^{\text{fee}}$ . Possibly, a bigger tank could mitigate this decrease, in combination, as also pinpointed earlier, with the adoption of a dynamic weighting, which could also be a possible future research direction.

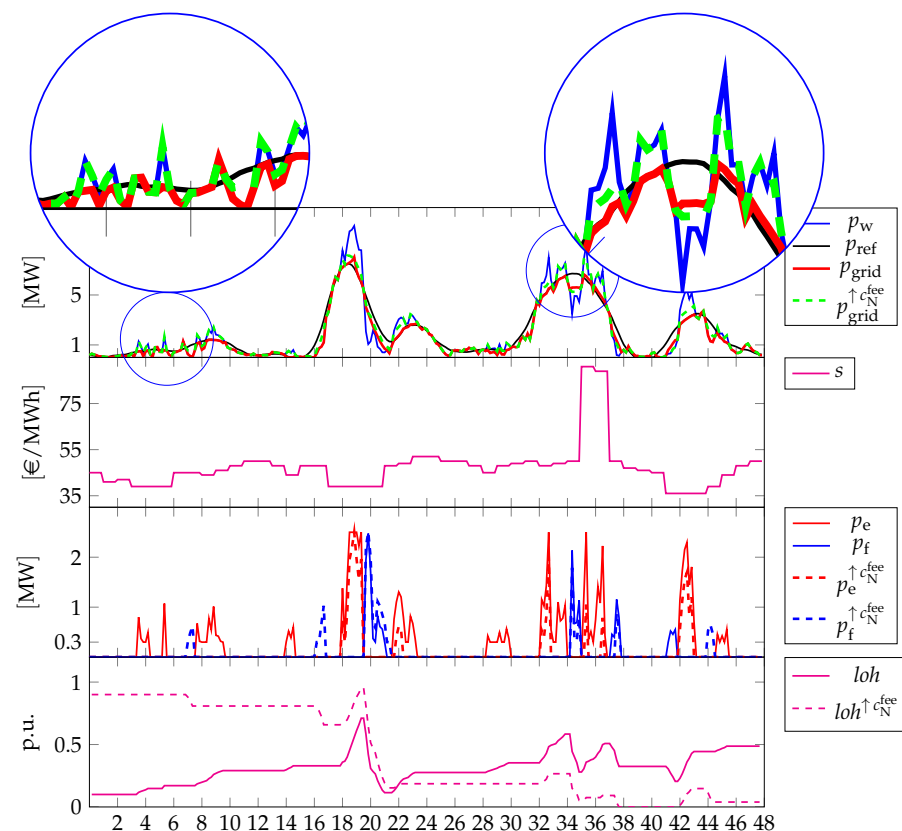


**Figure 13.** Different profiles related to the reference period from 09:00 of 29 May 2017 to the same hour of 30 May 2017, with full-feature operations:  $c_N^{\text{fee}} = 0.2$  vs.  $c_N^{\text{fee}} = 3$ . First graph: power by wind generation (blue solid line), power reference that has to be delivered to the grid (black solid line), actual power delivered when  $c_N^{\text{fee}} = 0.2$  (red solid line) and actual power delivered when  $c_N^{\text{fee}} = 3$  (green dashed line); Second graph: spot market prices  $s$  (source: “Gestore dei Mercati Energetici s.p.a.—[www.mercatoelettrico.org](http://www.mercatoelettrico.org) (accessed on 1 July 2022)”; Third graph: power of the electrolyzer when  $c_N^{\text{fee}} = 0.2$  (red solid line), power of the fuel cell when  $c_N^{\text{fee}} = 0.2$  (blue solid line), power of the electrolyzer when  $c_N^{\text{fee}} = 3$  (red dashed line) and power of the fuel cell when  $c_N^{\text{fee}} = 3$  (blue dashed line); Fourth graph: LoH when  $c_N^{\text{fee}} = 0.2$  (magenta solid line) and LoH when  $c_N^{\text{fee}} = 3$  (magenta dashed line).

#### 4. Discussion

This paper targets smooth power injection for wind farms paired to a HESS as established by the IEA in the final report of Task 24 operating under the HIA and published in

2013. This operating mode is considered one among the possible three that can promote the integration of wind generation into the grid and is not exactly covered by the actual literature. The paper develops an MPC strategy that relies on MLD modeling for the electrolyzer and the fuel cell, such that they can be operated by providing suitable logic commands and a continuous amount of powers they have to convert into hydrogen/re-electrify. The control strategy is demonstrated considering generation profiles of a real wind farm located in the center-south of Italy and corresponding real spot market prices. The addressed system and scenario are similar to those in [8], which shares some of the authors of this paper, however with a number of different assumptions, closer to a realistic application, that leads to quite different modeling and results. In addition to power smoothing, the control algorithms also include additional cost terms in order to account for the inherent value of the produced hydrogen and in order to account for the fees that the wind farm owner/operator might incur in case of infringement of the agreement with the TSO on the contracted power to be delivered to the grid.

The proposed controller shows enough flexibility to balance against different and competing objectives in real scenarios, providing that an appropriate choice of weights is adopted. In this regard, the simulations show that a dynamic choice of the weights corresponding to the costs and revenues that are optimized could be more appropriate since the controller performances can be strongly affected by the combination of the system conditions (e.g., the LoH in the tank) with the various exogenous' (e.g., the renewable generation and market prices). This, in general, can be a possible investigation research. Another possible research direction is identified by the use of the developed models and algorithms in order to carry out a scenario analysis with the aim of achieving different wind-hydrogen system sizes against multiple renewable generations and spot market profiles. The outcomes can be fruitfully used for a sizing that also accounts for the minimization of the devices' operating costs, among the many.

**Author Contributions:** Conceptualization, V.M., F.Z. and L.G.; methodology, V.M.; software, V.M.; validation, V.M.; formal analysis, V.M.; investigation, V.M.; resources, V.M.; data curation, V.M.; writing—original draft preparation, V.M.; writing—review and editing, V.M., F.Z. and L.G.; visualization, V.M.; supervision, F.Z. and L.G.; project administration, V.M.; funding acquisition, F.Z. All authors have read and agreed to the published version of the manuscript.

**Funding:** This project has received funding from the Fuel Cells and Hydrogen 2 Joint Undertaking (now Clean Hydrogen Partnership) under the European Union's Horizon 2020 research and innovation programme under grant agreement No. 779469.

**Data Availability Statement:** Wind generation profiles refer to 2017 are not public and owned by Friendly Power s.r.l., San Martino Sannita, Benevento, Italy. Spot market price profiles referring to 2017 are public and owned by "Gestore dei Mercati Energetici s.p.a.—[www.mercatoelettrico.org](http://www.mercatoelettrico.org) (accessed on 1 July 2022)". They can be downloaded either via the website (limited datastream capability) or via ftp and can be published only upon authorization.

**Conflicts of Interest:** The authors declare no conflict of interest.

## Abbreviations

The following abbreviations are used in this manuscript:

GME	Gestore dei Mercati Energetici
HESS	Hydrogen-based Energy Storage System
HIA	Hydrogen Implementing Agreement
IEA	International Energy Agency
LoH	Level of Hydrogen
MIL	Mixed-Integer Linear
MLD	Mixed-Logic Dynamic
MPC	Model Predictive Control
TSO	Transmission System Operator

## References

- Hoskin, A.; Pedersen, A.S.; Varkaraki, E.; Pino, F.J.; Aso, I.; Simón, J.; Lehmann, J.; Linnemann, J.; Stolzenburg, K.; Castrillo, L.; et al. *IEA-HIA Task 24—Wind Energy & Hydrogen Integration—Final Report*; Technical Report; International Energy Agency-Hydrogen Implementing Agreement. 2013. Available online: [https://www.ieahydrogen.org/wpfd\\_file/task-24-final-report/](https://www.ieahydrogen.org/wpfd_file/task-24-final-report/) (accessed on 29 August 2022).
- Zhao, X.; Yan, Z.; Xue, Y.; Zhang, X.P. Wind Power Smoothing by Controlling the Inertial Energy of Turbines with Optimized Energy Yield. *IEEE Access* **2017**, *5*, 23374–23382. <https://doi.org/10.1109/ACCESS.2017.2757929>.
- Lyu, X.; Zhao, J.; Jia, Y.; Xu, Z.; Po Wong, K. Coordinated Control Strategies of PMSG-Based Wind Turbine for Smoothing Power Fluctuations. *IEEE Trans. Power Syst.* **2019**, *34*, 391–401. <https://doi.org/10.1109/TPWRS.2018.2866629>.
- Lyu, X.; Jia, Y.; Xu, Z.; Ostergaard, J. Mileage-Responsive Wind Power Smoothing. *IEEE Trans. Ind. Electron.* **2020**, *67*, 5209–5212. <https://doi.org/10.1109/TIE.2019.2927188>.
- Mahmoudi, N.; Saha, T.K.; Eghbal, M. Wind Power Offering Strategy in Day-Ahead Markets: Employing Demand Response in a Two-Stage Plan. *IEEE Trans. Power Syst.* **2015**, *30*, 1888–1896. <https://doi.org/10.1109/TPWRS.2014.2354571>.
- Li, C.; Yao, Y.; Zhao, C.; Wang, X. Multi-Objective Day-Ahead Scheduling of Power Market Integrated With Wind Power Producers Considering Heat and Electricity Trading and Demand Response Programs. *IEEE Access* **2019**, *7*, 181213–181228. <https://doi.org/10.1109/ACCESS.2019.2959012>.
- Yang, Y.; Qin, C.; Zeng, Y.; Wang, C. Optimal Coordinated Bidding Strategy of Wind and Solar System with Energy Storage in Day-ahead Market. *J. Mod. Power Syst. Clean Energy* **2022**, *10*, 192–203. <https://doi.org/10.35833/MPCE.2020.000037>.
- Abdelghany, M.B.; Faisal Shehzad, M.; Liuzza, D.; Mariani, V.; Glielmo, L. Modeling and Optimal Control of a Hydrogen Storage System for Wind Farm Output Power Smoothing. In Proceedings of the 2020 59th IEEE Conference on Decision and Control (CDC), Jeju, Korea, 14–18 December 2020; pp. 49–54. <https://doi.org/10.1109/CDC42340.2020.9304133>.
- Koiwa, K.; Ishii, T.; Liu, K.Z.; Zanma, T.; Tamura, J. On the Reduction of the Rated Power of Energy Storage System in Wind Farms. *IEEE Trans. Power Syst.* **2020**, *35*, 2586–2596. <https://doi.org/10.1109/TPWRS.2019.2960463>.
- Yang, M.; Zhang, L.; Cui, Y.; Zhou, Y.; Chen, Y.; Yan, G. Investigating the Wind Power Smoothing Effect Using Set Pair Analysis. *IEEE Trans. Sustain. Energy* **2020**, *11*, 1161–1172. <https://doi.org/10.1109/TSTE.2019.2920255>.
- Barra, P.; de Carvalho, W.; Menezes, T.; Fernandes, R.; Coury, D. A review on wind power smoothing using high-power energy storage systems. *Renew. Sustain. Energy Rev.* **2021**, *137*, 110455. <https://doi.org/10.1016/j.rser.2020.110455>.
- Lamsal, D.; Sreeram, V.; Mishra, Y.; Kumar, D. Output power smoothing control approaches for wind and photovoltaic generation systems: A review. *Renew. Sustain. Energy Rev.* **2019**, *113*, 109245. <https://doi.org/10.1016/j.rser.2019.109245>.
- Zhai, Y.; Zhang, J.; Tan, Z.; Liu, X.; Shen, B.; Coombs, T.; Liu, P.; Huang, S. Research On the Application of Superconducting Magnetic Energy Storage in the Wind Power Generation System For Smoothing Wind Power Fluctuations. *IEEE Trans. Appl. Supercond.* **2021**, *31*, 1–5. <https://doi.org/10.1109/TASC.2021.3064520>.
- Yang, R.H.; Jin, J.X. Unified Power Quality Conditioner With Advanced Dual Control for Performance Improvement of DFIG-Based Wind Farm. *IEEE Trans. Sustain. Energy* **2021**, *12*, 116–126. <https://doi.org/10.1109/TSTE.2020.2985161>.
- Wang, B.; Cai, G.; Yang, D. Dispatching of a Wind Farm Incorporated With Dual-Battery Energy Storage System Using Model Predictive Control. *IEEE Access* **2020**, *8*, 144442–144452. <https://doi.org/10.1109/ACCESS.2020.3014214>.
- Sattar, A.; Al-Durra, A.; Caruana, C.; Debouza, M.; Mueen, S.M. Testing the Performance of Battery Energy Storage in a Wind Energy Conversion System. *IEEE Trans. Ind. Appl.* **2020**, *56*, 3196–3206. <https://doi.org/10.1109/TIA.2020.2979792>.
- Wan, C.; Qian, W.; Zhao, C.; Song, Y.; Yang, G. Probabilistic Forecasting Based Sizing and Control of Hybrid Energy Storage for Wind Power Smoothing. *IEEE Trans. Sustain. Energy* **2021**, *12*, 1841–1852. <https://doi.org/10.1109/TSTE.2021.3068043>.
- Spichartz, B.; Günther, K.; Sourkounis, C. New Stability Concept for Primary Controlled Variable Speed Wind Turbines Considering Wind Fluctuations and Power Smoothing. *IEEE Trans. Ind. Appl.* **2022**, *58*, 2378–2388. <https://doi.org/10.1109/TIA.2022.3144650>.
- De Battista, H.; Mantz, R.J.; Garelli, F. Power conditioning for a wind-hydrogen energy system. *J. Power Sources* **2006**, *155*, 478–486. <https://doi.org/10.1016/j.jpowsour.2005.05.005>.
- Little, M.; Thomson, M.; Infield, D. Electrical integration of renewable energy into stand-alone power supplies incorporating hydrogen storage. *Int. J. Hydrogen Energy* **2007**, *32*, 1582–1588. <https://doi.org/10.1016/j.ijhydene.2006.10.035>.
- Takahashi, R.; Kinoshita, H.; Murata, T.; Tamura, J.; Sugimasa, M.; Komura, A.; Futami, M.; Ichinose, M.; Ide, K. Output Power Smoothing and Hydrogen Production by Using Variable Speed Wind Generators. *IEEE Trans. Ind. Electron.* **2010**, *57*, 485–493. <https://doi.org/10.1109/TIE.2009.2032437>.
- Mueen, S.; Takahashi, R.; Tamura, J. Electrolyzer switching strategy for hydrogen generation from variable speed wind generator. *Electr. Power Syst. Res.* **2011**, *81*, 1171–1179. <https://doi.org/10.1016/j.epsr.2011.01.005>.
- Wen, T.; Zhang, Z.; Lin, X.; Li, Z.; Chen, C.; Wang, Z. Research on Modeling and the Operation Strategy of a Hydrogen-Battery Hybrid Energy Storage System for Flexible Wind Farm Grid-Connection. *IEEE Access* **2020**, *8*, 79347–79356. <https://doi.org/10.1109/ACCESS.2020.2990581>.
- Huang, C.; Zong, Y.; You, S.; Træholt, C.; Zheng, Z.; Xie, Q. Cooperative Control of Wind-Hydrogen-SMES Hybrid Systems for Fault-Ride-Through Improvement and Power Smoothing. *IEEE Trans. Appl. Supercond.* **2021**, *31*, 1–7. <https://doi.org/10.1109/TASC.2021.3103729>.

25. Koiwa, K.; Cui, L.; Zanma, T.; Liu, K.Z.; Tamura, J. A Coordinated Control Method for Integrated System of Wind Farm and Hydrogen Production: Kinetic Energy and Virtual Discharge Controls. *IEEE Access* **2022**, *10*, 28283–28294. <https://doi.org/10.1109/ACCESS.2022.3158567>.
26. Bemporad, A.; Morari, M. Control of systems integrating logic, dynamics, and constraints. *Automatica* **1999**, *35*, 407–427. [https://doi.org/10.1016/S0005-1098\(98\)00178-2](https://doi.org/10.1016/S0005-1098(98)00178-2).
27. Williams, P.H. *Model Building in Mathematical Programming*, 5th ed.; John Wiley & Sons Ltd.: Hoboken, NJ, USA, 2013.
28. Bynum, M.L.; Hackebeil, G.A.; Hart, W.E.; Laird, C.D.; Nicholson, B.L.; Sirola, J.D.; Watson, J.P.; Woodruff, D.L. *Pyomo—Optimization Modeling in Python*, 3rd ed.; Springer: Berlin/Heidelberg, Germany, 2021; Volume 67.
29. Hart, W.E.; Watson, J.P.; Woodruff, D.L. Pyomo: Modeling and solving mathematical programs in Python. *Math. Program. Comput.* **2011**, *3*, 219–260.
30. Pyomo.org. 2022. Available online: <http://www.pyomo.org/> (accessed on 1 July 2022).
31. FICO. 2022. Available online: <https://www.fico.com/en/products/fico-xpress-optimization> (accessed on 1 July 2022).
32. Friendly Power S.r.l. 2022. Available online: <http://www.friendlypower.it/> (accessed on 1 July 2022).
33. GME – Gestore Mercati Energetici. 2022. Available online: <http://www.mercatoelettrico.org/> (accessed on 1 July 2022).
34. Atif, A.; Khalid, M. Savitzky-Golay Filtering for Solar Power Smoothing and Ramp Rate Reduction Based on Controlled Battery Energy Storage. *IEEE Access* **2020**, *8*, 33806–33817. <https://doi.org/10.1109/ACCESS.2020.2973036>.